HIGH-RESOLUTION MODELING OF CLIMATE CHANGE IMPACTS ON WATER SUPPLY AND DEMAND, AND GHG EMISSIONS IN AN OKANAGAN-SIMILKAMEEN SUBWATERSHED, BRITISH COLUMBIA, CANADA

SHAGHAYEGH MIRMASOUDI
Master of Science, Bu-Ali Sina University, 2009

A Thesis
Submitted to the School of Graduate Studies
of the University of Lethbridge
in Partial Fulfilment of the
Requirements for the Degree

DOCTOR OF PHILOSOPHY

Department of Geography
University of Lethbridge
LETHBRIDGE, ALBERTA, CANADA

HIGH-RESOLUTION MODELING OF CLIMATE CHANGE IMPACTS ON WATER SUPPLY AND DEMAND, AND GHG EMISSIONS IN AN OKANAGAN-SIMILKAMEEN SUBWATERSHED, BRITISH COLUMBIA, CANADA

SHAGHAYEGH MIRMASOUDI

Date of Defence: October 5, 2018

Dr. James Byrne Supervisor	Professor	Ph.D.
Dr. Dan Johnson Thesis Examination Committee Member	Professor	Ph.D.
Dr. Roland Kroebel Thesis Examination Committee Member	Adjunct Professor	Ph.D.
Dr. Ryan MacDonald Thesis Examination Committee Member	Adjunct Professor	Ph.D.
Dr. Kent Peacock Internal Examiner	Professor	Ph.D.
Dr. Aaron Berg External Examiner University of Guelph Guelph, Ontario	Professor	Ph.D.
Dr. Greg Pyle Chair, Thesis Examination Committee	Professor	Ph.D.

Dedication

To Nima for his love, patience, support, and friendship.

Abstract

The interactions of atmospheric, landscape, hydrologic and agricultural processes on natural resources and greenhouse gas (GHG) emissions were assessed for a mountain watershed in south central British Columbia, Canada. A novel solar radiation model which uses the most available input data was developed in order to model solar radiation for the study watershed as input to the Generate Earth Systems Science (GENESYS) hydrometeorological model. Historical and future water supply and vegetation water demand under a range of climate scenarios using GENESYS were modelled for the watershed and the results revealed possible future changes in water supply and demand that are likely to stress future water resource management in the watershed. The GENESYS and Holos models were linked to estimate GHG emissions (CO_2, CH_4, and N_2O) and soil carbon change for both crop and animal production processes in a simulated farm in the watershed under different climate and management scenarios and the results indicated that climate change is likely to affect future agricultural GHG emissions and suggested the available mitigation options.

Acknowledgements

I would like to say thank you to my parents, family, professors, lab mates, and friends for all their support. I must thank my husband, Fariborz Mansouri for encouraging and supporting me. I am especially grateful to my supervisor James Byrne and my Thesis committee members Dan Johnson, Roland Kroebel, and Ryan MacDonald for all their support, help, and guidance through my journey. I would like to thank Kent Peacock, Aaron Berg and, Greg Pyle for their great contribution to this Thesis. Special thanks to Aklilu Alemu, Shannan Little, Sarah Pogue, Marcos Cordeiro, Henry Janzen, Candace Vanin, Devin Cairns, Laura Chasmer, and Celeste Barnes for their help with this research. I am forever grateful for Department of Geography, School of Graduate Studies, International Student Center, Solutions Centre, and Library at the University of Lethbridge for all their support.

Thank you to the University of Lethbridge, the Mitacs Program (Canada), in cooperation with NOVUS Environmental, Guelph, Ontario, Elk River Alliance, and Stantec Consulting Ltd. that this research would not have been possible without the financial support provided by them.

Table of Contents

List of Tables

List of Figures

Chapter 1 : Introduction

This work assesses the interactions of atmospheric, landscape, hydrologic and agricultural processes on natural resources and greenhouse gas (GHG) emissions for a mountain watershed in south central British Columbia. GHGs are atmospheric trace gases that absorb long-wave radiation emitted from the Earth's surface, thereby warming the lower atmosphere. Primary GHGs include carbon dioxide (CO_2), methane (CH_4) and nitrous oxide (N_2O).

In mountain watersheds of western North America, water supply and demand are largely driven by temperature, humidity, precipitation, snow accumulation and melt, and by vegetation evapotranspiration (Barnett et al., 2005). The variations in water supply and demand are highly correlated with the energy availability especially energy gained from shortwave and longwave radiation exchanges (Sheppard, 1996). The amount of solar radiation received by the Earth's surface is necessary information for different hydrometeorological models. Collecting radiation data in most countries is costly because of the equipment maintenance and the data processing and so solar radiation data are usually only collected by a few meteorological stations (McKenney et al., 2008). There have always been different choices of solar radiation models, but finding models within the usual range of accuracy, with lower number of input parameters, with more available input data, and suitable for different climate conditions is still difficult.

Climate change as a result of increasing atmospheric CO_2 concentration and other GHGs will have a significant impact on mountain hydrology and consequently water supply and demand in areas with substantial agriculture (Barnett et al., 2005; Neilsen et al.,

2006). These changes may result in substantial changes in GHG absorption, generation and energy, water, and GHG exchange between land cover systems and the atmosphere.

Southern British Columbia, Canada, is one of the regions that is expected to experience higher air temperature, earlier snowmelt, lower snow water equivalent during the spring, more precipitation as rainfall than snow, more crop water requirements, longer growing season period, more winter runoff and less summer runoff, lower average peak stream discharge, higher winter and spring stream flow, and lower summer stream flow as result of increasing atmospheric GHG concentrations (Leith and Whitfield, 1998; Hamlet and Lettenmaier, 1999; Cohen et al., 2000; Morrison et al., 2002; Cohen et al., 2006; Merritt et al., 2006; Neilsen et al., 2006; Jost and Weber, 2012; Shrestha et al., 2012; Schnorbus et al., 2014; Najafi et al., 2017).

Significant amounts of anthropogenic GHGs are released by agroecosystems to the Earth's atmosphere, which is about 8% of the total GHG emissions in Canada, excluding energy use-related CO_2 emissions (Janzen et al., 2006). Agricultural soils also play a role as a source of carbon by storing carbon (Janzen et al., 2006). There are also many cost-effective ways to mitigate agricultural GHG emissions that use current technologies and opportunities and can be applied rapidly (Burney et al., 2010). How agriculture will impact GHG emissions is reasonably well known, but how GHG increases and how associated atmospheric change will change agricultural systems is still unclear (IPCC, 2014).

Mitigation potential in the agriculture sector can be determined through two different pathways; elimination of GHG from the atmosphere, or reduction of GHG emissions by choice of management in both crops and livestock; however, costs and potentials are

distributed differently among regions (IPCC, 2014). There are also some barriers like climate and non-climate policies, social, economic, institutional, ecological, technological, and educational barriers that increase the gap between actual and potential mitigation options (Smit and Skinner, 2002). However, more research and development in mitigation options in agriculture can remove the technological barriers (IPCC, 2014). Furthermore, on the global scale, some mitigation options are more applicable than others but in the regional scale, this may be different (IPCC, 2014).

There is a clear need to assess climate change impacts on water supply and demands, and on agriculture-derived GHG emissions for different geographic regions and agricultural systems. These assessments are needed for local sectors to provide the related information necessary for mitigation practices (Stocker, 2014). The Generate Earth Systems Science input (GENESYS) spatial hydrometeorological model investigates current and future hydrometeorological conditions (MacDonald et al., 2009). The GENESYS model estimates hydrometeorological variables by applying a series of processed-based routines and commonly available meteorological data. It has been applied in studies of climate change impact assessments on hydrometeorology in western North American watersheds for different climate change scenarios (Lapp et al., 2005; MacDonald et al., 2009; Larson et al., 2011; MacDonald et al., 2011; MacDonald et al., 2012; MacDonald et al., 2013). The changes in hydrometeorological conditions are then applied to estimate climate-induced changes in GHG emissions (CO_2, CH_4 and N_2O) and soil carbon stocks for both crop and animal production processes. The Holos GHG emissions estimation model was designed by scientists at Agriculture and Agri-Food Canada to estimate GHG emissions and soil carbon stock for Canadian farms, including both animal

management and cropping systems (Little et al., 2008). The model has been applied to estimate farm GHG emissions and also assess the impacts of management practices changes on farm GHG emissions (Janzen et al., 2006; Little et al., 2008; Stewart et al., 2009; Beauchemin et al., 2010; Beauchemin et al., 2011; Bonesmo et al., 2012; Kröbel et al., 2012; Mc Geough et al., 2012; Hünerberg et al., 2014; Chai et al., 2016; Kröbel et al., 2016; Legesse et al., 2016; Alemu et al., 2017a; Alemu et al., 2017b; Guyader et al., 2017).

The Olalla watershed is a subwatershed in the Regional District of Okanagan-Similkameen (RDOS), southern British Columbia, Canada with the total drainage area of about 181 km^2 and elevation range from 476 to 2235 meters above sea level (m a.s.l). The watershed has a generally dry climate, and is mostly covered by Interior Douglas Fir (IDF) (Regional District of Okanagan-Similkameen, 2011a; Hectares BC, 2015). The agricultural area in the watershed consists of un-irrigated rangeland (7.3% of the watershed area) and irrigated cropland (1.8% of the watershed area) (Hectares BC, 2015). Cattle ranching is the dominant agricultural activity in this area and 78% of the irrigated land is used to grow perennial hay and pasture, and 3% to grow annual field crops. Fruit production is the other important agricultural activity and 17% of the irrigated land is used to grow fruits. The remaining 2% of the irrigated area is for vegetable production (Statistics Canada, 2006). The irrigation season in the watershed is from April to the end of September for most irrigation users (Regional District of Okanagan-Similkameen, 2011b) and irrigation licences use wells close to the Keremeos Creek and its tributaries inside the Olalla watershed (BC Government, 2018).

1.1. Thesis objectives

This research has four main objectives to better understand the impacts of climate change on water supply and demand, and agricultural GHG emissions in the Olalla watershed.

1. Model solar radiation using an accurate proposed solar radiation model which uses the most available input data.

2. Model historical and future water supplies under a range of climate scenarios using the GENESYS hydrometeorological model.

3. Estimate historical vegetation water requirement and assess climate-driven changes in that parameter for a range of future climate scenarios using GENESYS.

4. Link the GENESYS and Holos GHG emissions estimation models to estimate CO_2, CH_4 and N_2O emissions and soil carbon change for agricultural - both crop and animal production - processes under different climate and management scenarios.

1.2. Thesis structure

Chapter 1 is the introduction chapter of the Thesis. The objectives noted above are presented in three following chapters (Figure 1.1). The first objective is presented in Chapter 2, the second and third objectives are presented in Chapter 3 and the fourth objective is presented in Chapter 4. Chapter 5, the conclusion and summary of the Thesis, outlines the main findings of the research.

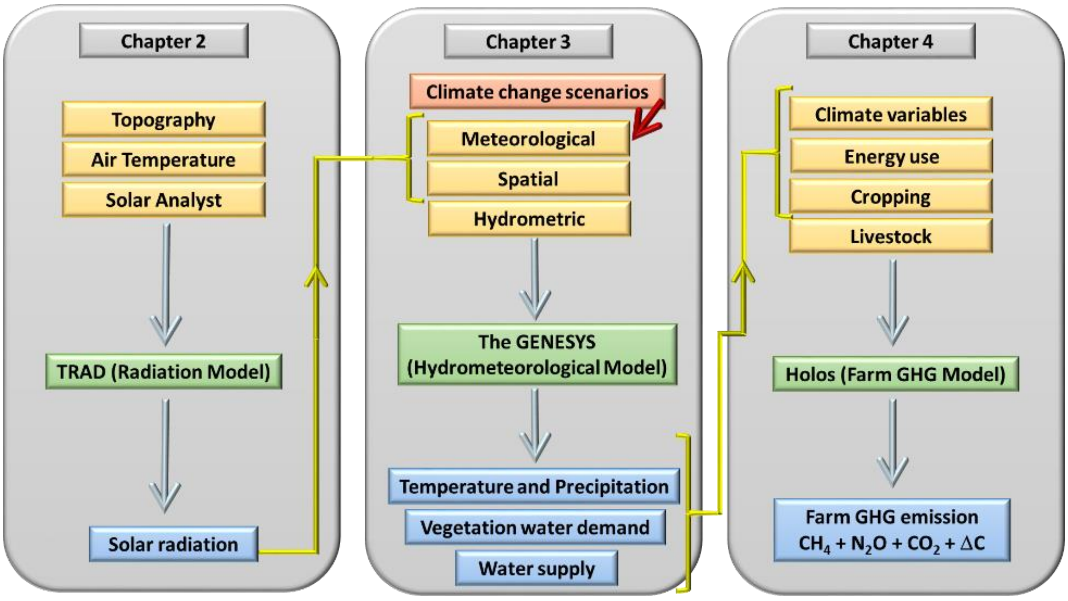

Figure 1.1: Diagram representing Chapters 2, 3, and 4 of the Thesis and the way that they are linked

Chapter 2 : A novel time-effective model for daily distributed solar radiation estimates across variable terrain

2.1. Introduction

Solar radiation is a driver of photosynthesis and evapotranspiration, and accurate estimation of spatially continuous long-term solar radiation data is necessary information for many hydrometeorological models (Kodysh et al., 2013; Aladenola and Madramootoo, 2014).

Collecting radiation data in most countries is costly, difficult, and involves uncertainties, so solar radiation data are usually only recorded by a few meteorological stations (McKenney et al., 2008). For this reason, over the last few decades, many models have been developed for representing the spatio-temporal variability of global solar radiation including recent satellite-based models, or predictive models based on correlations of solar radiation with sunshine duration, air temperature, cloud observations, and other weather data (Table 2.1). These spatial models are based on solar geometries and take into account site latitude, local topography, and shadowing effects. However, they use different methods to calculate solar radiation, and they need different data for implementing atmospheric attenuation (Table 2.1).

Table 2.1: A brief summary of the spatially-based solar radiation models, their errors and testing locations.

Model	MBE (%)	Main inputs	Testing locations
Bird (Bird and Hulstrom, 1981; Badescu et al., 2012; Gueymard and Ruiz-Arias, 2015)	8.0	Air mass, surface albedo, surface air pressure, precipitable water vapor, ozone	Sun-photometric sites
CEM (Atwater and Ball, 1978; Badescu et al., 2012)	5.0	Surface albedo, surface air pressure, precipitable water vapor, cloud observations	USA
ESRA (Rigollier et al., 2000; Badescu et al., 2012; Gueymard and Ruiz-Arias, 2015)	5.0	Surface air pressure, Linke index	Europe
Ineichen (Ineichen, 2008; Gueymard and Ruiz-Arias, 2015)	2.0	Atmospheric aerosol optical depth, precipitable water vapor	Europe
METSTAT (Maxwell, 1998; Badescu et al., 2012; Gueymard and Ruiz-Arias, 2015)	5.0	Cloud observations, aerosol optical depth, precipitable water vapor, ozone, surface albedo, snow depth, days-since-last snowfall, atmospheric pressure	USA
MRM5 (Gul et al., 1998; Muneer et al., 1998; Badescu et al., 2012; Gueymard and Ruiz-Arias, 2015)	5.0	Sunshine fraction, dry- and wet-bulb temperature	UK, Japan, Europe
NSRDB – SUNY (Nottrott and Kleissl, 2010)	5.0	Meteorological satellite images	USA
Paulescu (Paulescu and Schlett, 2003; Badescu et al., 2012; Gueymard and Ruiz-Arias, 2015)	-5.0	Surface air pressure, precipitable water vapor, ozone	Sun-photometric sites
RES2 81 (Gueymard, 2008; Gueymard and Ruiz-Arias, 2015)	5.0	Precipitable water vapor, ozone, surface albedo, aerosol albedo, atmospheric pressure	Sun-photometric sites
r.sun (Šúri and Hofierka, 2004; Ruiz-Arias et al., 2009)	-4.5	Linke index	Spain
Solei32 (Miklánek and Mészároš, 1993; Ruiz-Arias et al., 2009)	-4.5	Linke index	Spain
Solar Analyst (Dubayah and Rich, 1995; Fu and Rich, 2002; Ruiz-Arias et al., 2009)	-25.0	Direct atmospheric transmissivity, diffuse fraction (default values)	Spain
SRAD (Wilson and Gallant, 2000; Ruiz-Arias et al., 2009)	10.0	Monthly average sunshine fraction and cloudiness data	Spain
Zelenka (Zelenka et al., 1999)	10.0	Meteorological satellite images	Switzerland, USA

Atmospheric attenuation often varies substantially with surface radiation. However, most locations lack long-term radiation, cloudiness, and/or satellite data for many climate stations, which are needed in order to identify and estimate atmospheric attenuation. For example, models such as r.sun (Šúri and Hofierka, 2004; Ruiz-Arias et al., 2009), Solei-32 (Miklánek and Mészároš, 1993; Ruiz-Arias et al., 2009) and, ESRA (Rigollier et al., 2000;

Badescu et al., 2012; Gueymard and Ruiz-Arias, 2015) calculate the overcast radiation from clear sky values and a clear-sky index called Linke (Table 2.1, (Kasten and Czeplak, 1980; Beyer et al., 1996)). The Linke must be derived from one of the three methods: 1) from the ratio between measured global radiation and computed values of clear sky global radiation, 2) from other climatologic data such as cloudiness (Kasten and Czeplak, 1980), or 3) directly from short-wave surface irradiance measured by satellites (Beyer et al., 1996). Although satellite-based models may be suitable for solar radiation estimation in large regions, their disadvantages are high cost and lack of historical records, because these methods are comparably new (Olatomiwa et al., 2015).

Sunshine duration is the most widely used meteorological parameter for solar radiation estimation, in the literature. This variable is more available and gives relatively better results than other variables (Sen, 2008). However, air temperature data can be used instead, when the sunshine duration is not available at a specific location and time period (Yacef et al., 2014) as air temperature data have been collected at many locations globally, and generally for a much longer period relative to any meteorological records (Gago et al., 2011). However, using only air temperature, or air temperature along with wind speed or relative humidity data, to predict solar radiation may result in better estimation of solar radiation in clear sky conditions (higher solar radiation values) compared with cloudy sky conditions (lower solar radiation values) (Ogliari et al., 2013; Quan et al., 2013).

Furthermore, empirical models, either unified and continuous or as combinations of empirical models for certain ranges, can estimate solar radiation for specific climate or specific region, because they use empirical coefficients estimated using correlations between global solar radiation and other climate variables for that specific area (Yacef et

al., 2014). Accurate and simple models that are applicable for different types of climates or regions have been used in this way. Additionally, when hourly or other short-term estimation of solar radiation is necessary, it may be more practical to start with daily estimations and calculate hourly values form daily values (Collares-Pereira and Rabl, 1979).

According to the spatially-based solar radiation models' average uncertainty reported in Table 2.1, all these models are comparable with the measured values with a mean bias error (MBE) of about -5% to 10% except Solar Analyst (Dubayah and Rich, 1995; Fu and Rich, 2002; Ruiz-Arias et al., 2009) that shows an underestimation of about 25% relative to the corresponding observed values and also its reliability decreases in cloudy sky conditions. Myers (2005) reviewed uncertainties in several solar radiation models and concluded that the best model uncertainties are representing the uncertainties in existing measured data which is corresponded to the mean absolute bias error ($MABE$) of 25 to 100 $W{\cdot}m^{-2}$. However, developing models with fewer input parameters under different climate conditions remains a challenge (Myers, 2005). Therefore, a daily global solar radiation model, within the usual range of accuracy, with lower input parameters, with more available input data, and suitable for different climate conditions can be usefully applied for accurate estimation of solar radiation necessary for different studies including hydrometeorological modeling.

Solar Analyst (Dubayah and Rich, 1995; Fu and Rich, 2002; Ruiz-Arias et al., 2009), which has been implemented as a tool in ESRI ArcGIS, estimates solar radiation for any geographical locations specified by a latitude and longitude or for any study area as a sum of direct radiation (D_R) and diffuse radiation (F_R) (Fu and Rich, 2002). More specifically,

Solar Analyst (Dubayah and Rich, 1995; Fu and Rich, 2002; Ruiz-Arias et al., 2009) considers atmospheric attenuation by using direct atmospheric transmissivity (τ), defined as the proportion of extraterrestrial radiation (H_0) transmitted as direct radiation at sea level along the shortest atmospheric path, plus diffuse fraction (K_D), which is the fraction of global normal radiation flux that is diffused (Fu and Rich, 2002).

In the current chapter, we present a daily solar radiation estimation method which uses ambient air temperature, a digital elevation model (DEM), latitude and longitude of the study location, time of year, and monthly radiation estimates from Solar Analyst (G_{R_m}) (Dubayah and Rich, 1995; Fu and Rich, 2002; Ruiz-Arias et al., 2009) in order to estimate solar radiation for the hydrometeorological modelling presented in Chapter 3. Our objective is to provide improved, spatially and more widely applicable estimation by using air temperature-based empirical models for atmospheric transmissivity (K_T) and diffuse fraction to vary total monthly radiation estimation from Solar Analyst (Dubayah and Rich, 1995; Fu and Rich, 2002; Ruiz-Arias et al., 2009) and then calculate total daily radiation ($G_{R_{d_{TRAD}}}$) as a fraction of total monthly radiation by applying a daily transmissivity-based ratio by using the TRAD (temperature-estimation of radiation) daily model, as air temperature data is readily available at most locations on the planet. Our model stems from the observation that the difference between maximum and minimum air temperature (ΔT) has a strong correlation with daily average shortwave radiation (Bristow and Campbell, 1984). Furthermore, hourly solar radiation can be decomposed from the daily values by using a ratio between daily and hourly radiation (Liu and Jordan, 1960; Tham et al., 2010).

2.2. Methods

2.2.1. The TRAD (temperature-estimation of radiation) daily model

Our presented TRAD daily model assumed that the daily variations in irradiation for each month are a function of daily variations in atmospheric transmissivity, the proportion of daily irradiance reaching the Earth's surface to the daily extra-terrestrial insolation, in the same month. Irradiation is the amount of solar energy arriving on a unit area over a stated time interval (Wh·m^{-2}) (Page, 1986). We proposed the TRAD model to estimate daily irradiation values in any ground station by Equation 2.1:

$$G_{R_{d_{TRAD}}} = \left[K_{T_{d_{B-C}}} \Big/ \sum_{d=1}^{n} K_{T_{d_{B-C}}} \right] \times G_{R_m} \quad (2.1)$$

where, $G_{R_{d_{TRAD}}}$ is irradiation for the day in question (Wh·m^{-2}), $K_{T_{d_{B-C}}}$ is the corresponding atmospheric transmissivity of that day calculated using the Bristow and Campbell model (Bristow and Campbell, 1984), using maximum and minimum air temperature inputs, $\sum_{d=1}^{n} K_{T_{d_{B-C}}}$ is sum of all daily atmospheric transmissivity values in the corresponding month, and G_{R_m} is total monthly irradiation (Wh·m^{-2}) from Solar Analyst (Dubayah and Rich, 1995; Fu and Rich, 2002; Ruiz-Arias et al., 2009). G_{R_m} is estimated using a DEM, latitude and longitude of the study location, average annual $K_{T_{d_{B-C}}}$ at sea level ($K_{T_{d_{B-C\,(sl)}}}$) (Bristow and Campbell, 1984), and average annual daily diffuse fraction calculated by Carroll model ($K_{D_{d_{Ca}}}$) (Carroll, 1985).

Values of $G_{R_{d_{TRAD}}}$ (Wh·m^{-2}) were calculated for different study locations for their available observed daily irradiance (W·m^{-2}) record periods. Daily irradiance (W·m^{-2}), the

instantaneous energy received on a unit area per unit time (Page, 1986), was calculated from $G_{R_{d_{TRAD}}}$ (Wh·m^{-2}). The following section reviews daily atmospheric transmissivity and diffuse fraction models (Bristow and Campbell, 1984; Carroll, 1985) and also Solar Analyst (Dubayah and Rich, 1995; Fu and Rich, 2002; Ruiz-Arias et al., 2009) which was used in the daily irradiation estimation using TRAD.

2.2.2. Daily atmospheric transmissivity and diffuse fraction models

Daily atmospheric transmissivity using the Bristow and Campbell (1984) model was used to estimate daily diffuse fraction using Carroll's model (Carroll, 1985). $K_{T\,d_{B-C}}$ and $K_{D\,d_{Ca}}$ were then used to calculate average annual $K_{T\,d_{B-C\,(sl)}}$ and average annual $K_{D\,d_{Ca}}$ in order to estimate G_{R_m} values using Solar Analyst (Dubayah and Rich, 1995; Fu and Rich, 2002; Ruiz-Arias et al., 2009) (Equation 2.1). Then $K_{T\,d_{B-C}}$ and G_{R_m} were used in the TRAD model to calculate $G_{R_{d_{TRAD}}}$.

Bristow and Campbell (1984) proposed the following model for daily atmospheric transmissivity using the difference between maximum and minimum air temperature (ΔT):

$$K_{T\,d_{B-C}} = A \times (1 - \exp(-B \times \Delta T^{C})) \qquad (2.2)$$

In this equation, A, B, and C are empirical coefficients. Although empirical in nature, these coefficients represent the physics involved in the relationship, where A represents the maximum clear sky atmospheric transmissivity characteristics of the study region, which varies with elevation and pollution content of the air. Bristow and Campbell (1984) developed and tested their method using data from three different sites in the northwestern

United States and showed that this method provides accurate estimates of daily atmospheric transmissivity at these stations. Thornton and Running (1999) reformulated the Bristow-Campbell model (Bristow and Campbell, 1984) using daily measured temperature, humidity, and precipitation in order to calculate daily solar radiation in 40 stations in locations with different climates. Their model gives a spatially and temporally variable estimation of A (Thornton and Running, 1999). However, Bristow and Campbell (1984) used a constant value of A over all their study stations. B and C display the partitioning of energy which is characteristic of the region of interest. Bristow and Campbell (1984) found it adequate to hold C constant at 2.4 for their study sites and consider B related to monthly mean ΔT via Relation 2.3:

$$B = 0.036 \times \exp(-0.154 \times \overline{\Delta T}) \tag{2.3}$$

In our study A, B and C were applied as they were used in Bristow and Campbell (1984). $K_{T\,d_{B-C}}$ was corrected based on elevation of the stations by the following equation, in order to use in Solar Analyst to estimate G_{R_m}(Dubayah and Rich, 1995; Fu and Rich, 2002; Ruiz-Arias et al., 2009):

$$K_{T\,d_{B-C\,(sl)}} = K_{T\,d_{B-C}} - (t_{lapse} \times Z) \tag{2.4}$$

where $K_{T\,d_{B-C\,(sl)}}$ is atmospheric transmissivity at sea level, t_{lapse} is typically equal to 0.00008 m^{-1} and Z is elevation in m above the sea level (Hungerford et al., 1989; Wilson and Gallant, 2000)

Liu and Jordan (1960) suggested that diffuse fraction should be a well-behaved function atmospheric transmissivity. Carroll (1984) proposed two relations for diffuse

fraction based on atmospheric transmissivity. We used atmospheric transmissivity from Bristow and Campbell (1984) model in Carroll's model (Carroll, 1985). The following equations shows how we estimated diffuse fraction using Carroll's model (Carroll, 1985) and $K_{T\,d_{B-C}}$.

for cloud-free conditions: $$K_{D\,d_{Ca}} = 0.88 - 1.024 \times K_{T\,d_{B-C}} \quad (2.5)$$

and for cloudy conditions: $$K_{D\,d_{Ca}} = Min \begin{cases} 1.11 - 1.16 \times K_{T\,d_{B-C}} \\ or \\ 1.0 \end{cases} \quad (2.6)$$

We applied the thresholds proposed by Colli et al. (2016) for classification of daily average sky conditions of a ground station (Table 2.2). The model was evaluated for three different groups of days based on different sky conditions including cloudy days, partly cloudy days, and sunny or clear days (Table 2.2).

Table 2.2: Daily atmospheric transmissivity thresholds for day classification (Colli et al., 2016).

Daily atmospheric transmissivity	Day classification
daily atmospheric transmissivity≤0.30	cloudy
0.30 < daily atmospheric transmissivity < 0.50	partly cloudy
daily atmospheric transmissivity≥ 0.50	sunny and clear

2.2.3. Application of Solar Analyst

Total annual global solar radiation in monthly intervals (G_{R_m}) was calculated using Solar Analyst (Dubayah and Rich, 1995; Fu and Rich, 2002; Ruiz-Arias et al., 2009) by a DEM, latitude and longitude of the study location, and estimates of average annual $K_{T\,d_{B-C\,(sl)}}$ and average annual $K_{D\,d_{Ca}}$.

Four calculations are contained in the upward-looking hemispherical algorithm applied in Solar Analyst (Dubayah and Rich, 1995; Fu and Rich, 2002; Ruiz-Arias et al., 2009): viewshed, sunmap, skymap calculation, and a concluding calculation that uses the previous three calculations to estimate a solar radiation value. The total amount of global solar radiation in $Wh \cdot m^{-2}$ is obtained by the sum of direct solar radiation ($Wh \cdot m^{-2}$) for all sunmap sectors and diffuse solar radiation for all skymap sectors ($Wh \cdot m^{-2}$) (Fu and Rich, 2002). The direct solar radiation from a sunmap sector with a centroid at solar zenith angle (degrees) and solar azimuth angle (degrees) is a function of the solar constant value (1367 $W \cdot m^{-2}$), τ, the elevation above sea level (meters), the time duration represented by the sky factor, the surface zenith angle (degrees), the surface azimuth angle (degrees), and the gap fraction for the sunmap sector. Correspondingly, diffuse solar radiation for each sky sector at the same centroid is related to diffuse fraction, the elevation above sea level (meters), the bounding zenith angles of the sky sector (degrees), the number of azimuthal divisions in the sky map, the time interval for analysis, fraction of visible sky for the sky sector (0-1), and the angle of incidence between the centroid of the sky sector and the intercepting surface (degrees). However, providing a correct value for τ is difficult because it is sensitive to the presence of clouds (Ruiz-Arias et al., 2009). For this reason, we applied $K_{T\,d_{B-C\,(sl)}}$ and $K_{D\,d_{Ca}}$ in the calculation of G_{R_m} using Solar Analyst (Dubayah and Rich, 1995; Fu and Rich, 2002; Ruiz-Arias et al., 2009).

2.2.4. Observed daily atmospheric transmissivity

In the present study, observed daily atmospheric transmissivity on a horizontal surface was calculated using Equation 2.7, which defines atmospheric transmissivity (K_t) as a ratio of a day's radiation (G_R) to that day's extra-terrestrial radiation (H_0).

$$K_t = \frac{G_R}{H_0} \tag{2.7}$$

The value of G_R (W·m^{-2}) is determined from the available pyranometer measurements, but H_0 (J·m^{-2}) is calculated by the following method (Spencer, 1971):

$$H_0 = \frac{24\times3600G_{sc}}{\pi}\left(1 + 0.033\cos\frac{360n}{365}\right)\times\left(\cos\emptyset\ \cos\delta\ \sin\omega_s + \frac{\pi\omega_s}{180}\sin\emptyset\sin\delta\right) \tag{2.8}$$

G_{sc} is the solar constant (1367 W·m^{-2}), D is Julian date, and $\emptyset$ is the latitude. H_0 then converted to W·m^{-2} to use in Equation 2.7.

The declination δ is found from the equation below (Spencer, 1971) (23.45 is the Earth's rotational axis vector to the ecliptic plane in degrees):

$$\delta = 23.45\ \sin\left(360\frac{284+D}{365}\right) \tag{2.9}$$

The sunset hour angle ω_s in degrees from horizontal is calculated using the following equation (Spencer, 1971):

$$\cos\omega_s = -\tan\emptyset\ \tan\delta \tag{2.10}$$

2.2.5. Hourly solar radiation model

Accurate hourly solar radiation data are necessary in many studies, for example in solar photovoltaic projects. We can apply a ratio to the estimated daily solar radiation values from the previous steps (Equation 2.11) and decompose the hourly solar radiation values. Liu and Jordan (1960) improved the method of Whillier (Whillier, 1956) to calculate the ratio of hourly to daily global solar radiation using a set of regression curves. Collares-Pereira and Rabl (1979) validated their approach and presented Equation 2.11 for estimating this ratio, which only needs site latitude and day number;

$$r_G = \frac{\pi}{24}(a + b\cos\omega)\frac{\cos\omega - \cos\omega_s}{\sin\omega - \omega_s\cos\omega_s} \tag{2.11}$$

where r_G is the ratio of hourly to daily global radiation, a and b are dependent on sites (Equation 2.12 and 2.13), ω is hour angle in degrees and defined as the angular displacement of the sun east or west of the local meridian due to rotation of the Earth on its axis at 15 degrees per hour, morning negative, afternoon positive, and ω_s is the sunset hour angle in degrees that is calculated by Equation 2.10.

$$a = 0.4090 + 0.5016\sin(\omega_s - 1.047) \tag{2.12}$$

$$b = 0.6609 - 0.4767\sin(\omega_s - 1.047) \tag{2.13}$$

Equation 2.11 has been developed based on data from measurement sites in the USA, but it also has been validated for 13 Indian locations (Hawas and Muneer, 1984) and 16 sites in the UK (Tham et al., 2010).

2.2.6. Data availability for verification

The Surface Radiation Budget Network (SURFRAD) was established in 1993 in the US (Augustine et al., 2000) and became an official part of the Global Climate Observing System (GCOS) in April 2004 (Augustine et al., 2005). Currently seven SURFRAD stations are operating in diverse climate regions in the USA, in Montana, Colorado, Illinois, Mississippi, Pennsylvania, Nevada, and South Dakota (Table 2.3 and Figure 2.1). The stations are not surrounded by trees or other obstacles, but may be located in areas with small shrubs or agriculture.

An upward-looking pyranometer measures total global solar radiation ($W \cdot m^{-2}$) on its main platform. Accuracy of the pyranometer is about 5%, which is achieved by standards of calibrations and operations recommended by the Baseline Surface Radiation Network (BSRN), sponsored by the World Climate Research Program (WCRP) of the World Meteorological Organization (WMO). SURFRAD data are available in daily files of one- or three-minute data. We extracted daily maximum and minimum air temperature (^oC) and mean irradiance ($W \cdot m^{-2}$) from the one- or three-minute data records for the available historical time period at each station.

A small number of spurious values in air temperature and irradiance records were removed from the analysis. Irradiance data that had negative values due to cooling of the thermopile near dusk and dawn (Augustine et al., 2005) and values higher than the extraterrestrial solar radiation were filtered out as well. Missing data were not used in the analysis (Table 2.4). However, the amount of missing data was small (Table 2.4) as the data have already been quality controlled by SURFRAD (Table 2.4) (Augustine et al.,

2000). Furthermore, in order to analyze the results in both a large and a small sample size in terms of years, we used 2015 as a case study. A 30 x 30 meter DEM covering all the SURFRAD sites was applied (NASA LP DAAC, 2011).

The extracted observed daily maximum and minimum air temperature (^{o}C) data were used in the proposed solar radiation method to estimate daily mean irradiance ($W \cdot m^{-2}$, Equations 2.1-2.6) in order to compare it with the observed mean irradiance ($W \cdot m^{-2}$) at different SURFRAD stations. The observed daily mean irradiance ($W \cdot m^{-2}$) was also used to find observed daily atmospheric transmissivity (Equations 2.7-2.10) to compare it with the calculated daily atmospheric transmissivity values from the Bristow and Campbell (1984) model (Equations 2.2-2.4).

Table 2.3: SURFRAD network information.

Site Name	Latitude	Longitude	Elevation	Time Zone	Installed
Bondville, IL	40.0519° N	88.3731° W	230 m	UTC-6	April 1994
Boulder, CO	40.1249° N	105.2368° W	1689 m	UTC-7	July 1995
Desert Rock, NV	36.6237° N	116.0195° W	1007 m	UTC-8	March 1998
Fort Peck, MT	48.3078° N	105.1017° W	634 m	UTC-7	November 1994
Goodwin Creek, MS	34.2547° N	89.8729° W	98 m	UTC-6	December 1994
Penn State, PA	40.7201° N	77.9309° W	376 m	UTC-5	June 1998
Sioux Falls, SD	43.7340° N	96.6233° W	473 m	UTC-6	June 2003

Table 2.4: The time period and data used in the study.

Site Name	Time period	Total years	Missing data
Bondville, IL	Jan 1996 to Dec 1998 and Jan 2000 to Dec 2015	19	0.32%
Boulder, CO	Jan 1996 to Dec 2015	20	0.05%
Desert Rock, NV	Jan 1999 to Dec 2011 and Jan 2013 to Dec 2015	16	0.82%
Fort Peck, MT	Jan 1997 to Dec 2015	19	0.61%
Goodwin Creek, MS	Jan 1996 to Dec 2002 and Jan 2005 to Dec 2015	18	0.71%
Penn State, PA	Jan 1999 to Dec 2015	17	1.50%
Sioux Falls, SD	Jan 2004 to Dec 2006 and Jan 2008 to Dec 2015	11	0.10%

Figure 2.1: A geographical map of SURFRAD stations located in the USA.

2.2.7. Statistical validation methods

In the present study, the predictive efficiency of the model was tested using the mean bias error (MBE) and the mean absolute bias error ($MABE$). These terms are defined by the following equations;

$$MBE = \frac{1}{n}\sum_{i=1}^{n}(y_i - x_i) \tag{2.14}$$

$$MABE = \frac{1}{n}\sum_{i=1}^{n}|y_i - x_i| \tag{2.15}$$

where x_i is the i th measured value, y_i is the i th calculated value, and n is the total number of observations. The MBE is a measure of the systematic error of a model. It evaluates the tendency of a model to under- or overestimate the measured values and is for an accurate model is equal to zero (Willmott and Matsuura, 2005). The $MABE$ is a measure of the goodness of the fit for a model, and a natural measure of average error and a good test for inter-comparisons of the average model performance error. For precise data modeling $MABE$ should be close to zero (Willmott and Matsuura, 2005). We also provide

the Pearson correlation coefficient between the observed and modelled data. The Pearson correlation produces a sample correlation coefficient, r, which measures the strength and direction of linear relationships, negative or positive, between paired continuous variables.

2.3. Results and discussions

2.3.1. All years: daily radiation verification

Pearson correlation test results showed a strong positive correlation between the measured and estimated irradiance values, and this correlation increased from cloudy to sunny days (Table 2.5), except Fort Peck and Penn State, which had very small differences in correlation between partly cloudy and sunny days (Table 2.5). Considering all the stations together for all study years with data, in case of cloudy days, there was a significant positive correlation (r = 0.55; Table 2.5) and partly cloudy and sunny days showed a stronger positive correlation (r = 0.85 and r = 0.89 respectively; Table 2.5).

The result showed the $MABE$ decreased significantly from cloudy (about 112%) and partly cloudy (about 38%) to sunny days (about 18%) (Table 2.5). This error was more than three times larger under cloudy sky conditions than partly cloudy and more than six times larger in cloudy days than sunny days (Figure 2.3b).

MBE calculations showed the model overestimated the measured daily irradiance for cloudy days (about 88%) (Table 2.5; Figures 2.3d). In partly cloudy conditions, the overestimation (about 16%) slightly decreased compared to the cloudy days (Table 2.5; Figure 2.3d). However, clear or sunny days showed underestimations relative to the

observed values (about 8%) (Table 2.5; Figure 2.3d). The only exception was Fort Peck station with underestimations on partly cloudy days (Figure 2.3d).

The results showed the model is less able to account for partly cloudy and cloudy days. However it gives a reasonable estimation for solar radiation during clear and sunny days, taking into account the average 8% percent underestimation or 18% error in overall model performance. One of the likely sources of error is using a value for maximum atmospheric transmissivity of 0.7 in Bristow-Campbell model (1984) although this value is known to differ with elevation and air particle content (Bristow and Campbell, 1984). Variable maximum atmospheric transmissivity can be applied by using the reformulated Bristow-Campbell model by Thornton and Running (1998); however, their model uses precipitation and humidity data plus air temperature data. The $MABE$ and MBE in estimating daily solar radiation in clear and sunny days using the model proposed in this study, which are around 18% and 8%, respectively, are reasonable compared to the same errors in estimation of daily solar radiation by Thornton and Running (1998) which are 15% and 4%, respectively. The average MBE of our model (8%) on clear and sunny days is also within the range of MBE of the Solei-32 (Miklánek and Mészároš, 1993; Ruiz-Arias et al., 2009), Solar Analyst (Dubayah and Rich, 1995; Fu and Rich, 2002; Ruiz-Arias et al., 2009), SRAD (Wilson and Gallant, 2000; Ruiz-Arias et al., 2009) and r.sun (Šúri and Hofierka, 2004; Ruiz-Arias et al., 2009) models in the same sky condition, which is under 10%. However, our model depends mainly on air temperature data, whereas other models need accurate radiation, cloudiness, and/or satellite data as input. The TRAD model (Equation 2.1) is also a function of total monthly radiation estimated by Solar Analyst (Dubayah and Rich, 1995; Fu and Rich, 2002; Ruiz-Arias et al., 2009). Atmospheric

attenuation for calculating total monthly radiation in Solar Analyst (Dubayah and Rich, 1995; Fu and Rich, 2002; Ruiz-Arias et al., 2009) was applied by using the estimated average annual $K_{T\,d_{B-C\,(sl)}}$ and $K_{D\,d_{Ca}}$, which may affect the results and consequently the daily solar radiation estimation in the TRAD model (Equation 2.1). Furthermore, the accuracy of the measured data should be considered (accuracy of the pyranometer is about 5%).

Desert Rock station showed the best overall model performance ($MABE$ about 17%) between all other stations when considering all sky conditions (Table 2.5). This is because this station had the highest average percentage of clear and sunny days (89%) (Figure 2.2).

2.3.2. All years: daily atmospheric transmissivity verification

The Pearson correlation test between the estimated and measured daily atmospheric transmissivity values in cloudy and partly cloudy conditions applied for all the study years showed that there was a low positive correlation between the estimated and measured values in all stations, except for Desert Rock and Boulder in cloudy days and Sioux Falls in partly cloudy days (Table 2.5). These correlations also increased from cloudy and partly cloudy to sunny days in all stations except in Fort Peck (Table 2.5).

The $MABE$ for daily atmospheric transmissivity considerably higher for cloudy days (about 135%) than partly cloudy days (about 40%) (Table 2.5; Figure 2.3a). The MBE test showed the Bristow-Campbell model (Bristow and Campbell, 1984) overestimated the measured daily atmospheric transmissivity for cloudy days (118%) (Figure 2.3c). Overestimations for partly cloudy days (about 25%) decreased compared to the cloudy days (Figure 2.3c). However, clear or sunny days showed underestimations (about 9%) (Figure

3c). The only exception was Fort Peck station with overestimations on partly cloudy days (Figure 2.3c).

The result showed that the Bristow and Campbell (1984) model gives better estimation (about 15% error) of daily atmospheric transmissivity for sunny days than for partly cloudy or cloudy sky conditions, which also describes the performance of the daily solar radiation model using the TRAD model (Equation 2.1) in sunny and clear days. The average MBE of Bristow and Campbell (1984) considering all study years and sky conditions together is around 4% (Table 2.5).

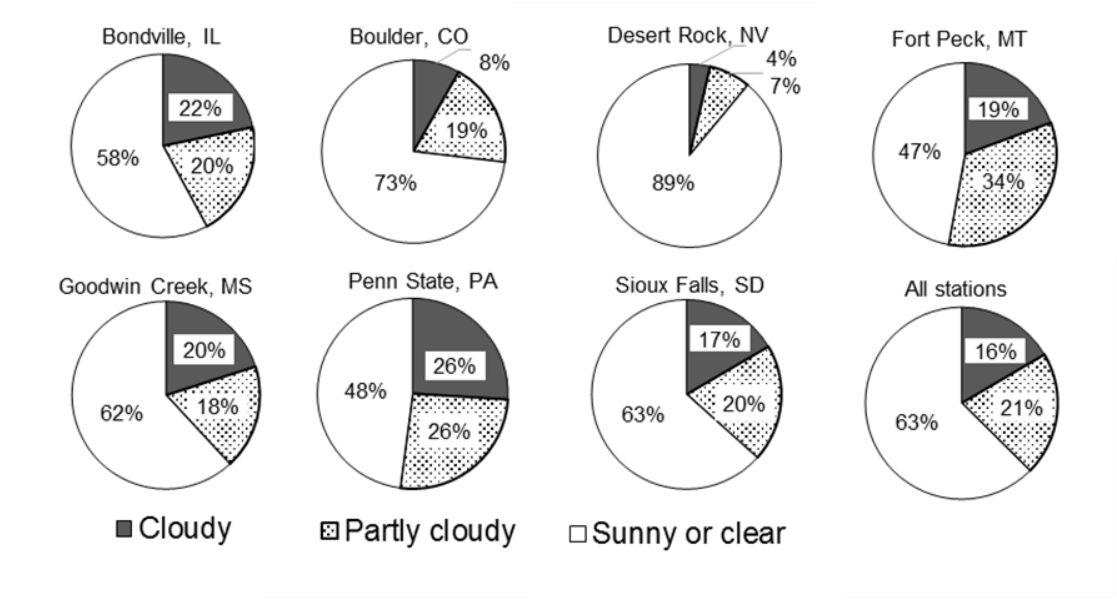

Figure 2.2: Average percentage of each sky condition in the different sites.

Table 2.5: Statistical comparison of the observed daily atmospheric transmissivity and daily irradiance against the corresponding modelled values using $MBE, MABE$, and Pearson correlation coefficients (r) between the observed and modelled values for each study site individually, and also for all the seven sites together in their total study years (MBE and $MABE$ in % are related to the mean observed value).

Station Name	Daily atmospheric transmissivity					
	MBE		MABE		r	n
	(%)		(%)			
All sky conditions						
Bondville, IL	6.10	0.03	26.80	0.13	0.57**	6918
Boulder, CO	-3.20	-0.02	23.00	0.13	0.35**	7301
Desert Rock, NV	-12.50	-0.08	19.00	0.13	0.45**	5796
Fort Peck, MT	20.0	0.09	33.00	0.15	0.46**	6897
Goodwin Creek, MS	5.80	0.03	23.00	0.11	0.62**	6528
Penn State, PA	10.10	0.05	29.70	0.14	0.61**	6116
Sioux Falls, SD	8.60	0.04	32.20	0.16	0.13**	4013
Combined data from all stations	3.77	0.02	25.10	0.13	0.50**	43569
Daily atmospheric transmissivity ≤ 0.30 (Cloudy sky)						
Bondville, IL	108.0	0.19	130.2	0.23	0.12**	1503
Boulder, CO	135.05	0.26	148.73	0.28	NSS	599
Desert Rock, NV	127.05	0.23	138.81	0.26	NSS	209
Fort Peck, MT	108.11	0.22	124.99	0.25	0.22**	1335
Goodwin Creek, MS	119.97	0.19	136.73	0.22	0.06*	1309
Penn State, PA	90.24	0.16	115.44	0.20	0.14**	1589
Sioux Falls, SD	198.17	0.36	201.09	0.37	0.10**	665
Combined data from all stations	117.65	0.21	135.58	0.24	0.15**	7209
0.30 < daily atmospheric transmissivity < 0.50 (Partly cloudy sky)						
Bondville, IL	22.16	0.08	38.44	0.15	0.18**	1409
Boulder, CO	24.1	0.10	36.47	0.15	0.12**	1363
Desert Rock, NV	20.88	0.08	35.18	0.15	0.15**	429
Fort Peck, MT	34.50	0.14	48.49	0.19	0.17**	2313
Goodwin Creek, MS	20.68	0.08	33.51	0.14	0.20**	1180
Penn State, PA	17.04	0.06	38.26	0.15	0.22**	1598
Sioux Falls, SD	33.98	0.13	45.93	0.18	NSS	805
Combined data from all stations	25.48	0.10	40.49	0.16	0.16**	9097
Daily atmospheric transmissivity ≥ 0.50 (Sunny and clear sky)						
Bondville, IL	-7.49	-0.04	13.90	0.09	0.22**	4006
Boulder, CO	-12.05	-0.08	16.92	0.11	0.15**	5339
Desert Rock, NV	-15.53	-0.11	16.99	0.12	0.27**	5158
Fort Peck, MT	1.16	0.01	13.28	0.08	0.23**	3249
Goodwin Creek, MS	-6.16	-0.04	11.82	0.08	0.30**	4039
Penn State, PA	-4.31	-0.03	13.90	0.09	0.28**	2929
Sioux Falls, SD	-10.64	-0.06	16.70	0.10	0.10**	2543
Combined data from all stations	-8.86	-0.05	15.02	0.10	0.19**	27263
Station Name	**Daily irradiance**					
	MBE		**MABE**		**r**	**n**
	(%)		(%)			
All sky conditions						
Bondville, IL	0.40	0.74	27.50	45.96	0.82**	6918
Boulder, CO	3.30	6.35	27.70	52.63	0.78**	7301
Desert Rock, NV	-10.30	-24.25	17.30	40.65	0.88**	5796
Fort Peck, MT	-2.50	-3.90	24.80	39.87	0.88**	6897

Goodwin Creek, MS	3.10	5.60	24.40	44.59	0.80**	6528
Penn State, PA	9.60	14.86	30.30	47.02	0.84**	6116
Sioux Falls, SD	1.50	2.50	27.00	44.87	0.83**	4013
Combined data from all stations	0.28	0.49	25.27	45.26	0.83**	43569
Daily atmospheric transmissivity ≤ 0.30 (Cloudy sky)						
Bondville, IL	89.1	44.73	111.10	55.77	0.62**	1503
Boulder, CO	145.77	89.29	157.89	96.70	0.45**	599
Desert Rock, NV	143.53	74.73	155.15	80.78	0.41**	209
Fort Peck, MT	41.75	21.74	77.98	40.61	0.67**	1335
Goodwin Creek, MS	106.02	52.04	124.72	61.22	0.36**	1309
Penn State, PA	76.50	38.88	102.46	52.07	0.55**	1589
Sioux Falls, SD	90.78	51.20	115.01	64.87	0.63**	665
Combined data from all stations	87.79	45.68	111.65	58.09	0.55**	7209
0.30 < daily atmospheric transmissivity < 0.50 (Partly cloudy sky)						
Bondville, IL	18.33	24.40	36.51	48.62	0.84**	1409
Boulder, CO	33.76	46.98	44.79	62.34	0.85**	1363
Desert Rock, NV	23.30	29.86	36.82	47.18	0.83**	429
Fort Peck, MT	-5.76	-6.32	38.78	42.55	0.87**	2313
Goodwin Creek, MS	19.84	29.41	33.40	49.51	0.78**	1180
Penn State, PA	17.84	22.92	38.48	49.45	0.82**	1598
Sioux Falls, SD	18.20	22.36	40.60	49.90	0.85**	805
Combined data from all stations	15.96	20.43	38.60	49.44	0.85**	9097
Daily atmospheric transmissivity ≥ 0.50 (Sunny and clear sky)						
Bondville, IL	-10.86	-24.25	18.57	41.47	0.90**	4006
Boulder, CO	-6.15	-13.35	20.84	45.24	0.90**	5339
Desert Rock, NV	-12.81	-32.22	15.40	38.72	0.92**	5158
Fort Peck, MT	-5.34	-12.91	15.60	37.72	0.87**	3249
Goodwin Creek, MS	-6.84	-16.12	16.05	37.81	0.88**	4039
Penn State, PA	-1.16	-2.61	19.03	42.78	0.89**	2929
Sioux Falls, SD	-7.90	-16.50	18.11	37.83	0.92**	2543
Combined data from all stations	-7.87	-18.13	17.63	40.61	0.89**	27263

* significant at the 95% confidence level.
** significant at the 99% confidence level.
NSS not statistically significant.

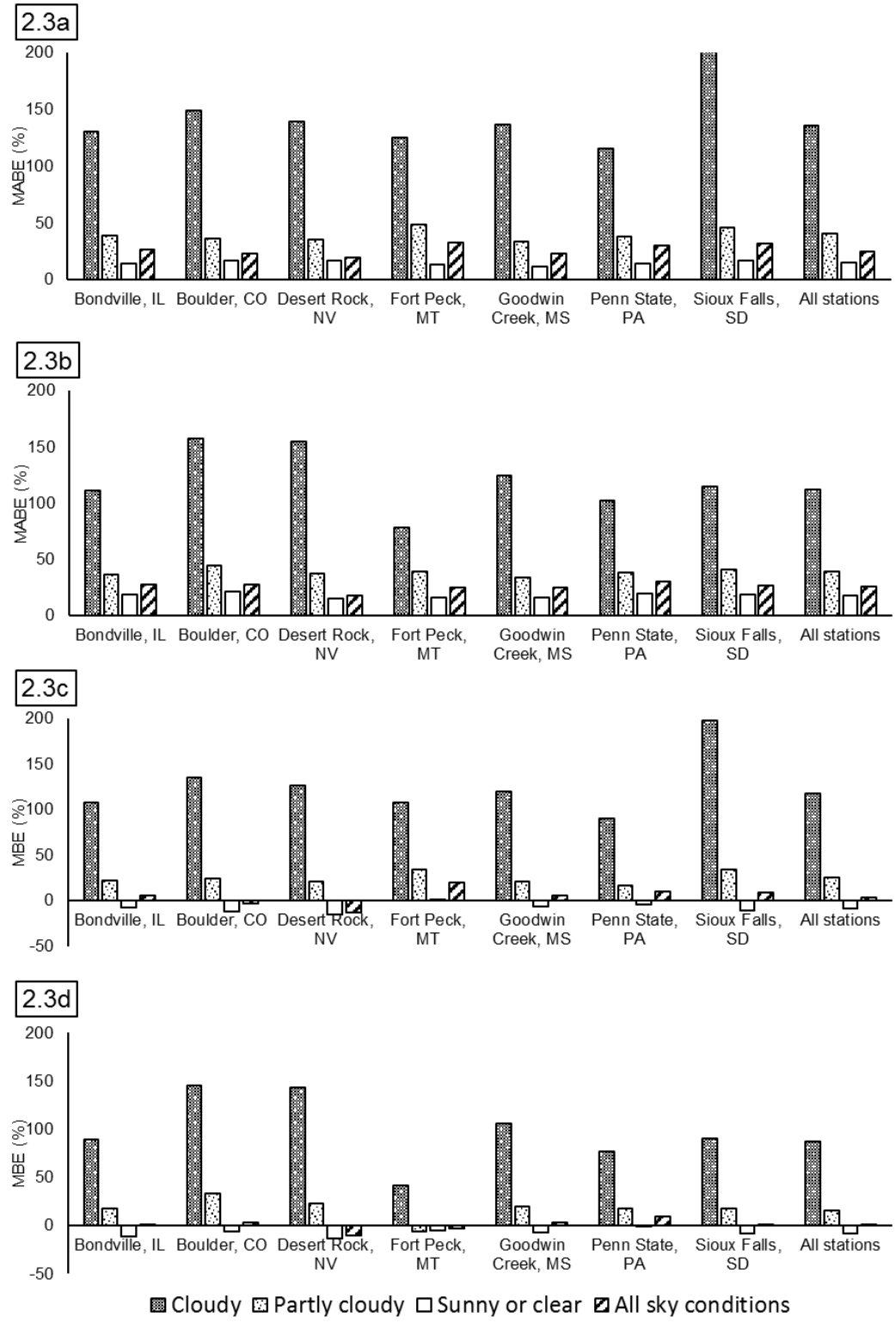

Figure 2.3a-d: $MABE$ (%) of the estimated daily atmospheric transmissivity and estimated daily irradiance (2.3a and 2.3b) and MBE (%) of the estimated daily atmospheric transmissivity and estimated daily irradiance (3c and 3d) for each sky condition in different sites for the entire study time period.

2.3.3. Year 2015: Daily radiation verification

The result of Pearson correlation tests showed that there always was a strong positive correlation between the measured and estimated irradiance values, and this correlation increased from cloudy to sunny days in year 2015 (Table 2.6). However, exceptions were very small differences in correlation between partly cloudy and sunny days in Fort Peck and Penn State (Table 2.6).

The result showed the $MABE$ declined significantly from cloudy (105%) and partly cloudy (about 38%) to sunny days (17%) (Table 2.6). This error was more than three times higher under cloudy days than partly cloudy, and more than six times higher in cloudy sky conditions than sunny (Figure 2.4b).

MBE result indicated that the model overestimated the measured daily irradiance for cloudy days (about 83%) (Table 2.6; Figures 2.4d and 2.5a-h). In partly cloudy days, the overestimation (about 19%) decreased relative to the cloudy conditions (Table 2.6; Figures 2.4d and 2.5a-h). However, clear or sunny sky condition showed underestimations relative to the observed values (6%) (Table 2.6; Figures 2.4d and 2.5a-h). The only exception was Fort Peck station with underestimations in partly cloudy days (Figures 2.4d and 2.5a-h).

2.3.4. Year 2015: Daily atmospheric transmissivity verification

In 2015, there was no correlation between the estimated and measured daily atmospheric transmissivity values in cloudy and partly cloudy days in any stations, except there were significant correlations in Fort Peck and Penn State in cloudy days and Goodwin

Creek and Penn State in partly cloudy days (Table 2.6). On sunny days, there was a positive correlation in all stations except Fort Peck and Bondville (Table 2.6).

The $MABE$ for daily atmospheric transmissivity was considerably higher for cloudy days (145%) than partly cloudy days (42%) (Table 2.6; Figure 2.4a). The MBE test showed Bristow-Campbell model (Bristow and Campbell, 1984) overestimated the measured daily atmospheric transmissivity for cloudy days (about 130%) (Figure 2.4c). Overestimations for partly cloudy days (about 28%) decreased compared to the cloudy days (Figure 2.4c). However, clear or sunny days showed underestimations (about 9%) (Figure 2.4c). The only exception was Fort Peck station with overestimations on sunny sky conditions (Figure 2.4c).

Table 2.6: Same as Table 2.5 in 2015.

Station Name	Daily atmospheric transmissivity MBE (%)		MABE (%)		r	n
All sky conditions						
Bondville, IL	5.49	0.03	39.75	0.20	NSS	365
Boulder, CO	-1.93	-0.01	22.05	0.12	0.50**	365
Desert Rock, NV	-10.07	-0.06	17.85	0.11	0.42**	363
Fort Peck, MT	22.25	0.11	33.66	0.15	0.50**	362
Goodwin Creek, MS	8.36	0.04	22.07	0.10	0.72**	364
Penn State, PA	10.84	0.05	29.86	0.14	0.57**	365
Sioux Falls, SD	7.03	0.04	31.55	0.16	0.18**	365
Combined data from all stations	5.23	0.03	27.51	0.14	0.44**	2549
Daily atmospheric transmissivity ≤ 0.30 (Cloudy sky)						
Bondville, IL	181.88	0.31	197.90	0.34	NSS	72
Boulder, CO	80.19	0.16	93.65	0.18	NSS	39
Desert Rock, NV	120.71	0.26	124.55	0.27	NSS	13
Fort Peck, MT	121.85	0.23	141.60	0.27	0.34**	73
Goodwin Creek, MS	90.68	0.15	108.50	0.18	NSS	85
Penn State, PA	105.79	0.19	121.69	0.22	0.25*	93
Sioux Falls, SD	228.56	0.38	228.56	0.38	NSS	54
Combined data from all stations	130.29	0.24	144.72	0.26	0.14**	431
0.30 < daily atmospheric transmissivity < 0.50 (Partly cloudy sky)						
Bondville, IL	33.93	0.13	51.27	0.20	-0.24*	84
Boulder, CO	28.00	0.12	42.96	0.18	NSS	71
Desert Rock, NV	20.53	0.08	32.23	0.13	NSS	33
Fort Peck, MT	38.08	0.15	46.14	0.18	NSS	124
Goodwin Creek, MS	25.85	0.10	36.20	0.14	0.28*	69

Penn State, PA	13.11	0.05	35.72	0.14	0.24*	95
Sioux Falls, SD	29.65	0.11	44.26	0.17	NSS	81
Combined data from all stations	28.18	0.11	42.42	0.17	NSS	555
Daily atmospheric transmissivity ≥ 0.50 (Sunny and clear sky)						
Bondville, IL	-17.23	-0.11	22.78	0.15	NSS	209
Boulder, CO	-10.75	-0.07	15.24	0.10	0.21**	255
Desert Rock, NV	-13.58	-0.09	15.63	0.11	0.19**	317
Fort Peck, MT	5.18	0.03	12.18	0.07	NSS	165
Goodwin Creek, MS	-3.9	-0.02	10.05	0.06	0.28**	210
Penn State, PA	-4.36	-0.02	13.96	0.09	0.16*	177
Sioux Falls, SD	-11.14	-0.07	16.96	0.11	0.19**	230
Combined data from all stations	-9.15	-0.06	15.46	0.10	0.11**	1563
	Daily irradiance					
	MBE		**MABE**			
Station Name	(%)		(%)		**r**	**n**
All sky conditions						
Bondville, IL	-0.58	-0.97	27.49	46.50	0.81**	365
Boulder, CO	5.42	10.02	28.14	52.07	0.80**	365
Desert Rock, NV	-5.99	-13.75	16.10	36.96	0.87**	363
Fort Peck, MT	0.31	0.49	22.64	36.03	0.88**	362
Goodwin Creek, MS	7.25	12.80	23.93	42.28	0.83**	364
Penn State, PA	9.61	15.15	31.00	48.84	0.82**	365
Sioux Falls, SD	2.05	3.39	28.07	46.54	0.81**	365
Combined data from all stations	2.19	3.89	24.89	44.15	0.83**	2549
Daily atmospheric transmissivity ≤ 0.30 (Cloudy sky)						
Bondville, IL	79.23	37.31	105.08	49.48	0.70**	72
Boulder, CO	87.81	58.79	100.27	67.13	0.42**	39
Desert Rock, NV	114.58	69.23	117.61	71.05	0.80**	13
Fort Peck, MT	54.45	25.46	94.30	44.09	0.72**	73
Goodwin Creek, MS	82.64	46.45	100.43	56.45	0.55**	85
Penn State, PA	77.68	40.07	98.18	50.65	0.66**	93
Sioux Falls, SD	119.93	57.59	141.50	67.95	0.64**	54
Combined data from all stations	82.78	43.16	105.03	54.76	0.63**	431
0.30 < daily atmospheric transmissivity < 0.50 (Partly cloudy sky)						
Bondville, IL	23.74	35.40	34.09	50.83	0.84**	84
Boulder, CO	39.20	50.90	54.47	70.73	0.84**	71
Desert Rock, NV	26.76	38.13	36.88	52.54	0.83**	33
Fort Peck, MT	-4.13	-4.75	31.57	36.33	0.90**	124
Goodwin Creek, MS	27.26	38.95	38.81	55.46	0.83**	69
Penn State, PA	15.39	20.47	36.50	48.55	0.84**	95
Sioux Falls, SD	19.71	25.42	37.31	48.11	0.85**	81
Combined data from all stations	18.95	25.06	37.83	50.03	0.85**	555
Daily atmospheric transmissivity ≥ 0.50 (Sunny and clear sky)						
Bondville, IL	-13.13	-28.78	19.95	43.73	0.90**	209
Boulder, CO	-4.03	-8.81	20.40	44.57	0.91**	255
Desert Rock, NV	-9.19	-22.56	13.82	33.94	0.92**	317
Fort Peck, MT	-2.73	-6.61	13.32	32.24	0.88**	165
Goodwin Creek, MS	-3.98	-9.40	13.62	32.22	0.91**	210
Penn State, PA	-0.45	-1.02	21.12	48.02	0.83**	177
Sioux Falls, SD	-8.28	-17.08	19.85	40.97	0.90**	230
Combined data from all stations	-6.33	-14.45	17.18	39.20	0.89**	1563

* significant in 95% confidence level.
** significant in 99% confidence level.
NSS not statistically significant.

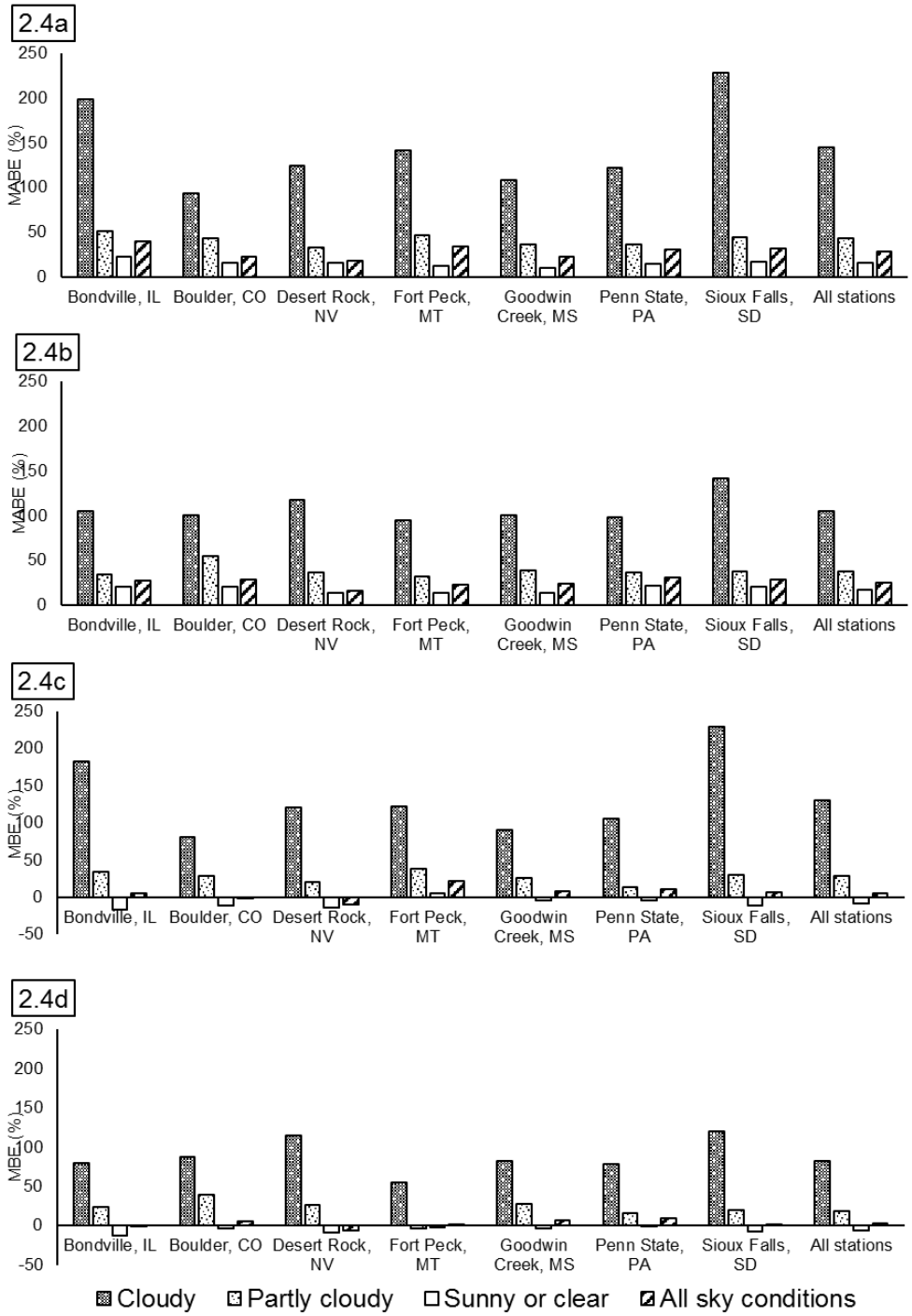

Figure 2.4a-d: $MABE$ (%) of the estimated daily atmospheric transmissivity and estimated daily irradiance (4a and 4b) and MBE (%) of the estimated daily atmospheric transmissivity and estimated daily irradiance (4c and 4d) for each sky condition in different sites for 2015.

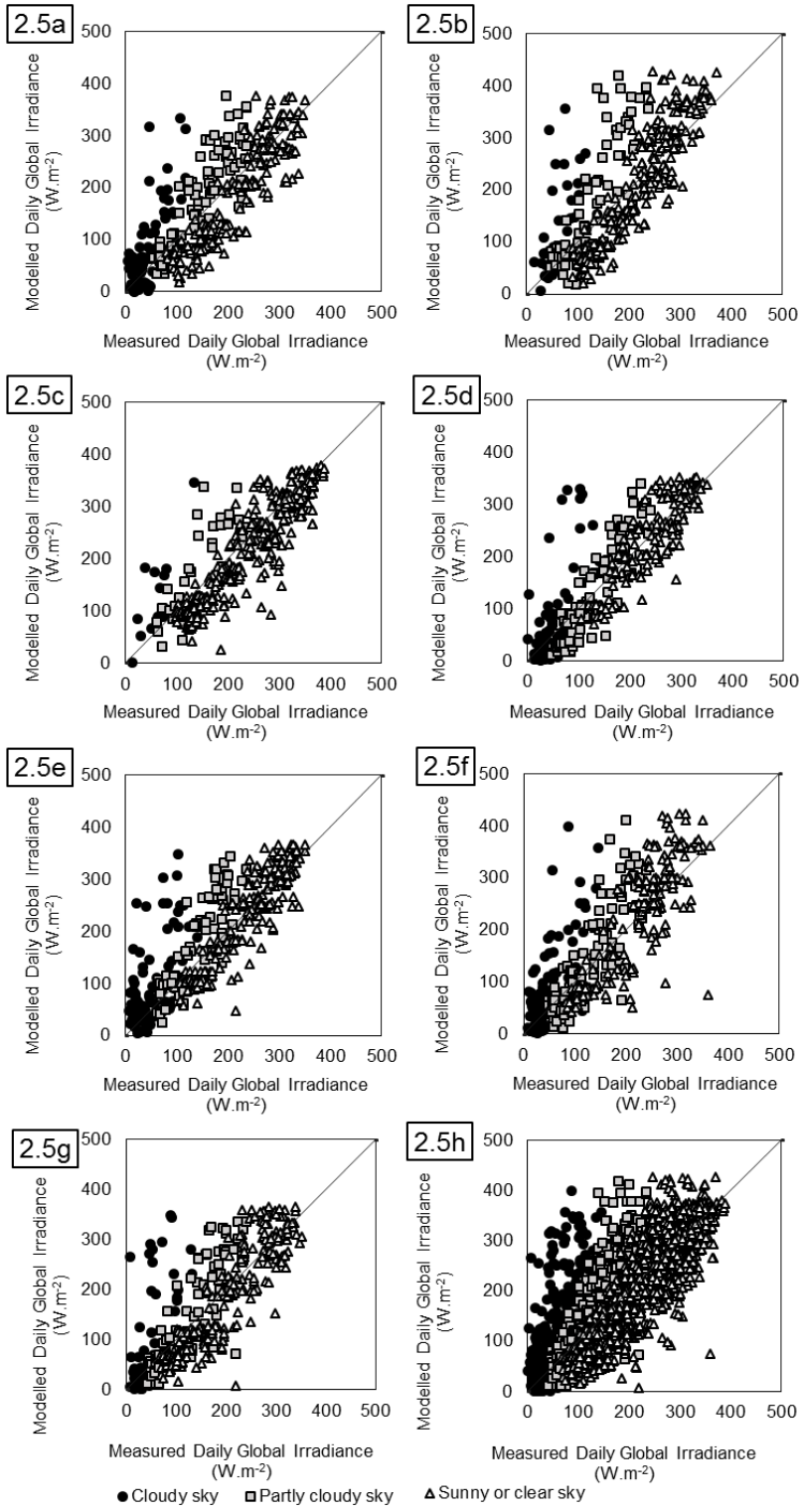

Figure 2.5a-h: Comparison of the measured versus predicted daily irradiance ($W \cdot m^{-2}$) for Bondville, IL (5a), Boulder, CO (5b), Desert Rock, NV (5c), Fort Peck, MT (5d), Goodwin Creek, MS (5e), Penn State, PA (5f), Sioux Falls, SD (5g) and all the SURFRAD stations (5h) in 2015, as an example of a single year.

2.4. Conclusions

In Chapter 2, a method for estimating daily solar radiation by using only maximum and minimum air temperature, topography, and time of year was presented, and will be used as an input for the hydrometeorological modelling presented in Chapter 3. The TRAD model, a daily solar radiation model that used estimated daily atmospheric transmissivity from the Bristow and Campbell (1984) model and calculated total monthly solar radiation values by Solar Analyst (Dubayah and Rich, 1995; Fu and Rich, 2002; Ruiz-Arias et al., 2009) was developed. Estimated average annual atmospheric transmissivity at sea level and diffuse fraction according to models of Bristow and Campbell (1984) and Carroll (1985) (Carroll, 1985) to calculate total monthly solar radiation using Solar Analyst (Dubayah and Rich, 1995; Fu and Rich, 2002; Ruiz-Arias et al., 2009) were used. In addition, hourly solar radiation values can be calculated using the ratio between daily and hourly radiation estimates suggested in previous literature, combined with the estimated daily insolation from the method presented in this chapter. The method was validated using seven different sites in climatologically different areas across the United States. Overall, results showed that daily solar radiation can be estimated very well with $MABE$ of about 40 to 53 $W \cdot m^{-2}$ or MBE of ±10% under all sky conditions between the seven sites by using the presented method, which is an improvement over previously used methods with MBE of under 10% because the modified approach and model presented here also require significantly less input data. This method can be very useful especially for those stations with substantially higher number of sunny days than cloudy or partly cloudy days, assuming the availability of air temperature data. The estimated values for those days that the model is not able to estimate accurately can be corrected by using available measured data. The implemented

DEM environment of this method makes it applicable in many studies that need spatial estimation of solar radiation.

Chapter 3 : Climate change impacts on water supply and demand in an Okanagan-Similkameen Subwatershed, British Columbia, Canada

3.1. Introduction

The hydrological cycle on the surface of the Earth cannot be treated as a simple system because human influence has altered this system, directly through various activities related to land and water resource management, and indirectly by increasing the variability of climate through increasing emissions of greenhouse gases (Mauser and Bach, 2009).

Intra-annually, the hydrological cycle in mountain watersheds is driven mostly by precipitation, snow accumulation and subsequent melting, and by growing season evapotranspiration (Barnett et al., 2005). Changes in the hydrological cycle and subsequent changes in water yield, evapotranspiration, and soil moisture as a result of climate change can affect water supply, and subsequently affect the rates of vegetation growth and water use in mountain watersheds (Neilsen et al., 2006). Climate change will have a significant impact on mountain hydrology, altering water supply and demand, and increasing stress on water resources, vegetation cover, the agricultural sector, wildlife, human settlements, and economy, along with non-climate change anthropogenic forces (Hamlet and Lettenmaier, 1999; Cohen et al., 2000; Miles et al., 2000; Cohen et al., 2006; Merritt et al., 2006; Neilsen et al., 2006; Harma et al., 2012).

Anthropogenic climate change is predicted to alter climate and physical systems in mountain areas of southern British Columbia, Canada. Climate change is expected to result in higher air temperatures, earlier snowmelt, decreased spring snow water equivalent, more rainfall events than snow, increases in crop water requirements (especially during periods

of high water demand), longer growing season, increases in winter runoff, decreases in summer runoff, reductions in average peak annual discharge, increases in winter and spring stream flow, and decreases in summer stream flow in this region (Leith and Whitfield, 1998; Hamlet and Lettenmaier, 1999; Cohen et al., 2000; Morrison et al., 2002; Cohen et al., 2006; Merritt et al., 2006; Neilsen et al., 2006; Jost and Weber, 2012; Shrestha et al., 2012; Schnorbus et al., 2014; Najafi et al., 2017).

Hydrologic climate change impact assessments are investigated using general or regional circulation models (GCMs or RCMs) and hydro-metrological models. However, GCMs or RCMs must be downscaled to provide higher temporal and/or spatial resolutions often required for use in hydro-metrological models for impact assessment studies, especially in complex landscapes such as mountain area (Wang et al., 2012; Wang et al., 2016). There are two different methods for impact assessments using GCM or RCM scenarios; change factor (CF), in which GCMs or RCMs projected future climate changes are applied to the meteorology of a baseline, and statistical downscaling (SD), in which GCMs or RCMs climate variables are applied to statistical transfer functions in order to calculate meteorological series with point-scale (Diaz-Nieto and Wilby, 2005). Diaz-Nieto and Wilby (2005), explored the suitability of these methods under baseline (1961-1990) and climate change scenarios (2020's, 2050's and 2080's) for low streamflow in the River Thames, UK. They showed stream flow will decrease in late summer and fall under both techniques in the future; however, the SD method shows more detailed and complex changes in the future compared with the CF method. On the other hand, the SD method is more time-consuming and needs a large range of transfer functions and high-quality observed data. Diaz-Nieto and Wilby (2005) concluded these two methods should be used

in a complementary way, because the CF method maps the future changes to the historical record and is more suitable for high-level assessments and vulnerable regions detections, while the SD method works better for impact assessments related to temporal sequencing and analysis of daily event persistence changes.

The effects of climate change on spring and summer water supply and spring and summer water demand related to the vegetation cover in a snow-dominated watershed (Olalla watershed, southern British Columbia, Canada) in the time-frame of 1961 to 2100 were assessed in Chapter 3. The GENESYS spatial hydrometeorological model (MacDonald et al., 2009) was applied to predict the potential changes for the ensembles of the 15 GCMs of the coupled model inter-comparison project (CMIP5) (Wang et al., 2012; Wang et al., 2016) for two Representative Concentration Pathways (RCP) greenhouse gas emission scenarios (RCP 4.5 and RCP 8.5) (Moss et al., 2010) for three different future periods, including 2020's (2011-2040), 2050's (2041-2070) and 2080's (2071-2100) relative to the 1961-1990 base period.

3.2. Materials and methods

3.2.1. Study subwatershed

The Olalla watershed is located in the Regional District of Okanagan-Similkameen, southern British Columbia, Canada. The total drainage area is about 181 km^2 and contributes flows to the Water Survey of Canada stream gauge located at the Keremeos Creek below Wills intake (Environment Canada ID: 08NL045) (Figure 3.1). The stream gauge was installed in April 29, 1971, and continues to operate.

The watershed is inside the Southern Thompson Plateau hydrologic zone which has a generally dry condition and also Interior Douglas Fir biogeoclimatic zone (Hectares BC, 2015; Regional District of Okanagan-Similkameen, 2011a). Normal (1961-1990) mean annual precipitation in the Olalla watershed is 520 mm with the highest (63 mm) and lowest (30 mm) precipitation received in December and October respectively (Wang et al., 2012; Wang et al., 2016), Figure 3.2). Normal (1961-1990) mean annual air temperature over the watershed is 4.7 ˚C; July and January are the warmest and coolest months with average air temperatures of 14.5 ˚C and -5.7 ˚C, respectively ((Wang et al., 2012; Wang et al., 2016), Figure 3.2).

Elevation in the watershed ranges between 476 to 2235 m a.s.l. The watershed is mostly dominated by rolling upland relief and glacial till material and has a broad flat valley infilled with post-glacial alluvial material (Regional District of Okanagan-Similkameen, 2011a). Most of the watershed soil (about 95%) has a course texture (loamy sand or sandy loam) with a well- to rapidly-drained condition which means the soil has high infiltration rates and low runoff potential (BC Ministry of Environment, 2016). The area has diverse land cover, with 75.7 % of the watershed covered by coniferous forests, mostly Interior Douglas Fir (IDF), 9.8% by alpine, barren surfaces, and subalpine, 7.3% by range lands, 1.8% by agriculture, 0.2% by open water, 2.4% by cutblocks and, 2.8% by predominantly built-up or developed lands and vegetation associated with these land covers (Hectares BC, 2015).

The town of Olalla in the valley of the watershed has grown over the past decades and there are different water licences including irrigation, conservation (storage), domestic, livestock and animal, waterworks and, others within the watershed (BC Government, 2018)

The most important recreation activity in the watershed is Apex Mountain Resort established in early 1960's, and which has been further developed in the early 1990s and which may cause soil erosion and consequently sediment loading into the creek (Regional District of Okanagan-Similkameen, 2011a). There were two environmental emergencies in the watershed associated with the Apex Mountain Resort development: the failure of a sewage retention pond in 1991, and an erosion event in 1995 that caused a considerable amount of sediment loading into the watershed (Regional District of Okanagan-Similkameen, 2011a). Furthermore, there is a little chance for the creek to attenuate peak flows or deposit sediments along its way as there are no significant open water or wetlands along the creek (Regional District of Okanagan-Similkameen, 2011a).

A large wildfire burned a substantial portion of the forested area on the western ridge of the watershed in 1934 (Regional District of Okanagan-Similkameen, 2011a). The gradual recovery of the forest area after the fire can cause a downward trend in stream flow of the watershed after the fire (Regional District of Okanagan-Similkameen, 2011a). However, there has been no fire since, and because the formerly burned area is mostly covered by forest regrowth, currently no effect on the hydrologic regime of the watershed is assumed (Regional District of Okanagan-Similkameen, 2011a). Furthermore, the equivalent clearcut area (likely below 20%) in the Olalla watershed, including both infested by the Mountain Pine Beetle (MPB) and harvested area in the upper portion of the watershed, is not significant enough to affect the hydrologic regime (Regional District of Okanagan-Similkameen, 2011a).

A flood prevention plan provided for RDOS in 2011 showed that the peak flows have apparently decreased by 50% since 1948 in the Olalla watershed (Regional District of

Okanagan-Similkameen, 2011a). They also reported that this may be the result of a long-term climate change such as variation in runoff and precipitation in combination with land use and vegetation cover changes over the time, for example, related to recovery from wildfire. However, they considered the climate change assessment in the region beyond the scope of their work.

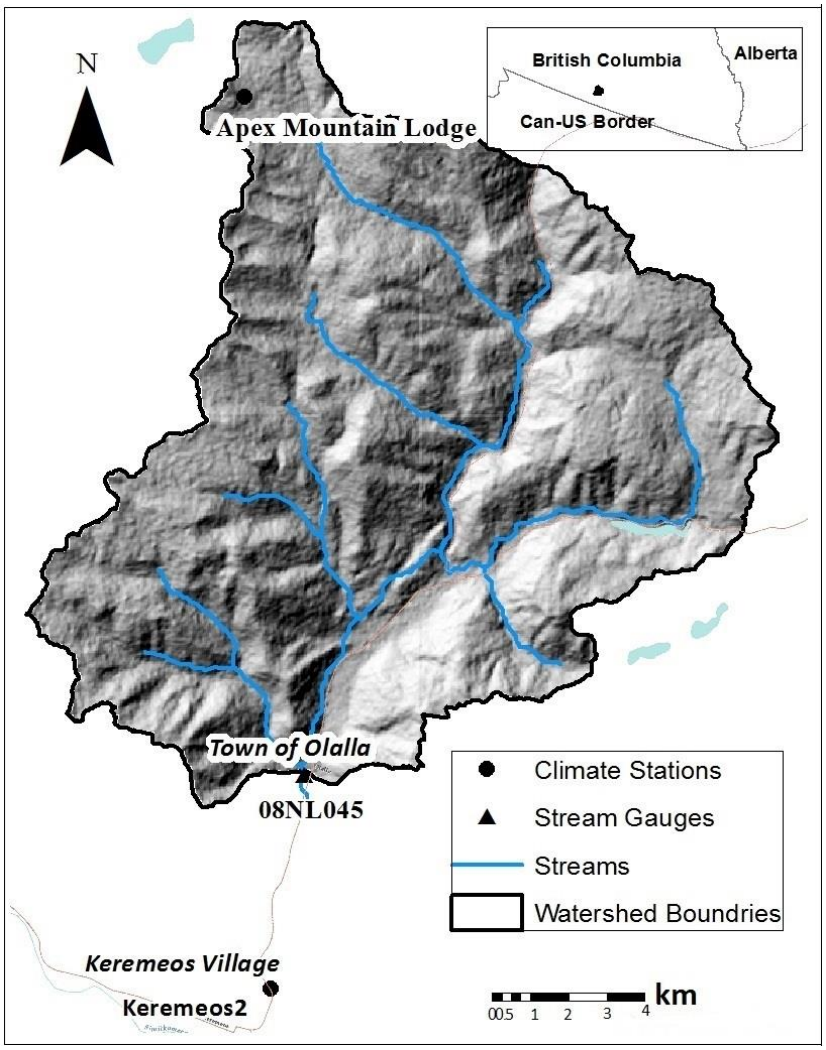

Figure 3.1: The Olalla watershed, Regional District of Okanagan-Similkameen, southern British Columbia, Canada.

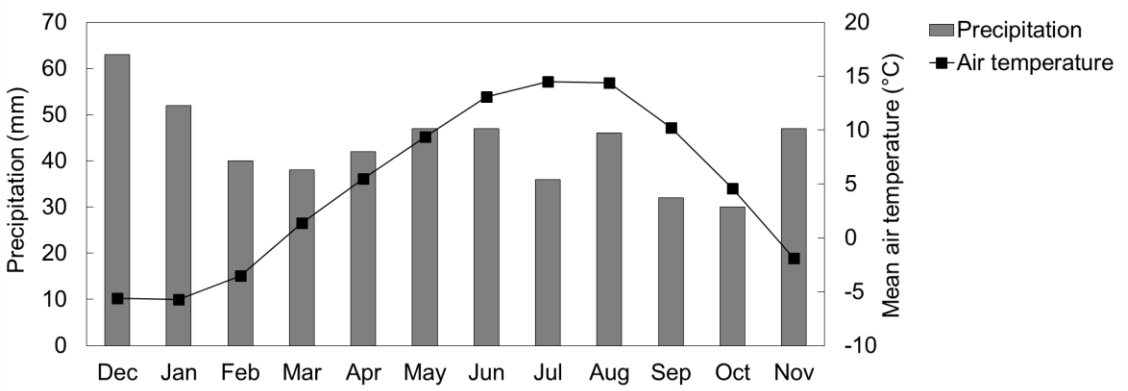

Figure 3.2: Average normal (1961-1990) mean monthly air temperature (˚C) and precipitation (mm) over the entire Olalla watershed.

3.2.2. Hydrometric data

There are four Environment Canada stream gauge records on Keremeos Creek (Environment Canada, 2015). Three of them were installed near the town of Olalla. The Olalla Creek at Olalla (08NL011) station operated for two years (1919-1921) and Keremeos Creek near Olalla (08NL10) operated from 1919 to 1971. The gauge was moved to Keremeos Creek below Willis intake (08NL045) on 29 April, 1971, which continues to operate, and serves as the stream gauge that was used in the current study. The drainage area changed slightly from 183 to 181 km^2 ((Regional District of Okanagan-Similkameen, 2011a), Figure 3.1). The fourth stream gauge station was located in Keremeos creek at Middle Bench road (08NL44) which was in operation for six years (1971-1977) (Figure 3.1).

Based on observed streamflow information at the Keremeos Creek below Willis intake (08NL045), the onset of snowmelt runoff in the Olalla watershed starts in April, when streamflow rises, with a peak in June and a receding in July and August (Figure 3.3).

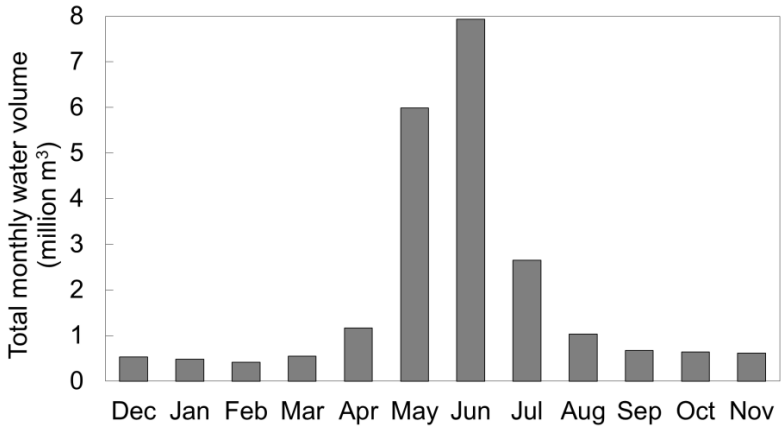

Figure 3.3: Historical average monthly water volume (million m^3) for the period of 1972 to 1999 in Olalla watershed.

There are no dams or reservoirs, groundwater points of diversions, or artesian wells in the watershed (BC Government, 2018). However, there are active domestic water licences that use water directly from the Keremeos Creek and its tributaries, and irrigation licences that use wells close to the creeks inside the Olalla watershed (BC Government, 2018). The irrigation season in the region is from April to the end of September for most of the irrigation users (Regional District of Okanagan-Similkameen, 2011b). We supposed that half of the total irrigation period water use (0.73 million m^3) is consumed during June and July and the other half during April, May, August and September (BC Government, 2018). We also estimated total annual (12 months) of about 0.50 million m^3 water use for the other licences including conservation (storage), domestic, livestock and animal, waterworks, and others (BC Government, 2018). Human water use was held constant during future simulations in order to test only the effect of changes in air temperature and precipitation on spring and summer water volume (million m^3). The total monthly human water use was subtracted from the simulated total monthly water volume.

3.2.3. Meteorological data

There are two climate stations within the watershed, with typically similar values of maximum air temperature (°C), minimum air temperature (°C), and precipitation (mm). Apex Mountain Lodge operated by Environment Canada at elevation of 1890 m (Figure 3.1) has available daily climate data from 1965 to 1971 (from the beginning of June 1965 to the end of October 1966 and from the beginning of December 1970 to the end of September 1971). There is also Apex Roadside or Apex Alpine at elevation of 1750 m with data from November 1997 to the present, which are close to the Apex Mountain Lodge and have hourly data collected electronically by Ministry of Transportation and Infrastructure (MoTI).

A climate station with the longest climate records available as input is needed as applications of the GENESYS model (MacDonald et al., 2009). Therefore, Keremeos 2 climate station, located at an elevation of 435 m a.s.l within the Keremeos village and in about five kilometres from the town of Olalla was selected as the base station ((Environment Canada, 2016), Figure 3.1). This station is closest to the watershed with the longest historical records (1924 to 2000). Continuous daily maximum and minimum air temperature and precipitation were obtained for 1961 to 1999 (the year 2000 was not selected because of the long gaps in data) (Environment Canada, 2016). There was not a significant gap in data (0.4% of the whole dataset) in the selected period and these minor gaps were infilled using a nearby climate station (Cawston Similkameen) and linear regression (Figure 3.4 and Table 3.1). Apex Mountain Lodge Environment Canada climate station is also selected for testing meteorological simulations of the model. The

Environment Canada climate station was preferred to MoTI climate station as both have nearly two years of available recorded data for model testing.

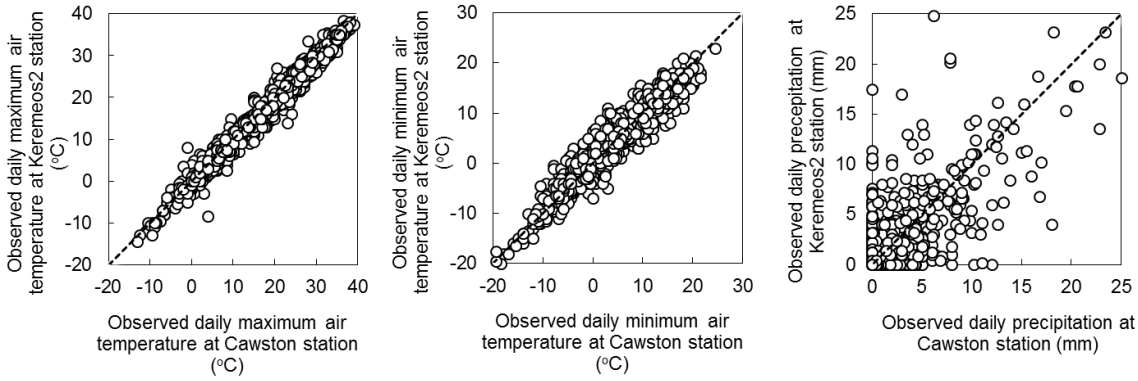

Figure 3.4: Observed daily climate variables at Cawston station (x) vs. Keremeos 2 station (y). The line represents the 1:1 line.

Table 3.1: Regression relationships between daily observed climate variables at Keremeos 2 station and Cawston station used to infill gaps in climate data at Keremeos 2 station using available daily data at Cawston station.

$y = a + bx$	Std. Error$_a$	t_a	p	Std. Error$_b$
Daily maximum air temperature (°C)				
$\mathbf{y = -0.211 + 0.984x}$	0.071	-2.95	<0.001	0.004
Daily minimum air temperature (°C)				
$\mathbf{y = 0.309 + 0.916x}$	0.065	4.73	<0.001	0.007
Daily precipitation (mm)				
$\mathbf{y = 0.349 + 0.729x}$	0.038	9.16	<0.001	0.014
t_b	**p**	**r^2**	**RMSE**	**n**
Daily maximum air temperature (°C)				
276.98	<0.001	0.98	1.6 °C	1458
Daily minimum air temperature (°C)				
133.94	<0.001	0.93	2.1 °C	1458
Daily precipitation (mm)				
53.04	<0.001	0.54	1.9 mm	2405

Daily solar radiation ($W \cdot m^{-2}$) was not available for the base station and calculated using the method presented in Chapter 2. Daily solar radiation for a non-slope surface or flat radiation for the base station is also calculated using the same method but without applying the DEM.

3.2.4. Spatial data

The watershed was divided into Hydrological Response Units (HRUs) using a Geographic Information System (GIS) overlay analysis in Esri ArcGIS. HRUs were defined by combining 100-m elevation bands using a 30 × 30 meter DEM ranging from 400 m to 2200 m (NASA LP DAAC, 2011), three solar radiation groups, and nine land cover types which resulted in delineation of 201 different HRUs. Land cover types included coniferous forests, cutblocks, barren surfaces, range lands, alpines, subalpine avalanche, agriculture, open water or wetlands, and also predominantly built-up or developed lands and vegetation associated with these land covers (Hectares BC, 2015). The normal (1961-1990) annual solar radiation over the watershed was calculated using ArcGIS Solar Analyst and average annual atmospheric attenuation for the normal period using the method presented in Chapter 2, and divided into three categories, low, medium and high receiving solar radiation surfaces ranges from 61.6 to 219.8 $w \cdot m^{-2}$.

The following physiographic characteristics were defined for each HRU. We provided mean elevation (m), area (ranging from 1049 m^2 to 6.9 km^2) and monthly Leaf Area Index (LAI) from MODIS LAI data set (NASA LP DAAC, 2000) which were considered to be constant at monthly time steps. Normal (1961-1990) mean monthly solar radiation ($w \cdot m^{-2}$) was estimated using Solar Analyst and normal (1961-1990) mean monthly atmospheric attenuation using the presented method in Chapter 2. Monthly maximum and minimum air temperature lapse rates ($^{\circ}C \cdot km^{-1}$) were derived from normal (1960-1990) monthly air temperature grid layers and are assumed to be constant at different months (Wang et al., 2012; Wang et al., 2016). Monthly precipitation values also derived for each HRU using spatial raster layers of precipitation (Wang et al., 2012; Wang et al., 2016).

Field Capacity (FC, mm) values were defined over the watershed using a GIS overlay analysis with soil texture data (BC Ministry of Environment, 2016), soil depth data (Agriculture and Agri-Food Canada, 1996) and generalized relationships between soil texture classes and plant available water holding capacity (Walker and Skogerboe, 1987). The GIS overlay analysis divided the watershed into five categories with average FC of around 38 mm, 90 mm, 135 mm, 210 mm, and 233 mm contributing to about 7%, 1%, 87%, 1% and 4% of total watershed area, respectively.

Monthly plant transpiration coefficients (PTCs) estimated for different land cover types in upper North Saskatchewan River Basin (UNSRB), Alberta (Nemeth, 2010) were used and then all monthly PTCs values were adjusted for our study area in order to take into account a drier climate in our watershed compared to UNSRB (BC Ministry of Agriculture Food and Fisheries, 2001). The monthly PTCs values for UNSRB were increased by 12% by finding an average ratio between PTCs for perennial crop and pasture in different stage of development recommended by BC Ministry of Agriculture Food and Fisheries (2001) for use in irrigation scheduling and PTCs for perennial crop and pasture presented by Nemeth (2010) in Alberta. PTCs for agricultural areas were calculated by taking the average between annual cropland and perennial crops or pasture for each month, and half of those monthly values were considered for urban and recreation activities (Table 3.2). PTCs were also considered similar to deciduous forest for cutblocks and as half of the monthly PTCs values for coniferous forest for barren surfaces.

Table 3.2: Plant transpiration coefficients (PTCs) for different land cover types in the Olalla watershed.

Land cover	Jan	Feb	Mar	Apr	May	Jun	Jul	Aug	Sep	Oct	Nov	Dec
Water/wetland	0.18	0.13	0.16	0.26	0.44	0.61	0.53	0.51	0.35	0.22	0.19	0.23
Range land	0.04	0.08	0.04	0.09	0.36	0.45	0.31	0.23	0.08	0.04	0.02	0.07
Agriculture	0.00	0.00	0.00	0.25	0.58	0.99	1.00	0.65	0.50	0.07	0.03	0.00
Barren surfaces	0.11	0.16	0.16	0.17	0.28	0.35	0.39	0.38	0.20	0.16	0.11	0.10
Cutblocks	0.10	0.09	0.09	0.12	0.26	0.72	0.96	0.85	0.66	0.16	0.13	0.09
Coniferous	0.21	0.32	0.32	0.34	0.57	0.70	0.77	0.76	0.39	0.32	0.22	0.20
Built-up	0.00	0.00	0.00	0.12	0.29	0.50	0.53	0.33	0.25	0.04	0.01	0.00

3.2.5. The GENESYS model

The GENESYS spatial hydrometeorological model integrates both GIS-derived HRUs and a series of physical subroutines to estimate hydrometeorological variables at high spatial resolution on a daily time step over mountain watersheds. The GENESYS model links daily meteorological data from a low elevation base station to the defined physiographic characteristics of each HRU to extrapolate daily hydrometeorological variables over the watershed. The GENESYS model has been used in different studies to simulate the impacts of climate change on hydrology of mountainous watersheds (Lapp et al., 2005; MacDonald et al., 2009; Larson et al., 2011; MacDonald et al., 2011; MacDonald et al., 2012; MacDonald et al., 2013).

As mentioned in Section 3.2.2, there are no dams or reservoirs in the Olalla watershed (BC Government, 2018) and domestic and irrigation water consumers use water directly from the creeks or wells close to them inside the Olalla watershed (BC Government, 2018). Also, the irrigation season in the region extends through spring and summer seasons (Regional District of Okanagan-Similkameen, 2011b). Furthermore, spring and summer seasons contribute to around 80% of total annual evapotranspiration over the watershed. For these reasons, the GENESYS model was applied to assess current and future changes

in spring and summer water supply and spring and summer water demand for the vegetation cover in the Olalla watershed. To determine the available and future water supply and demand using a number of GCMs, spring and summer water volume at the outlet of watershed and spring and summer vegetation evapotranspiration (ET_c) are used as the main predictors.

Monthly air temperature lapse rates, for each HRU are applied to daily air temperature values at the base station to predict these daily values over the watershed based on the elevation difference from the base station. Then using a ratio of slope to flat solar radiation, maximum air temperature is adjusted for differences between slopes and consequently different radiant energy received (Hungerford et al., 1989).

Daily solar radiation ($W \cdot m^{-2}$) for each HRU are generated using the corresponding monthly solar radiation ($W \cdot m^{-2}$) for that HRU and monthly and daily radiation ($W \cdot m^{-2}$) at the base station. The same technique was used by the model to calculate daily precipitation.

Daily relative humidity values for the entire watershed is calculated (Glassy and Running, 1994) where the dew point air temperature is assumed to be equivalent to the minimum air temperature.

Subsequently, GENESYS calculates a daily hydrological balance for each HRU when snow pack is available or removed using Equation 3.1 and Equation 3.2 respectively:

$$SWE_t = SWE_{t-1} + P_t - I_t - S_t - If_t \quad (3.1)$$

$$SM_t = SM_{t-1} + P_t + If_t - ET_{c_t} - Rech_t - Run_t \quad (3.2)$$

Where t is the time step (days); SWE is the snow water equivalent (mm); P is simulated daily rain or snow (mm) separated from the total precipitation (Kienzle, 2008); I is snow interception modelled for the coniferous forest ((Hedstrom and Pomeroy, 1998), mm) or rain interception (mm) calculated for the whole forest (von Hoyningen-Huene, 1981); S is sublimation ((Taylor, 1998), mm), If is soil infiltration (mm) calculated as a proportion of soil runoff until saturation that is controlled with FC happens, SM is soil moisture (mm) simulated using daily ET_c (mm), as one of the drivers, calculated for different vegetation types instead of applying daily reference evapotranspiration ((Valiantzas, 2006), ET_o, mm) to the soil moisture balance which is an improvement over the model. ET_c (mm) is vegetation evapotranspiration calculated by applying appropriate monthly $PTCs$ in daily ET_o to reflect seasonal and vegetation cover differences in water requirement. A ET_c generating function using different vegetation coefficients was implemented into the latest version of GENESYS. The model needs to receive monthly PTCs values for different land cover types (Table 3.2) in order to calculate daily ET_c by using daily ET_o and Equation 3.3:

$$ET_c = PTCs \times ET_o \tag{3.3}$$

When soil water content is below 50% of the FC, a proportional reduction factor is applied to the actual ET_c (MacDonald et al., 2009) using Equation 3.4 where XK is the water supply control on evapotranspiration, SM is the daily soil moisture and FC is the field capacity (mm).

$$XK = \left(^{2\,SM}/_{FC}\right)^{1.5} \tag{3.4}$$

The influence of elevated CO_2 on water availability through the direct effect of CO_2 on vegetation using increasing in stomatal resistance was not considered in the current study, as there is some doubt whether or not these effects will happen under field conditions (McKenney and Rosenberg, 1993). $Rech$ is groundwater recharge (mm) which due to the complexity of ground water recharge quantifications in mountainous watersheds, in the current version of GENESYS, is not simulated physically. It simply increases or decreases exponentially with soil moisture content (Magruder et al., 2009). Run is soil runoff (mm) calculated using the Soil Conservation Service curve number (SCS-CN) method which uses estimation curve number (CN) values (Mockus, 1972). Finally, snow melt (mm) is modelled using a temperature index melt routine developed by Quick and Pipes (1977), which applies a variable melt factor ($cm \cdot {}^{\circ}C^{-1}$) based on land cover types and time of year (DeWalle et al., 2002) and mean daily streamflow (Q, $m^3 \cdot s^{-1}$) is simulated using the Muskingum routing method.

Additionally, a sloped area under estimation factor (SAUEF) is applied to all water balance components described above in order to correct the simulated hydrological balance for the sloped areas of the watershed (Kienzle, 2011).

3.2.6. GENESYS calibration and verification

The time frame of 1961 to 1999 was selected in order to incorporate the meteorological data for driving the model and also to implement the application of climate change scenarios and also 1961 to 1990 was considered as climate normal or baseline period.

Application of the derived lapse rates from normal (1960-1990) monthly air temperature grids (Wang et al., 2012; Wang et al., 2016) for minimum air temperature resulted in overestimations in daily minimum air temperature. Therefore, the minimum air temperature lapse rates were calibrated and adjusted to observed monthly average minimum air temperature values at the Apex Mountain Lodge climate station in order to minimize the differences between measured and modelled monthly average air temperature data at this climate station and increase the performance of GENESYS to model air temperature. The adjusted monthly minimum air temperature and the derived maximum air temperature lapse rates from the normal grids (Wang et al., 2012; Wang et al., 2016) then were applied to daily minimum and maximum air temperature values at the base station to predict daily minimum and maximum air temperatures over the watershed based on the elevation difference from the base station.

The monthly maximum and minimum air temperature lapse rates used in this study are presented in Table 3.3.

Table 3.3: Monthly maximum and minimum air temperature lapse rates ($^{\circ}C \cdot km^{-1}$).

Variables	Jan	Feb	Mar	Apr	May	Jun	Jul	Aug	Sep	Oct	Nov	Dec
T_{max}	1.9	3.9	6.3	7.6	7.7	7.9	7.8	7.6	7.0	5.9	4.0	2.0
T_{min}	4.1	6.4	4.9	4.1	9.2	9.0	6.7	6.0	6.4	4.6	4.7	5.0

Daily air temperature and snow water equivalent (SWE) simulations were tested for the HRU representing the Apex Mountain Lodge Environment Canada climate station against the available measured data. The linear regression between observed and simulated, and root mean square error ($RMSE$) of the simulated values, were determined (Figure 3.6).

The GENESYS model was calibrated and verified using CN values, as it has been found using sensitivity tests that the CN values have considerable effects on streamflow

simulations in the model. The time period of available streamflow data (1972-1999) was separated into two periods of calibration (1972-1985) and verification (1986-1999). CN value is a function of soil type, land cover surface, and antecedent moisture conditions (AMC) (USDA, 1986). It was assumed that soil type and land cover do not change with time but CN values are different between three AMCs: dry, moderate moist and, wet soil moisture conditions (SCS, 1985).

The Percent of Normal Precipitation (PNP) index at the base station was used as a flag to identify dry, moderate and wet years. The PNP was calculated by dividing actual annual precipitation by normal annual precipitation and multiplying by 100. Our climate normal period was 1961-1990. The entire study period (1961-2100) was classified using the calculated PNP values so that a year is considered to be dry if the PNP is less than 75, moderately moist if the PNP is between 75 and 125 and, wet if the PNP is higher than 125.

The USDA (1986) standard CN values are represented for various soil and land cover types in moderately moist soil conditions, and need to be decreased for drier or increased for wetter conditions (USDA, 1986). CN values were provided for different surfaces in well- to rapidly-drained soil types, including the forested area (45%), alpine and sub-alpine (85 %), barren surface (77%) and for a combination of rangeland, cropland, open water, cutblocks, and built-up areas (70%) (USDA, 1986).

Simulated total monthly water volume was calibrated for the period of 1972-1985 using CN values by iteratively adjusting the CN values to minimize the model errors in the water volume simulation. CN values were increased by 15% for wetter years in the forested area of the watershed which contributes to nearly 76% of the total watershed area. However,

CN values during wetter years were held unchanged for other land covers in the watershed. Also, CN values related to the drier years were decreased by 10% for the forested area and 35% for all the other land cover types in the watershed. The simulated total monthly water volume then was verified for the period of 1986-1999 using the calibrated CN values for dry, moderated and wet years. The calibrated CN values were applied to the entire study period (1961-2100).

The linear regression between observed and simulated values of total monthly water volume, Nash–Sutcliffe (NS) model efficiency coefficient (Nash and Sutcliffe, 1970), mean bias error (MBE) which is a measure of the systematic error of a model and evaluates the tendency of a model to under- or overestimate the measured values (Willmott and Matsuura, 2005), and mean absolute Bias error ($MABE$) which is a measure of the goodness of the fit for a model and a natural measure of average error and a good test for inter-comparisons of the average model performance error (Willmott and Matsuura, 2005), were applied to assess the predictive capability of the calibrated model to simulate monthly water volume. However, it was understood that the lack of observed data in the mountainous study watershed could limit the model calibration and verification.

3.2.7. Future climate change scenarios

Future prediction of air temperature and precipitation for the base station from ensembles of 15 GCMs of the CMIP5 were obtained from ClimateWNA where locally downscaled scale-free future monthly climate data are available for the entire province of British Columbia (Wang et al., 2012; Wang et al., 2016). ClimateWNA used change factor or delta change method to overlay a scale-free baseline dataset with historical anomaly

datasets at 50-km resolution along with GCMs projections at 100 to 300 km resolution in order to create scale-free point future datasets. The resulting data are not gridded but the user is able to make an estimate for each location.

For each 15 GCMs there are two greenhouse gas emission scenarios (RCP 4.5 and RCP 8.5) for three different future periods including, 2020's (2011-2040), 2050's (2041-2070) and 2080's (2071-2100) in the form of monthly variables. Ensembles among the 15 GCMs for the two emission scenarios and three time periods were obtained with data on future monthly maximum and minimum air temperature and precipitation for each scenario.

To downscale the GCMs derived data, the CF method (Diaz-Nieto and Wilby, 2005) was used. This method was used in this study to apply the future changes relative to the 1961-1990 period in order to adjust deriving data set to the GENESYS model based on the observed daily climate data at the base station (MacDonald et al., 2011; MacDonald et al., 2012; MacDonald et al., 2013).

Future monthly air temperature and precipitation changes relative to the baseline (1961-1990) were calculated for two scenarios and three time periods (Figure 3.5). Monthly maximum and minimum air temperature changes were added to each day in the historical record (Diaz-Nieto and Wilby, 2005). To apply changes in precipitation for each scenario to the observed values, the monthly precipitation changes relative to the baseline (future monthly precipitation / base monthly precipitation) were multiplied by the daily precipitation values at the base station (Diaz-Nieto and Wilby, 2005). Six groups of 30-year datasets with applied changes in air temperature and precipitation were used as inputs to GENESYS to estimate hydrometeorological variables for the range of climate changes

scenarios in the Olalla watershed. However, the limitation of the FC method is any pattern of variability that may exist in the watershed scale will be assumed to remain unchanged in the future. However, the variability in local climate conditions at the study base station is considered (Diaz-Nieto and Wilby, 2005).

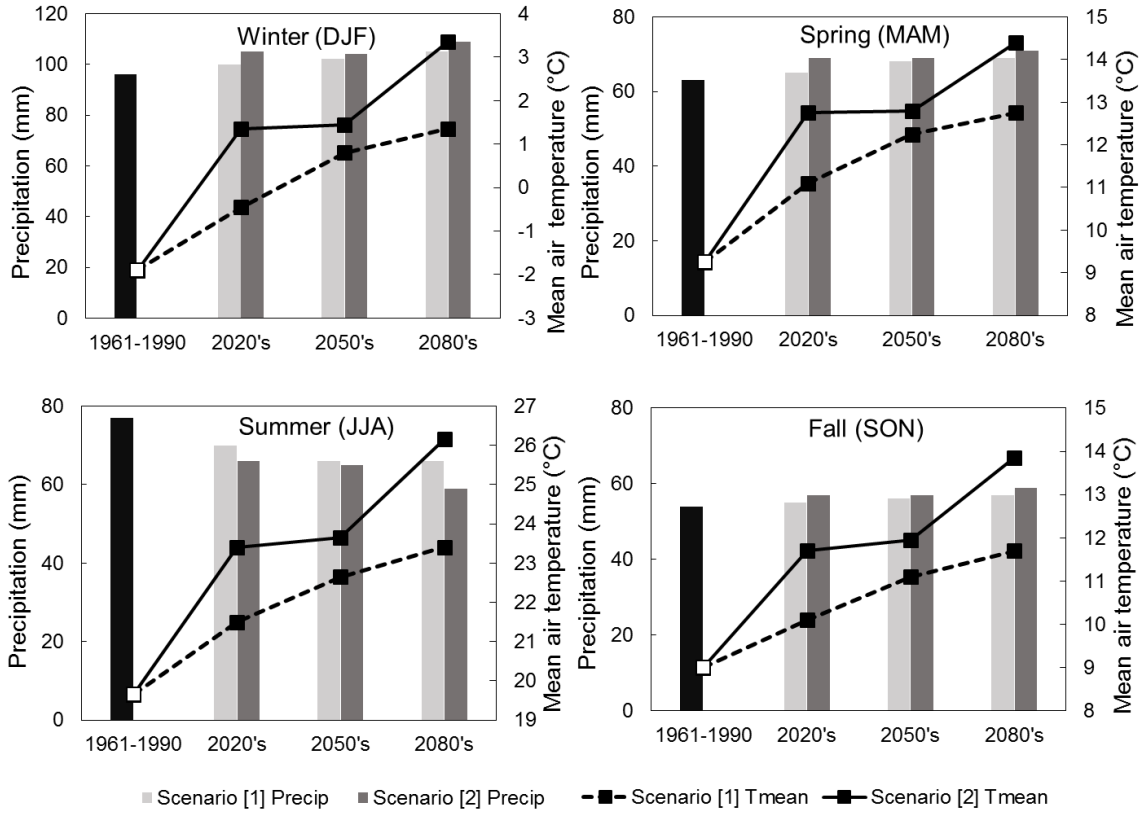

Figure 3.5: Future seasonal changes in actual mean temperature (average of maximum and minimum, ˚C) and precipitation (mm) relative to the 1961-1990 historical period for the Keremeos 2 station. DJF = December–February, MAM = March–May, JJA = June–August, SON = September–November.

Predicted air temperature increases were estimated for both greenhouse gas emission scenarios (RCP 4.5 and RCP 8.5) in each three different future periods including 2020's, 2050's and 2080's in all four seasons (Figure 3.5). However, future precipitation is forecast to increase in all seasons except summer where there is a decrease in precipitation (Figure 3.5).

3.3. Results and discussion

3.3.1 GENESYS calibration and verification

Simulated daily maximum air temperature, using the derived lapse rates from normal (1960-1990) monthly air temperature grids (Wang et al., 2012; Wang et al., 2016), simulated daily minimum air temperature using the adjusted lapse rates, and simulated total monthly SWE compared very well with the historical measurements at the Apex Mountain Lodge climate station for the available period of recorded data (Figure 3.6 and Table 3.4). However, it should be taken into account that the Apex Mountain Lodge station is located at high altitude at a considerable distance from the base station (Figure 3.1). As mentioned in MacDonald et al. (2012), accuracy of the GENESYS model predictions for air temperature and snow may decrease with increasing elevation, as a function of increasing distance from the base station and also increasing variability of the air temperature and snow in mountain areas.

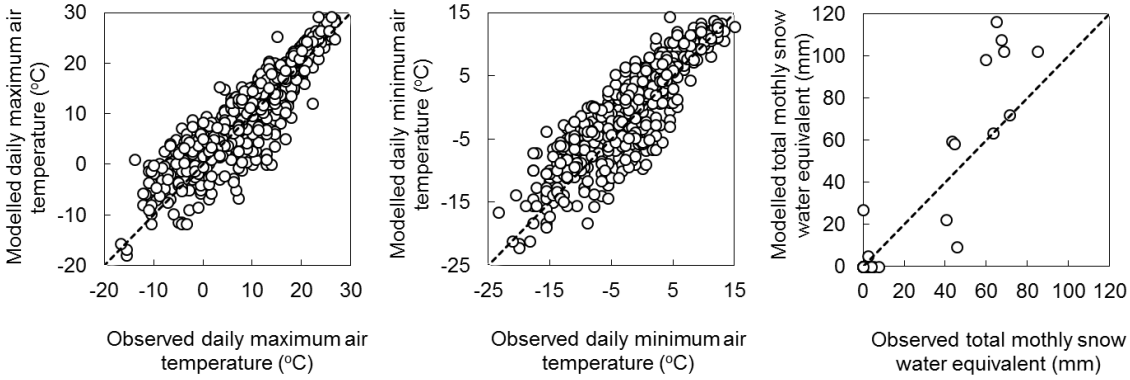

Figure 3.6: Observed vs. modeled daily maximum and minimum air temperature (˚C) and total monthly snow water equivalent (SWE) (mm) at the Apex Mountain Lodge climate station (the line represents the 1:1 line).

Table 3.4: Statistical comparison of the observed (x) vs. modeled (y) daily maximum and minimum air temperature (˚C) and total monthly snow water equivalent (SWE) (mm) at the Apex Mountain Lodge climate station.

$y = a + bx$	$Std.\,Error_a$	t_a	p	$Std.\,Error_b$
Daily maximum air temperature (˚C)				
$\mathbf{y = 2.577 + 0.859x}$	0.226	11.38	<0.001	0.018
Daily minimum air temperature (˚C)				
$\mathbf{y = 1.669 + 0.896x}$	0.135	12.33	<0.001	0.018
Total monthly SWE (mm)				
$\mathbf{y = -1.118 + 1.283x}$	4.293	-0.26	<0.001	0.110
t_b	p	r^2	RMSE	n
Daily maximum air temperature (˚C)				
48.36	<0.001	0.79	4.4 °C	605
Daily minimum air temperature (˚C)				
49.47	<0.001	0.78	3.9 °C	683
Total monthly SWE (mm)				
11.66	<0.001	0.85	19 mm	27

Simulated total monthly spring and summer (March to August) water volume were compared with the corresponding measured values for the calibration and verification periods at the Keremeos creek below Willis intake stream gauge location (08NL045) (Figure 3.7 and Table 3.5).

The Nash–Sutcliffe efficiency of 0.88 for the verification period showed the calibrated model was able to predict total monthly spring and summer (March to August) water volume very well (Figure 3.7 and Table 3.5). MBE test showed the model overestimated the measured values by 1.3%. Also, $MABE$ test showed the model had 24.0% average model performance error (Figure 3.7 and Table 3.5).

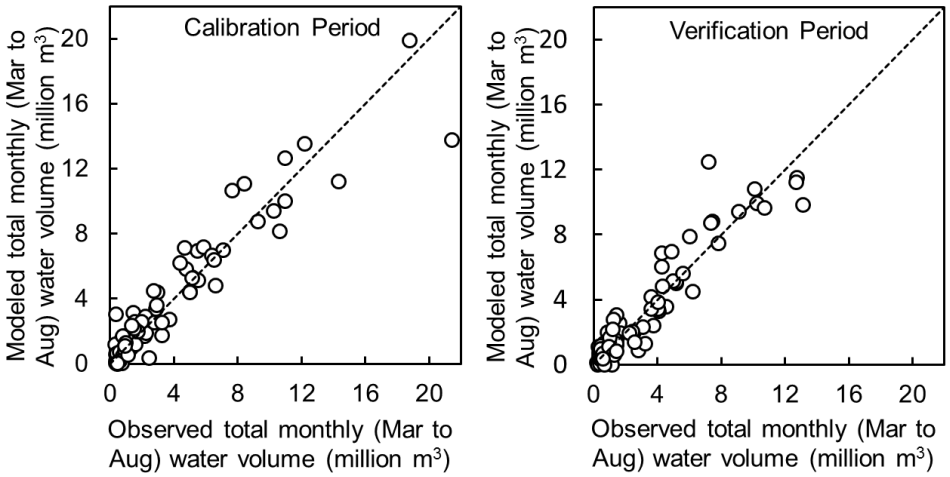

Figure 3.7: Observed vs. modelled total monthly spring and summer (March to August) water volume (million m^3) at the Olalla watershed, BC for the calibration (1972-1985, left) and verification (1986-1999, right) periods (the line represents the 1:1 line).

Table 3.5: Statistical comparison of the observed (x) vs. modelled (y) total monthly spring and summer (March to August) water volume (million m^3) at the Olalla watershed, BC for the calibration (1972-1985) and verification (1986-1999) periods.

$y = a + bx$	Std. $Error_a$	t_a	p	Std. $Error_b$	t_b
Calibration (1972-1985) period					
$\mathbf{y = 0.44 + 0.89x}$	0.18	2.40	<0.001	0.03	26.09
Verification (1986-1999) period					
$\mathbf{y = 0.18 + 0.95x}$	0.16	1.10	<0.001	0.04	25.42
p	**r^2**	**n**	**MBE**	**MABE**	**NS**
Calibration (1972-1985) period					
<0.001	0.89	84	2.2%	24.8%	0.89
Verification (1986-1999) period					
<0.001	0.89	84	1.3%	24.0%	0.88

3.3.2. Future water supply

In order to compare future changes in spring and summer water supply of the Olalla watershed, the 30-yr average spring and summer water volume for two emission scenarios and three future time periods, 2020's, 2050's, and 2080's were compared with the 30-yr average spring and summer water volume for the 1961-1990 period. Timing of snowmelt was also analysed for different scenarios relative to the 1961-1990 period.

Snowmelt started in April and achieved a peak in June and then decreased through July and August for the 1961-1990 period (Figures 3.3 and 3.8). However, the onset of snowmelt is likely to shift earlier in March with the primary spring water volume between March and June with a peak in May for Scenario 1 and time period of 2020's (Figure 3.8). This pattern is the same for all other future scenarios except Scenario 2 in the 2080's, in which the timing of snowmelt may start two months earlier and extend through February and May with a peak in April (Figure 3.8). An earlier timing of snowmelt in all scenarios is likely a function of air temperature increases over the watershed (Figure 3.5 and 3.8). According to the results, the peak water volume may decrease for different scenarios and time periods relative to the average historical value (Figure 3.8). The reduction in peak water volume is a function of likely decreases in the ratio of snow to total monthly precipitation due to air temperature increases in all scenarios and time periods (Knowles et al., 2006). If more of the precipitation occurs as rain than snow, the available water storage in the form of snow decreases and results lower snowmelt runoff (MacDonald et al., 2011).

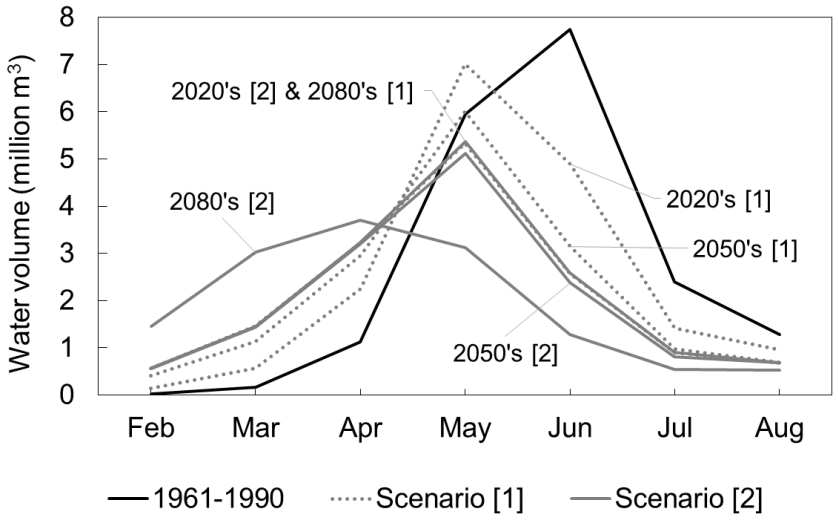

Figure 3.8: Snowmelt period scenarios relative to the base scenario for the Olalla watershed.

Snowmelt timing shifts to the beginning of the spring (March) for all the future scenarios except February for Scenario 2 in the 2080's (Figure 3.8), which may result in higher flows in the early spring and lower in summer relative to the 1961-1990 period (Figure 3.9). These changes with a combination of possible increases in future spring precipitation and decreases in summer precipitation (Figure 3.5), may increase spring water volume and decrease summer water volume in the Olalla watershed (Figure 3.9). However, the possible declines in the peak water volume in different climate change scenarios may not offset the increases in total spring water volume because the shifts in peak occur from June in summer to May (April in Scenario 2 in the 2080's) in spring (Figure 3.8).

The results showed, relative to the 1961-1990 period, total early spring water supply may increase by 36%, 39%, and 38% in Scenario 1 and by 39%, 35%, and 36% in Scenario 2 for the periods 2020's, 2050's and 2080's, respectively (Figure 3.9). Although, total spring water supply increased substantially in all scenarios relative to the 1961-1990 period, these increases were not notably different among scenarios and time periods (Figure 3.9). According to the results presented in Figure 3.9, total summer water volume may decrease for all future scenarios relative to the historical period. Relative to the 1961-1990 period, total summer water supply may be reduced by 36%, 58%, and 64% in Scenario 1 and by 64%, 66%, and 79% in Scenario 2 for the periods of 2020's, 2050's and 2080's, respectively (Figure 3.9). In both scenarios 1 and 2, the reductions in summer water supply increased substantially from 2020's to 2080's and the highest reductions between all scenarios and time periods was for Scenario 2 in the 2080's (Figure 3.9). Furthermore, negative changes in summer water supply were higher than positive changes in spring water supply in the Olalla watershed and as a result total spring and summer (March to July)

water supply decreased for eight percent, 20%, and 24% in Scenario 1 and for 24%, 27%, and 35% in Scenario 2 for the periods of 2020's, 2050's and 2080's, respectively relative to the 1961-1990 period (Figure 3.9). This has important implications for irrigation water supply and management.

Nearly all agricultural lands in the Rural Keremeos area (Area G in the RDOS regional district) are under irrigation, about 78% of the irrigated lands are hay and pasture, 17% are fruits (cherries, apples, peaches, and grapes), 3% are field crops and 2% are vegetables (Statistics Canada, 2006). Longer growing season and a warmer climate may favour agriculture in the region but this may also increase irrigation water demand (Cohen et al., 2006) during critical periods. Also, suitable climate conditions for fruit growing may expand to higher elevations (Zebarth et al., 1997) and this would increase fruit production in the watershed. However, climate change may increase spring water supply in the watershed, and if so this may not be very beneficial practically because a water supply increase during the wet season, even possibly resulting in excess water, may not be available during summer as there are no reservoirs in the watershed to store the water. Likely decreases in future summer water volume would stress summer water supply in the dry season. The simulated decline in summer water supply (Figure 3.9) may increase competition between agriculture and other sectors, such as domestic needs, in the dry season. Furthermore, the time of less water during the summer season overlaps with the highest irrigation demand (around June and July) and threats crop productivity in the watershed where most of the crops are under irrigation (Cohen et al., 2006). This may be more pronounced in our study watershed because its irrigation water is supplied by licences that use water directly from the creek or wells very close to the creek (BC Ministry of

Environment Lands and Parks, 1981; Regional District of Okanagan-Similkameen, 2011b). The future situation may need transitioning to more efficient irrigation systems such as drip irrigation, or, this may also result in management decisions to grow other types of crops suited to the more efficient irrigation systems.

Although the frequency of droughts has not yet been attributed to climate change caused by human activities, the effects of climate change on hydrology may result in greater number and intensity of droughts (Barnett et al., 2005). Stewart et al., (2004) showed a one-month advance in snowmelt makes the summer drought periods longer and will have serious effects on the water supply, wildfire management and ecosystem in western North America. Lower summer water supply in the watershed (Figure 3.9) may accelerate the effects of possible future droughts in the watershed. Decreases in summer water supply (Figure 3.9) may also influence summer groundwater availability in the watershed as groundwater system is closely connected to the surface water in the region (Cohen et al., 2000).

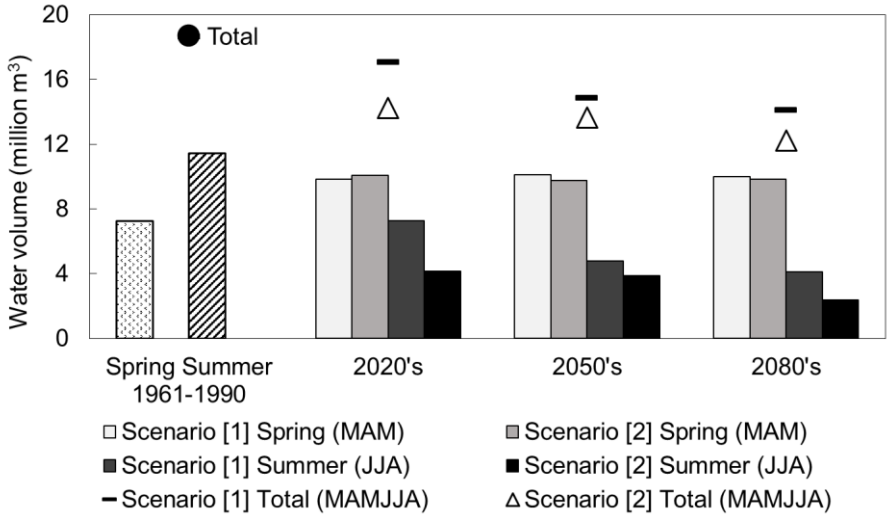

Figure 3.9: Spring and summer water supply scenarios relative to the 1961-1990 for the Olalla watershed. MAM = March–May, JJA = June–August, MAMJJA = March–August.

3.3.3. Future vegetation water demand

The results demonstrate future climate change is likely to increase spring ET_c over the watershed, although not equally across HRUs (Figure 3.10). Average spring vegetation water demand over the watershed is likely to increase relative to the historical period by 20%, 32% and, 37% in Scenario 1 and 37%, 36% and, 47% in Scenario 2 for 2020's, 2050's and 2080's, respectively (Figure 3.12). For the summer season, Scenarios 1 and 2 showed a likely decrease in ET_c over the watershed (Figure 3.11). Summer vegetation water demand may decrease in contrast to the 1961-1990 period by 10%, 18% and, 20% in Scenario 1 and 20%, 21% and, 29% in Scenario 2 for 2020's, 2050's and 2080's, respectively (Figure 3.12). However, similar to the spring season these changes are not uniform over all vegetation covers in the watershed (Figure 3.11). The increases in ET_c during spring were more than reductions in ET_c during summer season (Figure 3.12). However, the total spring and summer (March to July) evapotranspiration may not change significantly in future relative to the historical period (Figure 3.12).

The actual inter-annual evapotranspiration is controlled and limited by both the availability of surface energy and soil moisture (Boé and Terray, 2008). Warmer air temperature (Figure 3.5) and correspondingly higher surface energy during spring would increase actual evapotranspiration. This is because, ET_c is controlled by surface energy in winter, fall, and spring in hydro-meteorological models like GENESYS that include a limiting impact of soil moisture on evapotranspiration (Boé and Terray, 2008). However, the models realized evapotranspiration is mostly controlled by soil moisture deficits during summer (Boé and Terray, 2008). Warmer air temperature and lower precipitation during

summer (Figure 3.5) and resultant lower soil moisture decreases evapotranspiration in this season.

Evapotranspiration in drier climates is a major component of water balance, and changes in evapotranspiration as a result of climate change may affect runoff (Merritt et al., 2006). The likely increases in spring evapotranspiration (Figure 3.12) may offset the likely increases in spring water supply (Figure 3.9). However, the likely decreases in summer evapotranspiration (Figure 3.12) may not be able to offset the likely decreases in summer water supply (Figure 3.9). Since the highest irrigation demand is during summer, future dry condition during summer along with population growth, warmer air temperature, and a longer growing season may threaten summer water availability in the watershed.

The uninform pattern of changes in evapotranspiration across the Olalla watershed in spring and summer (Figures 3.10 and 3.11) may also result in changes in vegetation cover type over the watershed. Also, in all scenarios, the upper 10% of the modeled changes occurred in elevations above 1400 m and 1200 m in spring and summer, respectively (Figures 3.10 and 3.11), which reflects the greater effect of climate change in higher elevations. In higher elevations, air temperature will rise above the threshold that precipitation can occur as snow instead of rain, and these thresholds were not met in the past in these elevations (MacDonald et al., 2012). Furthermore, higher spring evapotranspiration particularly in higher altitudes, may favour orchard production in these elevations (Zebarth et al., 1997).

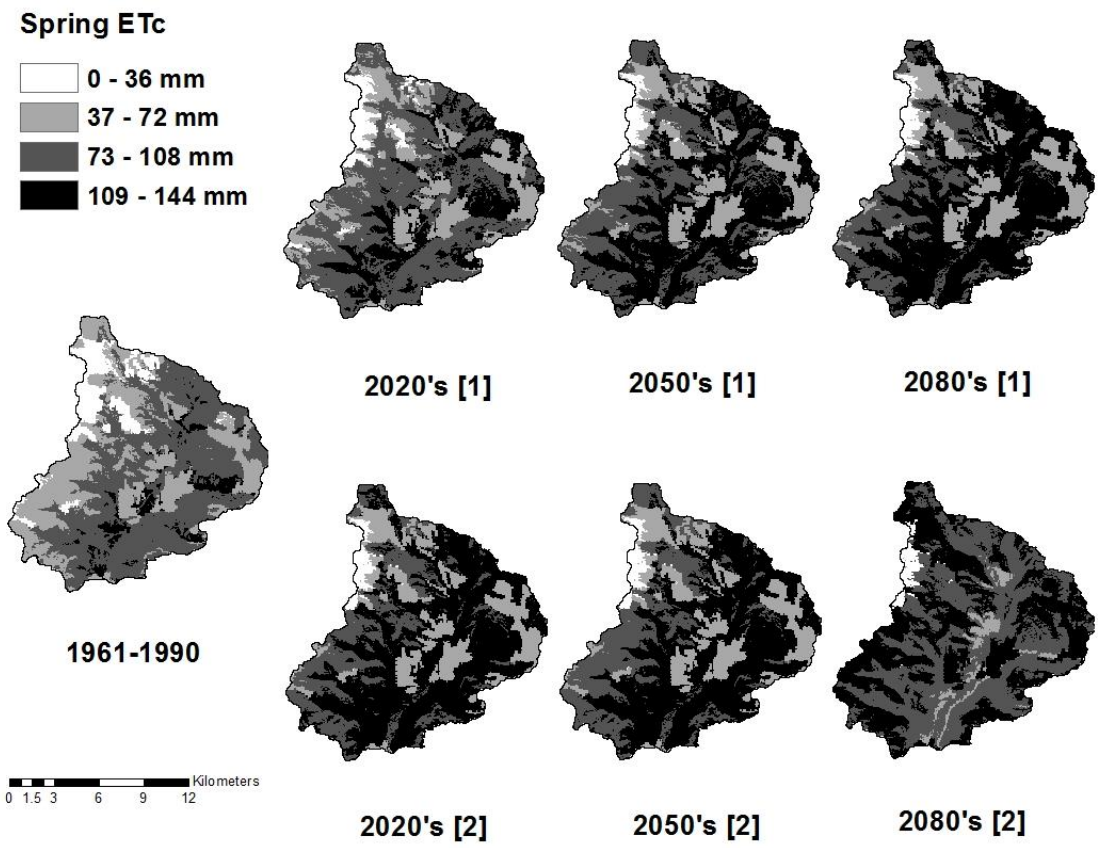

Figure 3.10: Spatial change in 30-year mean spring vegetation evapotranspiration (mm) at the Olalla watershed for the two emission scenarios for 2020's, 2050's, and 2080's periods relative to the 1961-1990 period. ET_C is vegetation evapotranspiration.

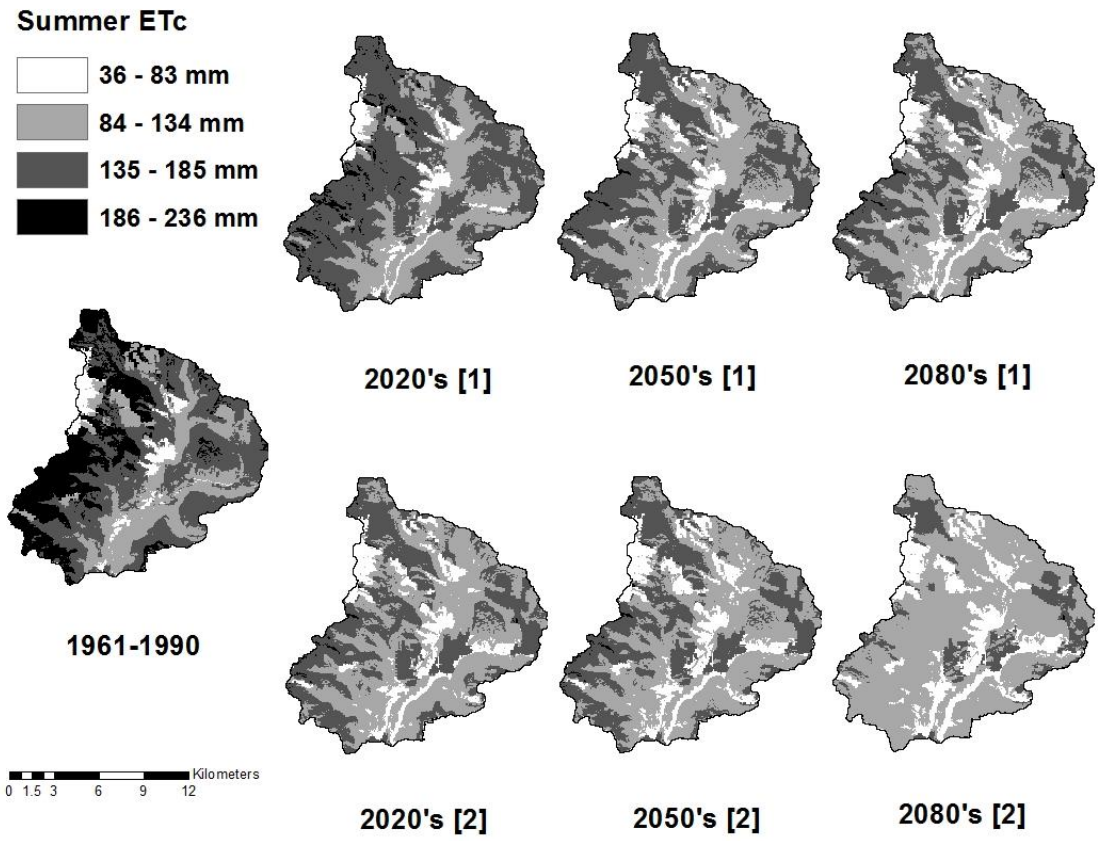

Figure 3.11: Spatial change in 30-year mean summer vegetation evapotranspiration (mm) at the Olalla watershed for the two emission scenarios for 2020's, 2050's, and 2080's periods relative to the 1961-1990 period. ET_C is vegetation evapotranspiration.

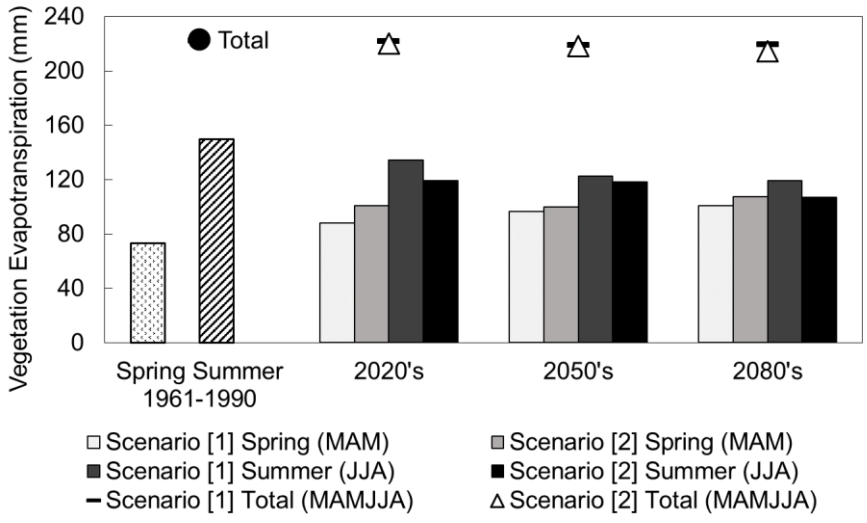

Figure 3.12: Spring and summer water demand scenarios over the Olalla watershed relative to the historical period. MAM = March–May, JJA = June–August, MAMJJA = March–August.

3.4. Conclusions

Current and future changes in spring and summer water supply and spring and summer vegetative water demand were investigated in Chapter 3 using the GENESYS spatial hydrometeorological model in the Olalla watershed, RDOS, BC, for two greenhouse gas emission scenarios (RCP 4.5 and RCP 8.5) and three different future periods relative to the 1961-1990 period.

The results of Chapter 3 showed that timing of snowmelt may occur one month earlier in all scenarios except Scenario 2 in the 2080's, which may be two months earlier relative to the 1961-1990 period as a result of increases in air temperature. There may be increases in future total spring water supply and decreases in summer water supply relative to the 1961-1990 period. These changes are likely due to increases in spring precipitation and decreases in summer precipitation along with the shifts in timing of snowmelt towards earlier in the spring. Furthermore, negative changes in summer water supply are higher than positive changes in spring water supply in the Olalla watershed. Average spring vegetation water demand may increase but summer vegetation water demand decrease for all scenarios relative to the historical period. These changes in evapotranspiration may be due to increases in surface energy during spring and decreases in soil moisture during summer, which as main drivers control evapotranspiration in these seasons. Also, changes in evapotranspiration may be higher in spring than summer and positive or negative changes more pronounced for the area located in elevation above 1400 m in spring and 1200 m in summer.

Increases in spring water supply may offset the increases in spring vegetation water demand; however, decreases in summer water supply cannot offset the decreases in spring vegetation water demand in the Olalla watershed. These changes are expected to put stress on water resources, agriculture, recreation activities, management, vegetation, wildlife, human settlements, and economic activities, along with non-climate change anthropogenic forces in the watershed. Hydro-climatology estimates generated by the study presented in Chapter 3 can help different sectors provide possible mitigation strategies in order to overcome the negative impacts of climate change in the Olalla watershed.

Chapter 4 : The effect of climate change on farm-level greenhouse gas (GHG) emissions in an Okanagan-Similkameen sub-watershed, British Columbia, Canada

4.1. Introduction

Agriculture is a considerable source of GHG emissions as a result of higher rates of production associated with industrialized farming practices (Kröbel et al., 2016). However, the response of agricultural GHG emissions to changes in atmospheric composition and subsequent climate change, and changes in agricultural rates and processes, are still unclear (IPCC, 2014) and require more study to provide local sectors with most relevant information for the development of mitigation practices (Stocker, 2014). Furthermore, there are disagreements between different studies on the positive or negative effects of warmer air temperature on soil carbon stocks (Davidson and Janssens, 2006). Warmer air temperature may accelerate decomposition of soil carbon (Gregorich et al., 2017) and transfer more carbon to the atmosphere (positive feedback); however, more plant-derived soil carbon capture may exceed increases in decomposition (negative feedback) (Davidson and Janssens, 2006).

There continues to be demand for cost-effective ways to mitigate GHG emissions from agriculture (Burney et al., 2010). Soil carbon stocks have been recognized as one of the most profitable strategies to offset net farm-level GHG emissions (Antle et al., 2002; Kröbel et al., 2016), though the offset will subsequently decline because carbon storage diminishes over time as the soil reaches a new carbon content equilibrium. Soil carbon stocks react to management changes where the balance between carbon inputs and outputs is changed, for instance by switching from annual to perennial cropping (Kröbel et al.,

2016). In order to mitigate the possible negative effect of climate change on farm-level GHG emissions, climate-induced changes in hydrometeorology can be implemented in GHG emissions models along with different agricultural management techniques to increase soil carbon stocks.

Chapter 4 applies a coupled modelling approach to investigate current and future hydrometeorological conditions using the GENESYS spatial hydrometeorological model described in Chapter 3 (MacDonald et al., 2009).

The changes in hydrometeorological conditions are then applied in the Holos GHG emissions estimation model (Little et al., 2008). The Holos model was designed by scientists at Agriculture and Agri-Food Canada to estimate GHG emissions for Canadian farms, including both animal management and cropping systems (Little et al., 2008). The main purposes of the model are estimating GHG emissions and informing management strategies for reducing GHG emissions. The model has been applied to estimate farm GHG emissions from beef and dairy production systems and also assess the impacts of management practices changes on farm GHG emissions (Janzen et al., 2006; Little et al., 2008; Stewart et al., 2009; Beauchemin et al., 2010; Beauchemin et al., 2011; Bonesmo et al., 2012; Kröbel et al., 2012; Mc Geough et al., 2012; Hünerberg et al., 2014; Chai et al., 2016; Kröbel et al., 2016; Legesse et al., 2016; Alemu et al., 2017a; Alemu et al., 2017b; Guyader et al., 2017).

This coupled modelling approach is used to estimate climate-induced changes in GHG emissions (CO_2, CH_4 and, N_2O) and soil carbon stocks for both crop and animal production processes. Chapter 4 considered two RCP scenarios (RCP 4.5 and RCP 8.5) for

three different future periods, including 2020's (2011-2040), 2050's (2041-2070) and 2080's (2071-2100) relative to a base period (1961-1990) using the ensembles of 15 GCMs of the CMIP5 (Moss et al., 2010; Wang et al., 2012; Wang et al., 2016). These future conditions were used for a simulated farm in the Olalla watershed described in Chapter 3. The effect of climate change on farm-level GHG emissions in the Okanagan-Similkameen region has never been assessed before.

4.2. Methods

4.2.1. Study area

The Olalla watershed, whose physical and climate characteristics were described in Chapter 3, has diverse land cover types, with about 76% of the watershed covered by coniferous forests, mostly IDF and the agricultural area in the watershed consists of un-irrigated rangeland (7.3% of the watershed area) and irrigated cropland (1.8% of the watershed area) ((Hectares BC, 2015), Figure 4.1). Elevation in the watershed ranges from 476 to 2235 m a.s.l, where the agricultural area is located below 900 m a.s.l elevation and the rangelands are located between 500 and 2100 m a.s.l elevation.

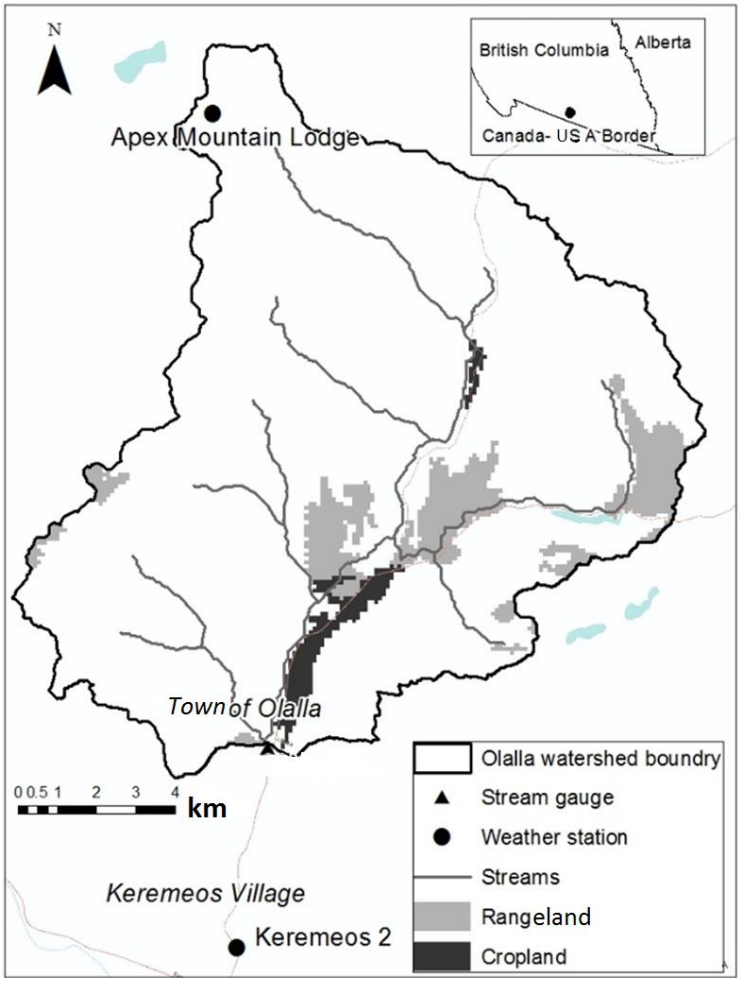

Figure 4.1: Simulated farm (cropland and rangeland area) in watershed.

The town of Olalla in the valley of the watershed has been growing in size and population over recent decades (Regional District of Okanagan-Similkameen, 2017). Cattle ranching is the dominant agricultural activity in this area, considering that land is used for the production of alfalfa, alfalfa mixtures, and hay and also fruit production is the other important agricultural activity (Statistics Canada, 2006). Nearly all croplands in the watershed is under irrigation and about 78% of the irrigated land is used to grow perennial hay and pasture, 17% to grow fruits, and 3% to grow annual field crops (Statistics Canada, 2006). There is no detailed information on vegetable grown in the area; however, it was

assumed that the remaining 2% of the irrigated area is for vegetable production ((Statistics Canada, 2006)).

The irrigation season in the watershed is from April to the end of September for most irrigation users (Regional District of Okanagan-Similkameen, 2011b). There are no dams or reservoirs, groundwater points of diversion or artesian wells in the watershed (BC Government, 2018) as mentioned in Section 3.2.2. However, there are active domestic water licences that use water directly from the Keremeos Creek and its tributaries, and irrigation licences that use wells close to the creeks inside the Olalla watershed (BC Government, 2018).

A research conducted in the region in order to find the preferences of farmers among three different policies options in a time of water shortage including water trading in a water market, mandatory reduction in water supply, and priority reallocation of water among farmers based on the type of crop grown or proportional distribution (Conrad et al., 2017). The result showed the farmers growing forage, ranch, orchards, and mixed use in the region would mostly prefer a moderate level (e.g., 15%) of reduction, not an extensive level, during a water shortage period among other policies options (Conrad et al., 2017).

4.2.1.1. Simulated farm

A simulated farm was used to represent a typical farm in the Olalla watershed in order to estimate the whole-farm GHG emissions for current and future scenarios (Figure 4.1). The simulated farm included a cow-calf operation and a feedlot, as well as land for grazing (range), perennial mixed-hay (pasture), annual barley silage, and barley grain for cattle feed and bedding supplements ((Beauchemin et al., 2010; Alemu et al., 2017b), Tables 4.2 to

4.4). Further, the farm was assumed to grow vegetables as a minor form of production, including beans, cabbages, onions, peas, peppers, potatoes, sugar beets, tomatoes, and watermelons ((Dorenboss and Kassam, 1979; Janzen et al., 2003; Statistics Canada, 2006), Tables 4.1 to 4.3). The agricultural land also includes small orchards of 18-year-old apple trees (Fiji hybrid), at the peak of carbon sequestration capability ((Wu et al., 2012), Tables 4.1 to 4.4). The growing season in the simulated farm was from April to the end of September (Regional District of Okanagan-Similkameen, 2011b).

Table 4.1: The information related to the simulated farm in the Olalla watershed.

Ecodistrict	**Ecozone**		**Soil texture**	**Soil type**	**Global warming potentials**		
					CO_2	**CH_4**	**N_2O**
1010	Montane Cordillera		Coarse	Brown Chernozem	1	28	265
Crops							
	Annual		**Perennial**	**Fruits**	**Native grasslands**		
Barley silage	**Barley grain**	**Vegetables**					
Area (ha)							
3	8	7	282	62[a]	1441		
Yield ($kg \cdot ha^{-1}$) [b]							
9530	5975	12000	6724	41696			

[a] In all crops, the area of crop is equal to the total irrigated area, but for apple trees, the total irrigated (drip irrigation) area is about 37 ha. The area covered by an 18-yr tree is 3.75 m^2.
[b] Yield data were obtained from Alemu et al. (2017b) and Wu et al. (2012).

Table 4.2: Climate, soil and water requirement, yield and total irrigated area for the crops in the simulated farm in the Olalla watershed[a].

Crop	Temperature requirement, optimum and range (°C)	Soil requirement	Fertilizer requirements (kg·ha^{-1}·growing period^{-1}) [b]		Water requirement (mm·growing season^{-1})	Sensitivity to water supply (k_{ET}) [c]
			N	P		
Barley	15-23, 5-30	Wide range of soils from deep sands and shallow soils to loams to heavy clays	45	50	450-650	Medium to high (1.15)
Vegetables [d]	15-30 , 10-35	Deep, medium textured, well drained	170	110	300-900	Medium to high (1.15)
Mixed hay	24-26, 10-30	Deep, medium textured, well drained	40	65	800-1600	Low to medium high (1.10)
Fruits (apple trees)	15-25, 10-35	Deep, medium textured	149	149	900-1010	High (1.20)

[a] Data were obtained from Dorenboss and Kassam, (1979)
[b] Highest recommended rates of N and P fertilizers are used, because the soil in the Olalla watershed is not very fertile.
[c] K_{ET} of the total growing period: low ($0.7<K_{ET}<0.8$), medium-low ($0.85<K_{ET}<0.95$), medium-high ($1.05<K_{ET}<1.15$), high ($K_{ET}>1.2$).
[d] The values for the vegetables are for a set of crops such as beans, cabbages, onions, peas, pepper, potatoes, sugar beets, tomatoes, and watermelons.

Table 4.3: Crop-specific characteristics used for the simulated farm in the Olalla watershed[a].

Crop	Moisture content (w·w^{-1})	Above ground residue N content (kg N·kg^{-1})	Below ground residue N content (kg N·kg^{-1})	Yield ratio
Barley silage	0.07	0.013	0.007	0.72
Barley grain	0.12	0.007	0.010	0.38
Vegetables	0.80	0.020	0.010	0.40
Mixed hay	0.13	0.015	0.015	0.40
Fruits (apple trees)	0.84	0.010	0.010	0.04

Crop	Above ground residue ratio	Below ground residue ratio	Fuel energy (GJ·ha^{-1})	Herbicide energy (GJ·ha^{-1})
Barley silage	0.08	0.20	1.78	0.23
Barley grain	0.47	0.15	1.78	0.23
Vegetables	0.40	0.20	1.78	0.23
Mixed hay	0.10	0.50	1.78	0.23
Fruits (apple trees)	0.67	0.30	1.78	0.23

[a] Data were obtained from Janzen et al. (2003).

Table 4.4: Fruit tree characteristics used for the simulated farm in the Olalla watershed[a].

Tree type	Fiji apple
Assumed age (yr)	18
Area covered by an 18 yr tree (m^2)	3.75
Stand length (yr)	30
Rows	315
Row length	787
Planting space (m)	2.5
Total number of trees	99162
a, b (coefficients for annual carbon accumulation)	0.9211, 1.0351

[a] Data were obtained from Wu et al. (2012).

4.2.2. Datasets used

4.2.2.1. Hydrometeorological data

The available streamflow data recorded from 1972 to 1999 at the Keremeos Creek below Willis intake (08NL045) and the air temperature (ºC) and snow water equivalent (SWE) (mm) data (1965 to 1971) from Apex Mountain Lodge station in the watershed (Figure 4.1; (Environment Canada, 2015)) were used for model calibration and validation described in Chapter 3. The station 'Keremeos 2' (435 m elevation) - within the eight kilometers from the town of Olalla with daily maximum and minimum air temperature (ºC) and precipitation (mm) data for the period of 1961 to 1999 - was selected as the base station ((Environment Canada, 2016), Figure 4.1) to run the model. Daily solar radiation (W m^{-2}) for the weather station were also calculated using daily air temperature data and the daily solar radiation estimation method described in Chapter 2 (Mirmasoudi et al., 2018).

4.2.2.2. Climate models

Future prediction of air temperature and precipitation for the base station from ensembles of 15 GCMs of the CMIP5 were obtained from ClimateWNA (Wang et al., 2012; Wang et al., 2016) . Locally downscaled scale-free future monthly climate data are

available for the entire BC province (Wang et al., 2012; Wang et al., 2016). The CF downscaling method (Diaz-Nieto and Wilby, 2005) was used to implement future monthly maximum and minimum air temperature and precipitation changes for the ensembles of the 15 GCMs for two greenhouse gas emission scenarios (RCP 4.5 and RCP 8.5) for three different future periods including, 2020's (2011-2040), 2050's (2041-2070) and 2080's (2071-2100) relative to the normal period of 1961-1990 in order to perturb deriving data set to the GENESYS model based on the measured daily climate data at the base station. Six 30-year meteorological datasets of the base station, for six climate change scenarios, with applied changes in air temperature, and precipitation were used as inputs to the GENESYS model to estimate hydrometeorological variables spatially for the Olalla watershed.

4.2.3. The GENESYS hydrometeorological model

The GENESYS spatial hydrometeorological model described in Chapter 3 was used to estimate hydrometeorological variables on a daily time step over the watershed. The watershed was divided into 201 HRUs using the method described in Chapter 3. The total agricultural area, both croplands and rangelands, included 47 different HRUs.

The GENESYS model links daily meteorological data from the base station to the defined physiographic characteristics of each HRU to extrapolate hydrometeorological variables. Daily air temperature values for each HRU were estimated using monthly air temperature lapse rates and daily air temperature values at the base station. Daily precipitation estimates for each HRU were generated using the relationship between monthly values at the HRU and monthly and daily values at the base station. Daily potential

evapotranspiration (PET, mm) for each HRU and, mean daily streamflow (Q, $m^3 \cdot s^{-1}$) at the outlet of the watershed were calculated under snow-covered and snow-free conditions.

4.2.3.1. Modelling setup and parameterization

For each HRU, the following parameters were identified: mean elevation (m), area (km^2), monthly leaf area index (LAI) (NASA LP DAAC, 2000), normal (1961-1990) mean monthly solar radiation ($W \cdot m^{-2}$) (Mirmasoudi et al., 2018), monthly maximum and minimum air temperature ($^{\circ}C \cdot km^{-1}$) and precipitation (mm) lapse rates (Wang et al., 2012; Wang et al., 2016), field capacity (FC, mm) ranging from 38 to 233 mm and monthly plant transpiration coefficients (PTCs). The estimated PTCs for different land cover types in upper North Saskatchewan River Basin (UNSRB), Alberta (Nemeth, 2010) were adjusted to the study area in order to take into account a drier climate in this watershed compared to UNSRB (BC Ministry of Agriculture Food and Fisheries, 2001). It was assumed that half of the total growing season water use (0.73 million m^3) is consumed during June and July and the other half during April, May, August and September (BC Government, 2018). It was also assumed that total annual (12 months) water use for the other licences including conservation (storage), domestic, livestock and animal, waterworks and, others was 0.50 million m^3 (BC Government, 2018). Total annual human water use (1.23 million m^3) was held constant during future simulations in order to test only the effect of changes in air temperature and precipitation on spring and summer water volume (million m^3). The total monthly human water use was subtracted from the simulated total monthly water volume.

The GENESYS model outputs including mean monthly air temperature, mean total growing season precipitation, and mean total growing season PET were estimated for the

simulated farm associated HRUs (cropland and rangeland HRUs). Also, total growing season water supply at the outlet of the Olalla watershed was calculated. These outputs from the GENESYS model were then used as inputs into Holos to estimate GHG emissions for the base and future climate scenarios at the simulated farm.

4.2.4. The Holos greenhouse gas model

Holos is a farm-level model that estimates GHG emissions from cropping system annually and from livestock on a monthly time step (Little et al., 2008). The model links farm characteristics including crops and animals, and a series of algorithms such as the Intergovernmental Panel on Climate Change (IPCC) Tier 2 methodology (IPCC, 2006) adjusted for Canadian agriculture system in order to estimate GHG emissions from a whole farm. Holos calculates average annual GHG (CO_2, CH_4, and N_2O) emissions from enteric fermentation, manure management, cropping, and energy consumption. Carbon sequestration from tree planting and land use management is also calculated in Holos and an equilibrium level for soil carbon content is estimated based on environmental and management conditions of the prior 30-year time frame (Kröbel et al., 2016).

Soil carbon was assumed to be constant and soil carbon change emissions are insignificant, unless changes in climate, crop yield, land use or management techniques occur (e.g., conventional versus reduced versus no tillage), which can be applied according to the year when adaptation occurred. When changes in soil carbon are taken into account, the equilibrium state needs to be re-adjusted continually (Kröbel et al., 2016). Soil carbon for native grassland systems was assumed to be at equilibrium levels (Smith, 2014). Some inputs in Holos are necessary to define, such as total area, crop types and cropping system

details, irrigation, and also number and types of animals, but there are also default values for some of the inputs, which can be overridden by the model user (Little et al., 2008), e.g., ecodistrict characteristics (Marshall et al., 1999) such as default values for soil type, soil texture, growing season precipitation, growing season potential evapotranspiration and land topography data. There are also region-specific emission factors for herbicide application, and energy use from machine operations ($GJ \cdot ha^{-1}$) which are associated with the ecodistrict characteristics and can be modified by the user (Little et al., 2008).

There are also more detailed inputs in Holos such as the ability to modify emission factors for manure systems and to design animal diets, as well different housing options, manure storage and handling options, initial and final body weight for animals, and also animal energy requirements and feed intake. Beside GHG emission investigations, the model takes into account different management strategies such as tillage type (conventional, reduced or no-tillage), fallowing, perennial crops and grassland seeding for GHG mitigations in a farm system.

4.2.4.1. Modelling setup and parameterization

The output hydrometeorological variables from the GENESYS model were used as inputs to Holos to modify ecodistrict variables. All ecodistrict-related inputs except soil type and soil texture were modified for model simulations. It was assumed that the farm GHG emissions are estimated for complete one-year beef production periods (Beauchemin et al., 2010) representative for each climate scenario (one year for baseline and six different years for each climate change scenario).

4.2.4.2. Crop modeling

As neither GENESYS nor Holos actually model crop growth, but the effect of different rates of evapotranspiration is relevant in both models, an approach, by the FAO Irrigation and Drainage Paper No. 33 (Dorenboss and Kassam, 1979), was utilized where a simple equation is used that relates relative crop yield to the corresponding relative changes in evapotranspiration. In this adjustment, Y_b and Y_s are the base and scenario yields, ET_b and ET_s are the base and the scenario evapotranspiration, and K_{ET} is a yield response factor representing the sensitivity of yield to changes in evapotranspiration ((Dorenboss and Kassam, 1979), Equation 1). Equation 4.1 is a water production function and can be applied to all agricultural crops including herbaceous vegetation, trees, and vines (Dorenboss and Kassam, 1979).

$$\left(1 - \frac{Y_b}{Y_s}\right) = K_{ET}\left(1 - \frac{ET_b}{ET_s}\right) \quad (4.1)$$

In order to model the sensitivity of the crops to water supply, different yield response factors were applied for each cropping systems (annual, perennial, and fruit trees) (Dorenboss and Kassam, 1979) to relative changes in evapotranspiration for different climate change scenarios versus the base period to estimate the relative crop yield changes (Table 4.2).

Coefficients for annual carbon accumulation of apple trees (a and b, Table 4.5) were also calculated for this study (Kort and Turnock, 2000), using the information related to apple trees carbon capture ability with age (kg C·m^{-2}·yr^{-1}) (Wu et al., 2012).

$$C_{tree} = \left(a\,(age - 2)\right)^b \quad (4.2)$$

Where, C_{tree} is carbon capture (kg C·year^{-1}), age is the tree age (year) and a and b are coefficients for annual carbon accumulation of apple trees (Kort and Turnock, 2000).

Soil direct N_2O emissions due to nitrogen fertilizer use, tillage, soil texture, topography, and irrigation and indirect N_2O emissions as a result of leaching and runoff and volatilization (Janzen et al., 2003; IPCC, 2006; Rochette et al., 2008; Wu et al., 2012; Rochette et al., 2018) and also CO_2 emissions due to energy use, herbicide manufacturing, nitrogen and phosphor production, and irrigation (Nagy, 2000; Dyer and Desjardins, 2007; Neitzert et al., 2007) from the apple production system in the simulated farm were calculated outside of Holos and then added to the final results because the current version of the model (Holos 3.0) does not have the fruit tree component to take into account fertilizers, herbicides, and irrigation applications (Table 4.3 and 4.4).

4.2.4.3. Beef modeling

The number of animals in the simulated farm system was estimated using the amount of land utilized for each total rangeland area, cropping operation, and hay production during a life cycle over an 8-year period. Further, Dry Matter (DM) intake, land productivity, utilization rate, harvest loss and feeding loss were required for the analysis (Alemu et al., 2017b). It was assumed that the breeding stock is established at the beginning of the 8-year cycle, which included newborn calves, young and growing heifers and bulls, mature cows and bulls, and lactating cows for nursing breeding stocks (Table 4.5). It was also assumed that there is an 85% annual calving rate for the progeny, all cows are pregnant and the sex ratio is 1:1 ((Alemu et al., 2017b), Table 4.5). Also, it was assumed that about 97% of the calves survived (mortality rate of 3%), and were backgrounded and finished on the farm

((Alemu et al., 2017b), Table 4.5). Calves were born in April, weaned in October and then backgrounded and finished under different diets to achieve the final weight ((Beauchemin et al., 2010; Alemu et al., 2017b), Tables 4.5 and 4.6).

The farm was assumed to not produce the total amount of barley grain necessary for the assumed cattle ranching system, and therefore must import about 162 tonnes of grains (27 ha of corresponded land) for an 8-year cycle. Further, a total of 818 tonnes of mixed hay (122 ha of corresponding land) was exported from the watershed in an 8-year cycle. It was assumed that the simulated farm was responsible for the CO_2 emissions from imported feed transportation and this emission was added to the energy related CO_2 emissions. However, the CO_2 emissions from the exported feed transportation was not considered to be included in the total GHG emissions of the simulated farm. The average CO_2 emissions for shipping of goods by modern trucking was assumed to be between 60 to 150 grams of CO_2 per metric tonnes of freight per kilometer of transportation (Emergency Community of Airport Entrepreneurs Hamburg EV, 2018). It was assumed that 162 tonnes of grains was imported from a farm located in Keremeos village or within about eight kilometers from the simulated farm, and the corresponded average CO_2 emission was estimated at about 0.136 Mg for an 8-year cycle, which is about 0.023 Mg for each year of beef production system (there are six complete beef production system in an 8-year cycle and the grain is only used for the progenies).

Table 4.5: The beef cattle farming system for the simulated farm in the Olalla watershed.

Animal category	Number of animals	Months on a specific diet	No. of days on a specific diet	Diet type	Manure
Newborn heifer calves	32	Apr	30	Milk and mixed hay	Deep-bedding
	32	May-Oct	184	Milk and native pasture	Pasture
Young heifers	32	Nov-Mar	151	Mixed hay	Deep-bedding
Growing Heifers	32	Apr	30	Mixed hay	Deep-bedding
	32	May- Oct	184	Native pasture	Pasture
	32	Nov-Mar	151	Mixed hay	Deep-bedding
Lactating Cows	33	Apr	30	Mixed hay	Deep-bedding
	33	May-Oct	184	Native pasture	Pasture
Cows [b]	32	Apr	30	Mixed hay	Deep-bedding
	32	May- Oct	184	Native pasture	Pasture
	32	Nov-March	151	Mixed hay	Deep-bedding
Newborn bull calves	1	Apr	30	Milk and mixed hay	Deep-bedding
	1	May-Oct	184	Milk and native pasture	Pasture
Young growing bulls	1	Nov-Mar	151	Mixed hay	Deep-bedding
Growing bulls	1	Apr	30	Mixed hay	Deep-bedding
	1	May- Oct	184	Native pasture	Pasture
	1	Nov-Mar	151	Mixed hay	Deep-bedding
Bulls	1	Apr	30	Mixed hay	Deep-bedding
	1	May- Oct	184	Native pasture	Native pasture
	1	Nov-March	151	Mixed hay	Deep-bedding
Newborn calves	27	Apr	30	Milk and mixed hay	Deep-bedding
	27	May-Oct	184	Milk and native pasture	Pasture
Backgrounders	26	Nov-Apr 15th	166	Mixed hay	Deep-bedding
	26	Apr 16th-Aug 13th	120	Native pasture	Pasture
Finishers	26	Aug 14th-Dec 18th	127	90% barley grain, 10% barley silage	Deep-bedding
Animal category	**Housing**	**Initial weight (kg)[a]**	**Final weight (kg)**	**ADG (kg·day^{-1})**	
Newborn heifer calves	Confined	39		0.86	
	Enclosed pasture		223		

Young heifers	Confined	223	372	0.99
Growing Heifers	Confined	372		0.58
	Enclosed pasture			
	Confined		583	
Lactating Cows	Confined	583		0.35
	Enclosed pasture		657	
Cows [b]	Confined	657		0.00
	Enclosed pasture			
	Confined		657	
Newborn bull calves	Confined	39		0.89
	Enclosed pasture		229	
Young growing bulls	Confined	229	379	0.99
Growing bulls	Confined	379		1.18
	Enclosed pasture			
	Confined		810	
Bulls	Confined	810		0.19
	Pasture			
	Confined		880	
Newborn calves	Confined	39		0.87
	Enclosed pasture		226	
Backgrounders	Confined	226		0.65
	Enclosed pasture		435	0.86
Finishers	Confined	435	637	1.60

[a] Average initial and final body weight and average daily weight gain (ADG) for animal categories on the farm is for the light continuous grazing management (Alemu et al., 2017b).
[b] It is assumed that both the initial and final weight for cows are 657 kg.

Table 4.6: Quality of diet (total digestible nutrient (TDN), crude protein (CP)) and methane conversion factor (Y_m) values for the light continuous grazing management used for different feed types in the simulated farm in the Olalla watershed.

Feed type	TND (%)	CP ($kg \cdot kg^{-1}$)	Y_m (%)
Natural rangeland	62.6	10.7	7.0
Mixed hay	63.3	16.1	7.0
Finishing diet	80.7	12.3	4.0

Furthermore, the model assumed the manure cannot be imported or exported, and emissions were estimated at the farm (Beauchemin et al., 2010; Alemu et al., 2017b). The deep-bedded system for confined housing of the cattle during fall and winter months was provided by barley straw grown in the farm and the manure was accumulated in the housing

system and transported to the barley silage and barley grain croplands once a year ((Beauchemin et al., 2010; Alemu et al., 2017b), Table 4.5). The manure was deposited on the pasture during the summer months when the animals were grazing on pasture ((Beauchemin et al., 2010; Alemu et al., 2017b), Table 4.5).

All GHGs were represented as CO_2 equivalent to account for the global warming potential of the respective gases: CH_4 kg × 23 + N_2O kg × 298 + CO_2 kg ((IPCC, 2001), Table 2). All the equations used for GHG emissions estimation from cattle ranching and crop cultivation are fully described in Beauchemin *et al.* (2010) and Alemu *et al.* (2017) (Beauchemin et al., 2010; Alemu et al., 2017b).

4.3. Results and discussion

4.3.1. The GENESYS hydrometeorological model

4.3.1.1. Monthly air temperature

The hydrometeorological modelling resulted in 30-year mean monthly air temperature increases of up to 5°C, or 51% relative to the 1961-1990 period at the simulated farm in the Olalla watershed. Predicted mean monthly air temperature increases were estimated for both greenhouse gas emission scenarios (RCP 4.5 and RCP 8.5) in each three different future periods including 2020's, 2050's and 2080's. Mean monthly air temperature changes increased from 2020's towards 2080's in Scenario 1; however, Scenario 2 showed the same pattern but similar results for 2020's and 2050's. The period 2080's in Scenario 2 showed the highest increases in mean monthly air temperature between all other scenarios and time periods (Table 4.7).

4.3.1.2. Growing season PET and growing season precipitation

The hydrometeorological modelling also showed 30-year mean total growing season PET increases of up to 41 mm or 12%. Results also suggest the 30-year mean total growing season precipitation decreased by up to 24 mm or 11%. Estimated mean total growing season PET increases and mean total growing season precipitation decreases were predicted for both greenhouse gas emission scenarios in each three different future periods. For both total growing season PET and precipitation, 2020's showed the lowest changes and 2050's and 2080's with similar results showed the highest changes in Scenario 1; however, 2020's and 2050's showed similar results and lower changes than 2080's in Scenario 2. The period 2080's in Scenario 2 showed the highest increase in mean total growing season PET and the highest decrease in mean total growing season precipitation between all other scenarios and time periods (Table 4.7).

4.3.1.3. Water supply

The results showed, relative to the 1961-1990 period, total growing season water supply decreased by 10.8%, 25.8%, and 31.4% in Scenario 1 and by 30.9%, 34%, and 49.5% in Scenario 2 for the periods 2020's, 2050's and 2080's, respectively as a result of climate change. The likely water supply reductions for different climate change scenarios and time periods relative to the 1961-1990 period, along with the higher competition for water between other sectors, will require increased surface and ground water allocations for agricultural purposes and, thus, raise energy use and CO_2 emissions. This is because the estimated reduction in water supply is more than 15%, the rate of reduction in water supply in a time of water shortage considered by the farmers in the region to be acceptable (Conrad

et al., 2017), in all the scenarios except Scenario 1 in the 2020's. Therefore, for the purpose of model application and assessment, it was assumed more surface and groundwater allocations would compensate the water supply reductions in the future. Therefore, the conversion of area irrigated to equivalent CO_2 (kg $CO_2 \cdot ha^{-1}$) was increased for different climate change scenarios and time periods relative to the 1961-1990 period. The applied percentage of increase in irrigation energy was assumed to be the same as the percentage of decreases in water supply for different climate change scenarios and time periods relative to the 1961-1990 period (Tables 4.7 and 4.8).

4.3.2. Ecodistrict emission factor and the fraction of nitrogen lost by leaching and runoff

The results suggested that changes in growing season precipitation and potential evapotranspiration (Table 4.7) decreased the ecodistrict N_2O emission factor by up to 31% (kg N_2O-N·(kg N)$^{-1}$) (Rochette et al., 2008; Rochette et al., 2018) and the fraction of nitrogen lost by leaching and runoff (kg N·(kg N)$^{-1}$) by up to 23% (Rochette et al., 2008), for different climate change scenarios and time periods relative to 1961-1990 period (Table 4.7).

Both greenhouse gas emission scenarios in each of three future periods showed decreases in the ecodistrict N_2O emission factor and the fraction of nitrogen lost by leaching and runoff. The lowest changes in the ecodistrict N_2O emission factor and the fraction of nitrogen lost by leaching and runoff was shown for 2020's and the highest changes was for 2050's and 2080's with similar results in Scenario 1; however, 2020's and 2050's showed similar results and lower changes than 2080's in Scenario 2. The greatest decreases in the

ecodistrict N_2O emission factor and the fraction of nitrogen lost by leaching and runoff was for 2080's in Scenario 2 (Table 4.7).

4.3.3. Crop yield

Results suggested different crop yield increased between 7 to 14% for different climate change scenarios and time periods relative to the 1961-1990 period (Tables 4.7 and 4.8). Different crop yield increased for both Scenario 1 and 2 in the 2020's, 2050's and, 2080's and also these changes increased from 2020's to 2080's in Scenario 1. However, 2020's and 2050's in Scenario 2 showed similar results and 2080's in Scenario 2 showed the highest increases in crop yield between all other scenarios and time periods (Table 4.7). As a result, both the below and above ground residue yield and corresponding direct and indirect N_2O emissions due to crop nitrogen inputs increased alongside.

4.3.4. Annual carbon accumulation of apple trees

Crop yield increases in apple trees resulted in an increase in annual carbon accumulation of apple trees for different climate change scenarios and time periods relative to the 1961-1990 period (8 – 14% or 1.55 to 2.77 kg $C \cdot yr^{-1}$). These changes were applied to future scenarios by selection of a and b coefficients fitted for each scenario (Table 4.8).

Table 4.7: The GENESYS-derived mean monthly temperature (°C), growing season precipitation (mm), and growing season potential evapotranspiration (mm) in the area of simulated farm and also, total growing season water volume (million m^3) at the outlet of watershed and related ecodistrict emission factor (kg N_2O-N·(kg N)$^{-1}$), and fraction of Nitrogen lost by leaching and runoff (kg N·(kg N)$^{-1}$) for the normal period of 1961-1990 and for the two emission scenarios and three future time periods, 2020s, 2050s, and 2080s.

	Baseline	Scenario 1			Scenario 2		
Month(s)	**1961-1990**	**2020s**	**2050s**	**2080s**	**2020s**	**2050s**	**2080s**
30-year mean monthly temperature (°C)							
Jan	-2.9	-1.7	-0.5	0.0	0.0	0.1	1.9
Feb	1.6	2.8	4.0	4.5	4.5	4.6	6.5
Mar	6.5	8.3	9.6	10.2	10.2	10.3	12.0
Apr	11.1	13.3	14.3	14.7	14.7	14.7	16.4
May	15.2	16.7	17.6	18.1	18.1	18.1	19.7
Jun	18.9	20.6	21.5	22.1	22.1	22.4	24.4
Jul	22.3	24.4	25.7	26.6	26.6	26.9	29.6
Aug	22.5	24.4	25.8	26.7	26.7	26.9	29.8
Sep	17.6	19.1	20.2	21.0	21.0	21.2	23.6
Oct	10.8	11.6	12.5	13.0	13.0	13.2	14.9
Nov	3.0	3.8	4.9	5.4	5.4	5.6	7.2
Dec	-2.3	-1.0	0.0	0.4	0.4	0.7	2.4
Average annual	10.4	11.9	13.0	13.6	13.6	13.7	15.7
30-year mean total growing season precipitation (mm)							
April-Sep	214	207	197	199	200	197	190
30-year mean total growing season potential evapotranspiration (mm)							
April-Sep	351	374	381	385	385	384	392
30-year mean total growing season water volume (million m^3) at the outlet of the watershed							
April-Sep	19.4	17.3	14.4	13.3	13.4	12.8	9.8
30-year mean total growing season ecodistrict emission factor (kg N_2O-N·(kg N)$^{-1}$)							
April-Sep	0.0086	0.0083	0.0065	0.0066	0.0066	0.0065	0.0059
30-year mean total growing season fraction of Nitrogen lost by leaching and runoff (kg N·(kg N)$^{-1}$)							
April-Sep	0.1733	0.1690	0.1423	0.1431	0.1440	0.1419	0.1327

Table 4.8: The change in different crop yield, coefficients (a and b) and estimated annual carbon accumulation of apple trees (kg $C \cdot yr^{-1}$), and conversion of area irrigated to kg CO_2 (kg $CO_2 \cdot ha^{-1}$) for different climate change scenarios relative to 1961-1990 for the simulated farm in the Olalla watershed.

	Value	Change for Scenario 1			Change for Scenario 2		
	Baseline	2020s	2050s	2080s	2020s	2050s	2080s
Yield [a]							
Barley silage and grain	9530 and 5975 $kg \cdot ha^{-1}$	7.5%	9.8%	11.1%	11.1%	10.8%	13.4%
Vegetables [b]	12000 $kg \cdot ha^{-1}$	7.5%	9.8%	11.1%	11.1%	10.8%	13.4%
Mixed hay	6724 $kg \cdot ha^{-1}$	7.2%	9.4%	10.7%	10.7%	10.3%	12.8%
Fruits (apple trees)	41696 $kg \cdot ha^{-1}$	7.9%	10.3%	11.6%	11.6%	1.3%	14.0%
The coefficients (a and b) and estimated annual carbon accumulation of apple trees							
C_{tree}	19.74 kg $C \cdot yr^{-1}$	7.9%	10.3%	11.6%	11.6%	11.3%	14.0%
a	0.9909	7.9%	10.3%	11.6%	11.6%	11.3%	14.0%
b	1.0351	0.0%	0.0%	0.0%	0.0%	0.0%	0.0%
Conversion of area irrigated to kg CO_2							
	367 kg $CO_2 \cdot ha^{-1}$	10.8%	25.8%	31.4%	30.9%	34.0%	49.5%

[a] Yield data were obtained from Alemu et al. (2017b) and Wu et al. (2012).
[b] The values for the vegetables are for a set of crops such as beans, cabbages, onions, peas, pepper, potatoes, sugar beets, tomatoes, and watermelons.

4.3.5. GHG emissions and soil carbon storage

The results suggest emissions decreased for enteric CH_4 between 1% to 4%, and also decreased for both manure CH_4 and manure direct N_2O between 3% to 7% for different climate change scenarios and time period relative to the 1961-1990 period (Figures 4.2 and 4.3). These emissions are functions of the net energy requirements of the livestock (Little et al., 2008). According to a study by Ngwabie et al. (2011), at moderate levels, air temperature seems to affect the behaviour of dairy cows where the daily indoor air temperature ranged from about 5 °C to about 20 °C, the daily activity of the cows decreased with increasing indoor air temperature. They concluded the corresponding CH_4 emissions of the cows decreased when their activity decreased (Ngwabie et al., 2011). Air temperature increases as a result of climate change (Table 4.7) may decrease the animal net energy requirement, and consequently enteric CH_4, manure CH_4, and manure N_2O emissions for different climate change scenarios and time period relative to the 1961-1990 period.

Total manure and crop indirect N_2O decreased between 1% to 27% for different climate change scenarios and time period relative to the 1961-1990 period (Figures 4.2 and 4.3) as a result of the reduction in the fraction of nitrogen lost by leaching and runoff. However, crop direct N_2O increased between 8% to 31% (Figures 4.3 and 4.4), because crop residue and nitrogen returns from crop residue to the soil increased for future scenarios relative to the 1961-1990 period. Crop direct N_2O is expected to be reduced due to lower emission rates from land-applied manure, and also the reduction in ecodistrict emission factors (Figure 4.3 and Table 4.7). However, the results suggest the effect of the increasing soil nitrogen returns through crop residues on crop direct N_2O outweighs the effect of the reduction of emissions from land applied manure and the overall reduction of the ecodistrict emission factor on crop direct N_2O.

CO_2 emissions from energy use are anticipated to increase between 5% to 23% for different climate change scenarios and time period relative to the 1961-1990 period (Figures 4.2 and 4.3) due to the higher energy demand for irrigation purposes.

Soil carbon storage due to fruit tree orchards would increase between 8% to 14% under the modelled conditions, for different climate change scenarios and time period relative to the 1961-1990 period (Figures 4.4 and 4.5) as a result of the increase in annual carbon accumulation of apple trees.

Finally, the results suggest that the carbon storage capability in the simulated farm at the Olalla watershed may increase from 6% to 8% for different climate change scenarios and time period relative to the base period (Figures 4.4 and 4.5). However, the simulation results without including fruit tree orchards at the simulated farm in the Olalla watershed

revealed that the total farm GHG emissions may increase from 4% to 14% as result of climate change for different climate change scenarios and time period relative to the 1961-1990 period. This shows the important effect of fruit tree orchards as a source of carbon capture in farm GHG emissions mitigation (Figure 4.6).

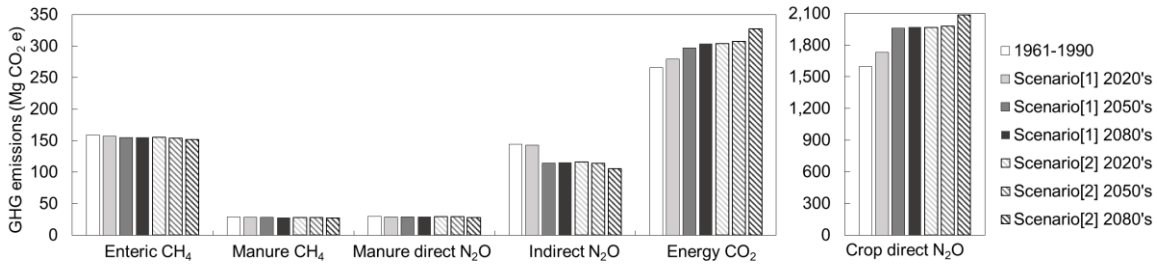

Figure 4.2: Various GHG emissions (CO_2 equivalents, Mg) resulting from the simulated farm in the Olalla watershed for the normal period of 1961-1990 and for the two emission scenarios and three future time periods, 2020s, 2050s, and 2080s.

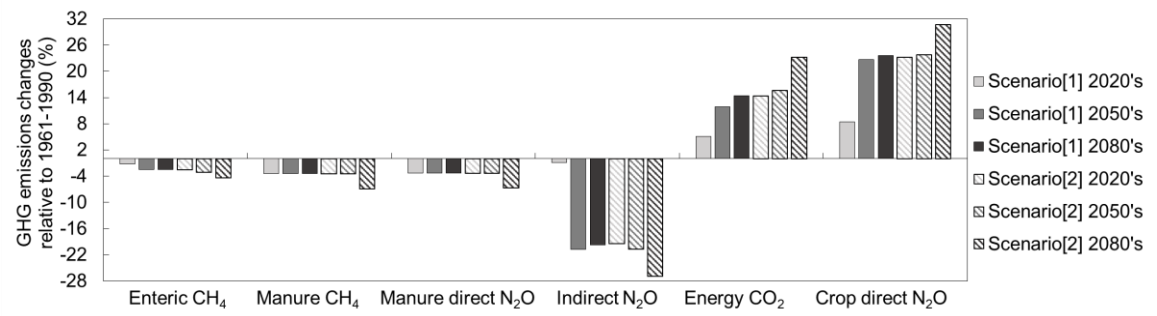

Figure 4.3: Changes in various GHG emissions resulting from the simulated farm in the Olalla watershed for the two emission scenarios and three future time periods, 2020s, 2050s, and 2080s relative to the 1961-1990 normal period.

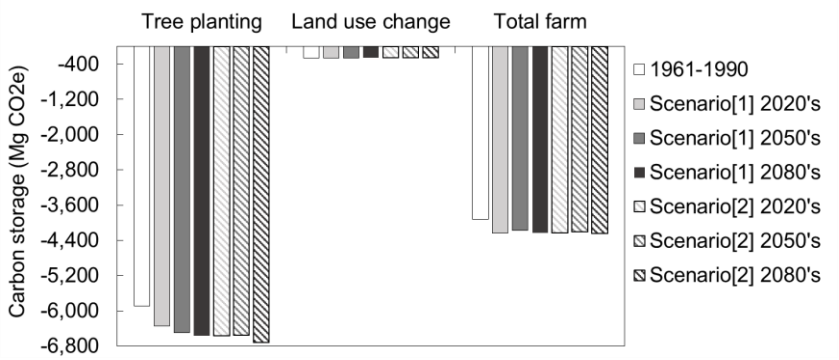

Figure 4.4: Various carbon storage (CO_2 equivalents, Mg) resulting from the simulated farm in the Olalla watershed for the normal period of 1961-1990 and for the two emission scenarios and three future time periods, 2020s, 2050s, and 2080s.

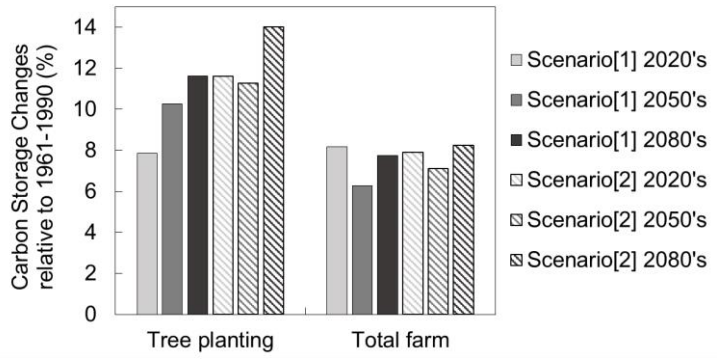

Figure 4.5: Changes in various carbon storage resulting from the simulated farm in the Olalla watershed for the two emission scenarios and three future time periods, 2020s, 2050s, and 2080s relative to the 1961-1990 normal period.

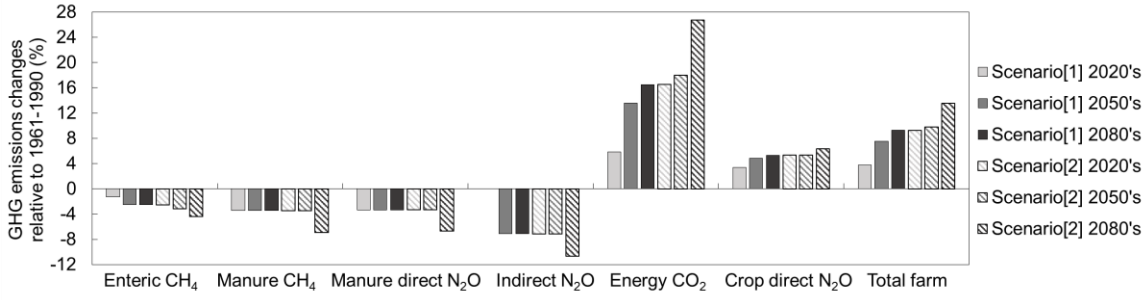

Figure 4.6: Changes in various GHG emissions resulting from the simulated farm in the Olalla watershed for the two emission scenarios and three future time periods, 2020s, 2050s, and 2080s relative to the 1961-1990 normal period without fruit tree orchards.

4.4. Conclusions

The concentration of GHGs in the atmosphere is increasing and agricultural area has been recognized as a significant source of GHG emissions. Chapter 4 estimated CO_2, CH_4, and N_2O emissions and soil carbon stocks for a simulated farm contributed to both beef and crop production at the Olalla watershed, BC.

The results of Chapter 4 suggest there may be a reduction in emissions related to enteric CH_4, manure CH_4, manure direct N_2O, and indirect N_2O for different climate change scenarios and time periods. However, there may be increases in crop direct N_2O and energy CO_2 for different climate change scenarios and time periods. Furthermore, soil carbon stocks, driven by fruit tree orchards, may also increase. This study suggests the carbon capture in the simulated farm at the Olalla watershed may increase depending on different climate change scenarios and time periods. However, if the simulation was conducted without fruit tree orchards, the total GHG emissions may increase for different climate change scenarios and time periods at the simulated farm in the Olalla watershed which represents a typical farm in the region. This shows the important effect of fruit tree orchards as a mitigation option for reducing farm GHG emissions in the region in the future. This mitigation option is likely to be more practical in the region as the results of Chapter 3 indicated that higher spring evapotranspiration especially in higher elevations, may favour orchard production in these altitudes.

Chapter 5 : Summary and conclusions

This research investigated climate change impacts on water supply and demand, and agricultural greenhouse gases (GHG) emissions in the Olalla watershed, an Okanagan-Similkameen subwatershed, British Columbia, Canada in the time-frame of 1961 to 2100 for the ensembles of 15 general circulation models (GCMs) for two Representative Concentration Pathways (RCP) scenarios (RCP 4.5 and RCP 8.5) for three different future periods, including 2020's (2011-2040), 2050's (2041-2070) and 2080's (2071-2100) relative to the 1961-1990 base period.

The Thesis addressed the following four different objectives, which were presented in Chapters 2, 3, and 4:

1. Model solar radiation using an accurate proposed solar radiation model which uses the most available input data.

2. Model historical and future water supplies under a range of climate scenarios using the Generate Earth Systems Science (GENESYS) hydrometeorological model.

3. Estimate historical vegetation water requirement and assess climate driven changes in that parameter for a range of future climate scenarios using GENESYS.

4. Link the GENESYS and Holos GHG emissions estimation models to estimate CO_2, CH_4 and N_2O emissions and soil carbon change for agricultural - both crop and animal production - processes under different climate and management scenarios.

This Thesis answered the research questions in the following manner:

1. Modeled daily solar radiation for the closest base climate station to the Olalla watershed and normal (1961-1990) mean monthly and annual solar radiation over the watershed using the proposed TRAD (temperature-estimation of radiation) model which uses ambient air temperature, a Digital Elevation Model (DEM), time of year, and monthly radiation estimates from Esri Solar Analyst.

2. Modeled historical and future water supply and vegetation water demand under a range of climate scenarios using the GENESYS model in the Olalla watershed and reveled possible future changes in water supply and demand that may stress future water resources management in the watershed.

3. Linked the GENESYS and the Holos models and estimated GHG emissions (CO_2, CH_4 and, N_2O) and soil carbon change for both crop and animal production processes in a simulated farm in the Olalla watershed under different climate and management scenarios, showed how climate change may affect future agricultural GHG emissions, and introduced the available mitigation options.

In Chapter 2, a daily solar radiation estimation method which uses ambient air temperature, a DEM, time of year, and monthly radiation estimates from Solar Analyst model was proposed. Accurate and precise estimation of spatio-temporal variability of solar radiation is critical for climate studies. Some commonly used models evaluate this variability using methods in which the data required for estimating atmospheric attenuation may not be easily accessible for some study areas. The objective was to use air temperature-based empirical models for atmospheric transmissivity and diffuse fractions to vary total monthly radiation estimation from Solar Analyst, and then calculate total daily radiation as

a fraction of total monthly radiation by applying a daily transmissivity-based ratio, as air temperature data is readily available at most locations on the planet.

The results of Chapter 2 revealed that daily solar radiation can be estimated very well, with a Mean Absolute Bias Error (MBE) of around 40 to 53 $W \cdot m^{-2}$ or a MBE of ±10%, under all sky conditions at seven sites in diverse climate regions, using significantly less input data. The presented method is an improvement over previously used methods with a MBE of under 10% but more input parameters. The results also showed the method is more useful for those stations with substantially higher numbers of sunny days than cloudy or partly cloudy days because the uncertainty of the model decreased from cloudy to sunny sky conditions. The implemented DEM environment of this method makes it applicable in many studies that need high resolution estimations of solar radiation across complex terrain. Hourly solar radiation values are modelled using a ratio between daily and hourly radiation, based on literature values and estimated daily insolation. The proposed solar radiation estimation method was used to estimate daily solar radiation for the base climate station closest to the Olalla watershed and normal (1961-1990) mean annual and monthly solar radiation over the watershed.

In Chapter 3, the effects of climate change on spring and summer water supply and spring and summer water demand related to the vegetation cover in the Olalla watershed in the Regional District of Okanagan-Similkameen (RDOS), southern British Columbia, Canada, in the time-frame of 1961 to 2100 were investigated. The GENESYS spatial hydrometeorological model was applied to predict the potential changes for the ensembles of 15 GCMs for two RCP scenarios (RCP 4.5 and RCP 8.5) for three different future

periods, including 2020's (2011-2040), 2050's (2041-2070) and 2080's (2071-2100) relative to the 1961-1990 base period.

Chapter 3 results indicate that the timing of snowmelt will likely occur one month earlier for all scenarios except Scenario 2 in the 2080's, where the timing of snowmelt may be two months earlier relative to the 1961-1990 period. There may be increases in the future total spring water supply from 35% to 39% and decreases in summer water supply from 36% to 79% relative to the 1961-1990 period based on the scenarios. Average spring vegetation water demand may increase from 20% to 47% but summer vegetation water demand may decrease from 10% to 29% relative to the 1961-1990 period based on the scenarios. These changes are expected to put stress on the future water resource management, on agricultural and forest productivity, and on ecosystem functions in the watershed.

The concentration of GHGs in the atmosphere is increasing and agricultural areas are recognized as a significant source of GHG emissions, and may be increasing GHG emission in a warmer world (Kröbel et al., 2016). Chapter 4 analyses evaluated CO_2, CH_4 and N_2O emissions and soil carbon storage changes for a simulated farm with both beef and crop production in the Olalla watershed. In Chapter 4, the GENESYS model output representing a range of future climate scenarios (current and future hydrometeorological conditions in the study area) were adapted to provide the Holos model inputs. Adapting the GENESYS output facilitated Holos modelling of farm GHG emissions under two greenhouse gas emission scenarios (RCP 4.5 and RCP 8.5) for three different future periods (2011-2040, 2041-2070 and 2071-2100) relative to the 1961-1990 base period.

The results of Chapter 4 showed that there may be reductions in emissions related to enteric CH_4, manure CH_4, manure direct N_2O, and indirect N_2O for different climate change scenarios and time periods. However, there may also be increases in crop direct N_2O and energy CO_2 for the same scenarios. Furthermore, soil carbon storage under fruit tree orchards would be expected to increase. According to this result, the simulated farm at the Olalla watershed is a carbon sink and the carbon capture will likely increase to higher levels, depending on different climate change scenarios and time periods. However, if the simulation was conducted without fruit tree orchards as a carbon sink, the simulated farm at the Olalla watershed is a carbon emitter and the carbon emissions will likely increase for different climate changes scenarios and time periods. This shows the important effect of fruit tree orchards as a mitigation option for reducing farm GHG emissions in the future which is likely to be more practical in the region as Chapter 3 indicated higher spring evapotranspiration especially in higher elevations, may favour orchard production in these altitudes.

5.1. Recommendations for future research

This Thesis modelled climate change impacts on water supply and demand, and agricultural GHG emissions in an Okanagan-Similkameen subwatershed, British Columbia, Canada. A number of recommendations for future research and development have been identified.

- The proposed TRAD model presented in Chapter 2 should be developed as an independent software package or an extension to ESRI Solar Analyst in order to be available for different users and applications.

- In Chapter 3, the impacts of climate change on water supply and vegetation water demand were assessed; however, focus should be placed on subsequent changes in land cover as a result of the anticipated changes in water supply and vegetation water demand. These land cover changes should be studied especially with a particular focus on the changes in forest and agricultural land covers, for example, suitability assessment of climate conditions for fruit growing in higher elevations.
- In Chapter 4, fruit growing was introduced as a mitigation option for GHG emissions from agriculture in the watershed. However, the economic feasibility should be identified by using the economic assessment option in the Holos model. Other cropping system management strategies other than fruit tree orchards that may result in lower GHG emissions and be economically viable may also be taken into account.

References

Agriculture and Agri-Food Canada, 1996. Soil Landscapes of Canada, v.2.2, Center for Land and Biological Resources Research, Agriculture and Agri-Food Canada, Ottawa.

Aladenola, O.O., Madramootoo, C.A., 2014. Evaluation of solar radiation estimation methods for reference evapotranspiration estimation in Canada. Theoretical and Applied Climatology, 118(3): 377-385. DOI:10.1007/s00704-013-1070-2

Alemu, A.W., Amiro, B.D., Bittman, S., MacDonald, D., Ominski, K.H., 2017a. Greenhouse gas emission of Canadian cow-calf operations: A whole-farm assessment of 295 farms. Agricultural Systems, 151: 73-83.

Alemu, A.W., Janzen, H., Little, S., Hao, X., Thompson, D.J., Baron, V., Iwaasa, A., Beauchemin, K.A., Kröbel, R., 2017b. Assessment of grazing management on farm greenhouse gas intensity of beef production systems in the Canadian Prairies using life cycle assessment. Agricultural Systems, 158: 1-13.

Antle, J., Capalbo, S., Mooney, S., Elliott, E.T., Paustian, K.H., 2002. Sensitivity of carbon sequestration costs to soil carbon rates. Environmental Pollution, 116(3): 413-422.

Atwater, M.A., Ball, J., 1978. A numerical solar radiation model based on standard meteorological observations. Solar Energy, 21(3): 163-170.

Augustine, J.A., DeLuisi, J.J., Long, C.N., 2000. SURFRAD—A national surface radiation budget network for atmospheric research. Bulletin of the American Meteorological Society, 81(10): 2341-2357.

Augustine, J.A., Hodges, G.B., Cornwall, C.R., Michalsky, J.J., Medina, C.I., 2005. An update on SURFRAD—The GCOS surface radiation budget network for the continental United States. Journal of Atmospheric and Oceanic Technology, 22(10): 1460-1472.

Badescu, V., Gueymard, C.A., Cheval, S., Oprea, C., Baciu, M., Dumitrescu, A., Iacobescu, F., Milos, I., Rada, C., 2012. Computing global and diffuse solar hourly irradiation on clear sky. Review and testing of 54 models. Renewable and Sustainable Energy Reviews, 16(3): 1636-1656.

Barnett, T.P., Adam, J.C., Lettenmaier, D.P., 2005. Potential impacts of a warming climate on water availability in snow-dominated regions. Nature, 438(7066): 303-309.

BC Government, 2018. BC Fresh Water Atlas, BC Data Catalogue.

BC Ministry of Agriculture Food and Fisheries, 2001. Water consevation factsheet, crop coefficients for use in irrigation scheduling, BC Ministry of Environment.

BC Ministry of Environment, 2016. Terrestrial Ecosystem Information (TEI) Access to Maps and Data, BC Soil mapping dataset, BC Ministry of Environment.

BC Ministry of Environment Lands and Parks, 1981. Water quality assessment and objectives for Keremeos Creek Watershed, Okanagan area, BC Ministry of Environment.

Beauchemin, K., Janzen, H., Little, S., McAllister, T., McGinn, S., 2011. Mitigation of greenhouse gas emissions from beef production in western Canada–Evaluation using farm-based life cycle assessment. Animal Feed Science and Technology, 166: 663-677.

Beauchemin, K.A., Janzen, H.H., Little, S.M., McAllister, T.A., McGinn, S.M., 2010. Life cycle assessment of greenhouse gas emissions from beef production in western Canada: A case study. Agricultural Systems, 103(6): 371-379.

Beyer, H.G., Costanzo, C., Heinemann, D., 1996. Modifications of the Heliosat procedure for irradiance estimates from satellite images. Solar Energy, 56(3): 207-212.

Bird, R.E., Hulstrom, R.L., 1981. Simplified clear sky model for direct and diffuse insolation on horizontal surfaces, Solar Energy Research Inst., Golden, CO (USA).

Boé, J., Terray, L., 2008. Uncertainties in summer evapotranspiration changes over Europe and implications for regional climate change. Geophysical Research Letters, 35(5): 1-5.

Bonesmo, H., Little, S., Harstad, O.M., Beauchemin, K.A., Skjelvåg, A.O., Sjelmo, O., 2012. Estimating farm-scale greenhouse gas emission intensity of pig production in Norway. Acta Agriculturae Scandinavica, Section A–Animal Science, 62(4): 318-325.

Bristow, K.L., Campbell, G.S., 1984. On the relationship between incoming solar radiation and daily maximum and minimum temperature. Agricultural and Forest Meteorology, 31(2): 159-166.

Burney, J.A., Davis, S.J., Lobell, D.B., 2010. Greenhouse gas mitigation by agricultural intensification. Proceedings of the National Academy of Sciences, 107(26): 12052-12057.

Carroll, J., 1985. Global transmissivity and diffuse fraction of solar radiation for clear and cloudy skies as measured and as predicted by bulk transmissivity models. Solar Energy, 35(2): 105-118.

Chai, L., Kröbel, R., MacDonald, D., Bittman, S., Beauchemin, K.A., Janzen, H.H., McGinn, S.M., Vanderzaag, A., 2016. An ecoregion-specific ammonia emissions inventory of Ontario dairy farming: Mitigation potential of diet and manure management practices. Atmospheric Environment, 126: 1-14.

Cohen, S., Neilsen, D., Smith, S., Neale, T., Taylor, B., Barton, M., Merritt, W., Alila, Y., Shepherd, P., Mcneill, R., 2006. Learning with local help: expanding the dialogue on climate change and water management in the Okanagan Region, British Columbia, Canada. Climatic Change, 75(3): 331-358.

Cohen, S.J., Miller, K.A., Hamlet, A.F., Avis, W., 2000. Climate change and resource management in the Columbia River Basin. Water International, 25(2): 253-272.

Collares-Pereira, M., Rabl, A., 1979. The average distribution of solar radiation-correlations between diffuse and hemispherical and between daily and hourly insolation values. Solar Energy, 22(2): 155-164.

Colli, A., Pavanello, D., Zaaiman, W.J., Heiser, J., Smith, S., 2016. Statistical analysis of weather conditions based on the Clearness Index and correlation with meteorological variables. International Journal of Sustainable Energy, 35(6): 523-536.

Conrad, S.A., Rutherford, M.B., Haider, W., 2017. Profiling Farmers' Preferences about Drought Response Policies Using a Choice Experiment in the Okanagan Basin, Canada. Water Resources Management, 31(9): 2837-2851.

Davidson, E.A., Janssens, I.A., 2006. Temperature sensitivity of soil carbon decomposition and feedbacks to climate change. Nature, 440(7081): 165-173.

DeWalle, D.R., Henderson, Z., Rango, A., 2002. Spatial and temporal variations in snowmelt degree-day factors computed from SNOTEL data in the Upper Rio Grande basin, Proceedings of the Western Snow Conference. Colorado State University, pp. 73.

Diaz-Nieto, J., Wilby, R.L., 2005. A comparison of statistical downscaling and climate change factor methods: impacts on low flows in the River Thames, United Kingdom. Climatic Change, 69(2): 245-268.

Dorenboss, J., Kassam, A., 1979. Yield response to water irrigation and drainage, Paper 33. FAO, Rome. Italy.

Dubayah, R., Rich, P.M., 1995. Topographic solar radiation models for GIS. International Journal of Geographical Information Systems, 9(4): 405-419. DOI:10.1080/02693799508902046

Dyer, J., Desjardins, R., 2007. Energy based GHG emissions from Canadian agriculture. Journal of the Energy Institute, 80(2): 93-95.

Emergency Community of Airport Entrepreneurs Hamburg EV, 2018. Climate killer aircraft

Environment Canada, 2015. HYDAT database, Environment Canada.

Environment Canada, 2016. Historical climate data, Environment Canada.

Fu, P., Rich, P.M., 2002. A geometric solar radiation model with applications in agriculture and forestry. Computers and Electronics in Agriculture, 37(1-3): 25-35.

Gago, E.J., Etxebarria, S., Tham, Y., Aldali, Y., Muneer, T., 2011. Inter-relationship between mean-daily irradiation and temperature, and decomposition models for hourly irradiation and temperature. International Journal of Low-Carbon Technologies, 6(1): 22-37. DOI:10.1093/ijlct/ctq039

Glassy, J.M., Running, S.W., 1994. Validating Diurnal Climatology Logic of the MT-CLIM Model Across a Climatic Gradient in Oregon. Ecological Applications, 4(2): 248-257.

Gregorich, E.G., Janzen, H., Ellert, B.H., Helgason, B.L., Qian, B., Zebarth, B.J., Angers, D.A., Beyaert, R.P., Drury, C.F., Duguid, S.D., 2017. Litter decay controlled by temperature, not soil properties, affecting future soil carbon. Global Change Biology, 23(4): 1725-1734.

Gueymard, C.A., 2008. REST2: High-performance solar radiation model for cloudless-sky irradiance, illuminance, and photosynthetically active radiation–Validation with a benchmark dataset. Solar Energy, 82(3): 272-285.

Gueymard, C.A., Ruiz-Arias, J.A., 2015. Validation of direct normal irradiance predictions under arid conditions: A review of radiative models and their turbidity-dependent performance. Renewable and Sustainable Energy Reviews, 45: 379-396.

Gul, M.S., Muneer, T., Kambezidis, H.D., 1998. Models for obtaining solar radiation from other meteorological data. Solar Energy, 64(1): 99-108.

Guyader, J., Little, S., Kröbel, R., Benchaar, C., Beauchemin, K.A., 2017. Comparison of greenhouse gas emissions from corn-and barley-based dairy production systems in Eastern Canada. Agricultural Systems, 152: 38-46.

Hamlet, A.F., Lettenmaier, D.P., 1999. Effects of climate change on hydrology and water resources in the Columbia River basin. JAWRA Journal of the American Water Resources Association, 35(6): 1597-1623.

Harma, K.J., Johnson, M.S., Cohen, S.J., 2012. Future water supply and demand in the Okanagan Basin, British Columbia: a scenario-based analysis of multiple, interacting stressors. Water Resources Management, 26(3): 667-689.

Hawas, M., Muneer, T., 1984. Study of diffuse and global radiation characteristics in India. Energy Conversion and Management, 24(2): 143-149.

Hectares BC, 2015. Hectares BC, Hectares BC.

Hedstrom, N., Pomeroy, J., 1998. Measurements and modelling of snow interception in the boreal forest. Hydrological Processes, 12(10): 1611-1625.

Hünerberg, M., Little, S.M., Beauchemin, K.A., McGinn, S.M., O'Connor, D., Okine, E.K., Harstad, O.M., Kröbel, R., McAllister, T.A., 2014. Feeding high concentrations of corn dried distillers' grains decreases methane, but increases nitrous oxide emissions from beef cattle production. Agricultural Systems, 127: 19-27.

Hungerford, R.D., Nemani, R.R., Running, S.W., Coughlan, J.C., 1989. MTCLIM: a mountain microclimate simulation model. US Department of Agriculture, Forest Service, Intermountain Research Station. 52 p., 414.

Ineichen, P., 2008. A broadband simplified version of the Solis clear sky model. Solar Energy, 82(8): 758-762.

IPCC, 2001. Third Assessment Report, Climate Change: The Scientific Basis Contribution of Working Group I to the Third Assessment Report of the IPCC (Table 6.7).

IPCC, 2006. 2006 IPCC guidelines for national greenhouse gas inventories. Intergovernmental Panel on Climate Change.

IPCC, 2014. Climate change 2014: Mitigation of climate change, 3. Cambridge University Press.

Janzen, H., Angers, D., Boehm, M., Bolinder, M., Desjardins, R., Dyer, J., Ellert, B., Gibb, D., Gregorich, E., Helgason, B., 2006. A proposed approach to estimate and reduce

net greenhouse gas emissions from whole farms. Canadian Journal of Soil Science, 86(3): 401-418.

Janzen, H., Beauchemin, K., Bruinsma, Y., Campbell, C., Desjardins, R., Ellert, B., Smith, E., 2003. The fate of nitrogen in agroecosystems: An illustration using Canadian estimates. Nutrient Cycling in Agroecosystems, 67(1): 85-102.

Jost, G., Weber, F., 2012. Potential Impacts of Climate Change on BC Hydro's Water Resources., BC Hydro.

Kasten, F., Czeplak, G., 1980. Solar and terrestrial radiation dependent on the amount and type of cloud. Solar Energy, 24(2): 177-189.

Kienzle, S.W., 2008. A new temperature based method to separate rain and snow. Hydrological Processes, 22(26): 5067-5085.

Kienzle, S.W., 2011. Effects of area under-estimations of sloped mountain terrain on simulated hydrological behaviour: a case study using the ACRU model. Hydrological Processes, 25(8): 1212-1227.

Knowles, N., Dettinger, M.D., Cayan, D.R., 2006. Trends in snowfall versus rainfall in the western United States. Journal of Climate, 19(18): 4545-4559.

Kodysh, J.B., Omitaomu, O.A., Bhaduri, B.L., Neish, B.S., 2013. Methodology for estimating solar potential on multiple building rooftops for photovoltaic systems. Sustainable Cities and Society, 8: 31-41.

Kort, J., Turnock, R., 2000. Annual carbon accumulations in agroforestry plantations—an Agrifood Innovation Fund project. PFRA Shelterbelt Cent., Agric. AgriFood Can., Indian Head, SK.

Kröbel, R., Bolinder, M., Janzen, H., Little, S., Vandenbygaart, A., Kätterer, T., 2016. Canadian farm-level soil carbon change assessment by merging the greenhouse gas model Holos with the Introductory Carbon Balance Model (ICBM). Agricultural Systems, 143: 76-85.

Kröbel, R., Janzen, H., Beauchemin, K., Bonesmo, H., Little, S., McAllister, T., 2012. A proposed approach to estimate and reduce the environmental impact from whole farms. Acta Agriculturae Scandinavica, Section A–Animal Science, 62(4): 225-232.

Lapp, S., Byrne, J., Townshend, I., Kienzle, S., 2005. Climate warming impacts on snowpack accumulation in an alpine watershed. International Journal of Climatology, 25(4): 521-536.

Larson, R.P., Byrne, J.M., Johnson, D.L., Kienzie, S.W., Letts, M.G., 2011. Modelling climate change impacts on spring runoff for the Rocky Mountains of Montana and Alberta II: runoff change projections using future scenarios. Canadian Water Resources Journal, 36(1): 35-52.

Legesse, G., Beauchemin, K., Ominski, K., McGeough, E., Kroebel, R., MacDonald, D., Little, S., McAllister, T., 2016. Greenhouse gas emissions of Canadian beef production in 1981 as compared with 2011. Animal Production Science, 56(3): 153-168.

Leith, R.M., Whitfield, P.H., 1998. Evidence of climate change effects on the hydrology of streams in south-central BC. Canadian Water Resources Journal, 23(3): 219-230.

Little, S., Linderman, J., Maclean, K., Janzen, H., 2008. HOLOS–a tool to estimate and reduce greenhouse gases from farms. Methodology and algorithms for versions 1.1. x. Agriculture and Agri-Food Canada, Cat. No, A52-136/2008E-PDF.

Liu, B.Y., Jordan, R.C., 1960. The interrelationship and characteristic distribution of direct, diffuse and total solar radiation. Solar Energy, 4(3): 1-19.

MacDonald, R.J., Boon, S., Byrne, J.M., Robinson, M.D., Rasmussen, J.B., 2013. Potential future climate effects on mountain hydrology, stream temperature, and native salmonid life history. Canadian Journal of Fisheries and Aquatic Sciences, 71(2): 189-202.

MacDonald, R.J., Byrne, J.M., Boon, S., Kienzle, S.W., 2012. Modelling the potential impacts of climate change on snowpack in the North Saskatchewan River Watershed, Alberta. Water Resources Management, 26(11): 3053-3076.

MacDonald, R.J., Byrne, J.M., Kienzle, S.W., 2009. A physically based daily hydrometeorological model for complex mountain terrain. Journal of Hydrometeorology, 10(6): 1430-1446.

MacDonald, R.J., Byrne, J.M., Kienzle, S.W., Larson, R.P., 2011. Assessing the potential impacts of climate change on mountain snowpack in the St. Mary River watershed, Montana. Journal of Hydrometeorology, 12(2): 262-273.

Magruder, I.A., Woessner, W.W., Running, S.W., 2009. Ecohydrologic process modeling of mountain block groundwater recharge. Groundwater, 47(6): 774-785.

Marshall, I., Schut, P., Ballard, M., 1999. A national ecological framework for Canada: Attribute data. Ottawa, Ontario: Environmental Quality Branch, Ecosystems Science Directorate, Environment Canada and Research Branch. Agriculture and Agri-Food Canada.

Mauser, W., Bach, H., 2009. PROMET–Large scale distributed hydrological modelling to study the impact of climate change on the water flows of mountain watersheds. Journal of Hydrology, 376(3): 362-377.

Maxwell, E.L., 1998. METSTAT—The solar radiation model used in the production of the National Solar Radiation Data Base (NSRDB). Solar Energy, 62(4): 263-279.

Mc Geough, E., Little, S., Janzen, H., McAllister, T., McGinn, S., Beauchemin, K., 2012. Life-cycle assessment of greenhouse gas emissions from dairy production in Eastern Canada: a case study. Journal of Dairy Science, 95(9): 5164-5175.

McKenney, D.W., Pelland, S., Poissant, Y., Morris, R., Hutchinson, M., Papadopol, P., Lawrence, K., Campbell, K., 2008. Spatial insolation models for photovoltaic energy in Canada. Solar Energy, 82(11): 1049-1061. DOI:https://doi.org/10.1016/j.solener.2008.04.008

McKenney, M.S., Rosenberg, N.J., 1993. Sensitivity of some potential evapotranspiration estimation methods to climate change. Agricultural and Forest Meteorology, 64(1-2): 81-110.

Merritt, W.S., Alila, Y., Barton, M., Taylor, B., Cohen, S., Neilsen, D., 2006. Hydrologic response to scenarios of climate change in sub watersheds of the Okanagan basin, British Columbia. Journal of Hydrology, 326(1): 79-108.

Miklánek, P., Mészároš, I., 1993. Modelling of insolation characteristics in mountainous environment. Advances in Water Sciences, 2: 32-36.

Miles, E.L., Snover, A.K., Hamlet, A.F., Callahan, B., Fluharty, D., 2000. Pacific Northwest regional assessment: the impacts of climate variability and climate change on the water resources of the Columbia River Basin. JAWRA Journal of the American Water Resources Association, 36(2): 399-420.

Mirmasoudi, S., Byrne, J., Kroebel, R., Johnson, D., MacDonald, R., 2018. A novel time-effective model for daily distributed solar radiation estimates across variable terrain. International Journal of Energy and Environmental Engineering: 1-16.

Mockus, V., 1972. Estimation of direct runoff from storm rainfall. Chapter 10, Section 4 (Hydrology), National Engineering Handbook. Soil Conservation Service, US Dept. Agriculture.

Morrison, J., Quick, M.C., Foreman, M.G., 2002. Climate change in the Fraser River watershed: flow and temperature projections. Journal of Hydrology, 263(1): 230-244.

Moss, R.H., Edmonds, J.A., Hibbard, K.A., Manning, M.R., Rose, S.K., Van Vuuren, D.P., Carter, T.R., Emori, S., Kainuma, M., Kram, T., 2010. The next generation of scenarios for climate change research and assessment. Nature, 463(7282): 747.

Muneer, T., Gul, M., Kambezidis, H., 1998. Long-term evaluation of a meteorological solar radiation model against UK data. Energy Conversion and Management, 39: 303-17.

Myers, D.R., 2005. Solar radiation modeling and measurements for renewable energy applications: data and model quality. Energy, 30(9): 1517-1531.

Nagy, C., 2000. Energy and greenhouse gas emission coefficients for inputs used in agriculture. Report to the Prairie Adaptation Research Collaborative: 11.

Najafi, M.R., Zwiers, F.W., Gillett, N.P., 2017. Attribution of Observed Streamflow Changes in Key British Columbia Drainage Basins. Geophysical Research Letters.

NASA LP DAAC, 2000. Leaf Area Index - Fraction of Photosynthetically Active Radiation 8-Day L4 Global 1km, NASA EOSDIS Land Processes DAAC, USGS Earth Resources Observation and Science (EROS) Center (https://lpdaac.usgs.gov/).

NASA LP DAAC, 2011. Advanced Spaceborne Thermal Emission and Reflection Radiometer (ASTER) Global Digital Elevation Model, NASA EOSDIS Land Processes DAAC, USGS Earth Resources Observation and Science (EROS) Center (https://lpdaac.usgs.gov/).

Nash, J.E., Sutcliffe, J.V., 1970. River flow forecasting through conceptual models part I—A discussion of principles. Journal of Hydrology, 10(3): 282-290.

Neilsen, D., Smith, C., Frank, G., Koch, W., Alila, Y., Merritt, W., Taylor, W., Barton, M., Hall, J., Cohen, S., 2006. Potential impacts of climate change on water availability

for crops in the Okanagan Basin, British Columbia. Canadian Journal of Soil Science, 86(5): 921-936.

Neitzert, F., Cheng, L., Collas, P., Matin, A., Folliet, N., McKibbon, S., 2007. National inventory report of greenhouse gas sources and sinks in Canada 1990-2005: the Canadian Government's submission to the UN Framework Convention on Climate Change: executive summary.

Nemeth, M.W., 2010. Climate change impacts on streamflow in the upper North Saskatchewan River Basin, Alberta, University of Lethbridge, Department of Geography.

Ngwabie, N., Jeppsson, K.-H., Gustafsson, G., Nimmermark, S., 2011. Effects of animal activity and air temperature on methane and ammonia emissions from a naturally ventilated building for dairy cows. Atmospheric Environment, 45(37): 6760-6768.

Nottrott, A., Kleissl, J., 2010. Validation of the NSRDB–SUNY global horizontal irradiance in California. Solar Energy, 84(10): 1816-1827.

Ogliari, E., Grimaccia, F., Leva, S., Mussetta, M., 2013. Hybrid predictive models for accurate forecasting in PV systems. Energies, 6(4): 1918-1929.

Olatomiwa, L., Mekhilef, S., Shamshirband, S., Mohammadi, K., Petković, D., Sudheer, C., 2015. A support vector machine–firefly algorithm-based model for global solar radiation prediction. Solar Energy, 115: 632-644.

Page, J.K., 1986. Prediction of solar radiation on inclined surfaces, 3. Springer.

Paulescu, M., Schlett, Z., 2003. A simplified but accurate spectral solar irradiance model. Theoretical and Applied Climatology, 75(3): 203-212.

Quan, D.M., Ogliari, E., Grimaccia, F., Leva, S., Mussetta, M., 2013. Hybrid model for hourly forecast of photovoltaic and wind power, Fuzzy Systems (FUZZ), 2013 IEEE International Conference on. IEEE, pp. 1-6.

Regional District of Okanagan-Similkameen, 2011a. Flood prevention plan for Keremeos Creek (Olalla Townsite), Onsite Engineering Ltd and Streamworks Consulting Inc.

Regional District of Okanagan-Similkameen, 2011b. Similkameen river water management plan: part 1- scoping study, Similkameen Valley Planning Society.

Regional District of Okanagan-Similkameen, 2017. Map of Similkameen River watershed hydrometric and meteorological monitoring stations, points of diversions, and dam locations. Regional District of Okanagan-Similkameen.

Rigollier, C., Bauer, O., Wald, L., 2000. On the clear sky model of the ESRA—European Solar Radiation Atlas—with respect to the Heliosat method. Solar Energy, 68(1): 33-48.

Rochette, P., Liang, C., Pelster, D., Bergeron, O., Lemke, R., Kroebel, R., MacDonald, D., Yan, W., Flemming, C., 2018. Soil nitrous oxide emissions from agricultural soils in Canada: Exploring relationships with soil, crop and climatic variables. Agriculture, Ecosystems & Environment, 254: 69-81.

Rochette, P., Worth, D.E., Lemke, R.L., McConkey, B.G., Pennock, D.J., Wagner-Riddle, C., Desjardins, R., 2008. Estimation of N2O emissions from agricultural soils in Canada. I. Development of a country-specific methodology. Canadian Journal of Soil Science, 88(5): 641-654.

Ruiz-Arias, J., Tovar-Pescador, J., Pozo-Vázquez, D., Alsamamra, H., 2009. A comparative analysis of DEM-based models to estimate the solar radiation in mountainous terrain. International Journal of Geographical Information Science, 23(8): 1049-1076.

Schnorbus, M., Werner, A., Bennett, K., 2014. Impacts of climate change in three hydrologic regimes in British Columbia, Canada. Hydrological Processes, 28(3): 1170-1189.

SCS, 1985. National engineering handbook, Section 4: Hydrology. United States Department of Agriculture, Soil Conservation Service Washington, DC.

Sen, Z., 2008. Solar energy fundamentals and modeling techniques: atmosphere, environment, climate change and renewable energy. Springer Science & Business Media.

Sheppard, D.L., 1996. Modelling the spatial characteristics of hydrometeorology in the upper Oldman River basin, Alberta, Lethbridge, Alta.: University of Lethbridge, Faculty of Arts and Science, 1996.

Shrestha, R.R., Schnorbus, M.A., Werner, A.T., Berland, A.J., 2012. Modelling spatial and temporal variability of hydrologic impacts of climate change in the Fraser River basin, British Columbia, Canada. Hydrological Processes, 26(12): 1840-1860.

Smit, B., Skinner, M.W., 2002. Adaptation options in agriculture to climate change: a typology. Mitigation and Adaptation Strategies for Global Change, 7(1): 85-114.

Smith, P., 2014. Do grasslands act as a perpetual sink for carbon? Global Change Biology, 20(9): 2708-2711.

Spencer, J., 1971. Fourier series representation of the position of the sun. Search, 2(5): 172-172.

Statistics Canada, 2006. Census of Agriculture, Farm Data and Farm Operator Data (95-629-X).

Stewart, A., Little, S., Ominski, K., Wittenberg, K., Janzen, H., 2009. Evaluating greenhouse gas mitigation practices in livestock systems: an illustration of a whole-farm approach. The Journal of Agricultural Science, 147(4): 367-382.

Stocker, T., 2014. Climate change 2013: the physical science basis: Working Group I contribution to the Fifth assessment report of the Intergovernmental Panel on Climate Change. Cambridge University Press.

Šúri, M., Hofierka, J., 2004. A new GIS-based solar radiation model and its application to photovoltaic assessments. Transactions in GIS, 8(2): 175-190.

Taylor, P., 1998. The thermodynamic effects of sublimating, blowing snow in the atmospheric boundary layer. Boundary-Layer Meteorology, 89(2): 251-283.

Tham, Y., Muneer, T., Davison, B., 2010. Estimation of hourly averaged solar irradiation: evaluation of models. Building Services Engineering Research and Technology, 31(1): 9-25.

Thornton, P.E., Running, S.W., 1999. An improved algorithm for estimating incident daily solar radiation from measurements of temperature, humidity, and precipitation. Agricultural and Forest Meteorology, 93(4): 211-228.

USDA, S., 1986. Urban hydrology for small watersheds. Technical Release, 55: 2-6.

Valiantzas, J.D., 2006. Simplified versions for the Penman evaporation equation using routine weather data. Journal of Hydrology, 331(3): 690-702.

von Hoyningen-Huene, J., 1981. Die Interzeption des Niederschlags in landwirtschaftlichen Pflanzenbeständen. Arbeitsbericht Deutscher Verband für Wasserwirtschaft und Kulturbau, DVWK.

Walker, W.R., Skogerboe, G.V., 1987. Surface irrigation. Theory and practice. Prentice-Hall.

Wang, T., Hamann, A., Spittlehouse, D., Carroll, C., 2016. Locally downscaled and spatially customizable climate data for historical and future periods for North America. PLoS One, 11(6): e0156720.

Wang, T., Hamann, A., Spittlehouse, D.L., Murdock, T.Q., 2012. ClimateWNA—high-resolution spatial climate data for western North America. Journal of Applied Meteorology and Climatology, 51(1): 16-29.

Whillier, A., 1956. The determination of hourly values of total solar radiation from daily summations. Theoretical and Applied Climatology, 7(2): 197-204.

Willmott, C.J., Matsuura, K., 2005. Advantages of the mean absolute error (MAE) over the root mean square error (RMSE) in assessing average model performance. Climate Research, 30(1): 79-82.

Wilson, J.P., Gallant, J.C., 2000. Terrain analysis: principles and applications. John Wiley & Sons.

Wu, T., Wang, Y., Yu, C., Chiarawipa, R., Zhang, X., Han, Z., Wu, L., 2012. Carbon sequestration by fruit trees-Chinese apple orchards as an example. PLOS ONE, 7(6): e38883.

Yacef, R., Mellit, A., Belaid, S., Şen, Z., 2014. New combined models for estimating daily global solar radiation from measured air temperature in semi-arid climates: application in Ghardaïa, Algeria. Energy Conversion and Management, 79: 606-615.

Zebarth, B., Caprio, J., Broersma, K., Mills, P., Smith, S., 1997. Effect of climate change on agriculture in the British Columbia and Yukon, BC Ministry of Environment Lands and Parks.

Zelenka, A., Perez, R., Seals, R., Renné, D., 1999. Effective accuracy of satellite-derived hourly irradiances. Theoretical and Applied Climatology, 62(3): 199-207.